博士論文

# A Study on Highly-Functional Hybrid Rockets Using Axial and Tangential Oxidizer Injections

（酸化剤の軸/周方向噴射を用いたハイブリッドロケットの高機能化に関する研究）

小澤　晃平

## Abstract

Hybrid rocket propulsion is a promising candidate as a chemical propulsion system for future space transportation because of its inherent safety and low lifecycle costs. In this thesis, a series of efforts revealed the impacts of an intrinsic characteristic called O/F shifts on flight performances and experimentally demonstrated the concept of a technique to eliminate O/F shifts. In order to evaluate the impact of O/F shifts, vertically launched single stage sounding rocket flight simulations were carried out, and the flight performances between O/F controlled and uncontrolled hybrid rockets were compared. The engine model in the flight simulation includes the sources of O/F shifts unique to hybrid rocket propulsion and the phenomena affected by O/F shifts. The sources of O/F shifts are the nonlinear dependence of nominal fuel regression rates on oxidizer mass flow rates and the uncertainty of fuel regression rates having errors were modeled from the previous experimental results. The systematic O/F shifts in $\pm 3\sigma$ decreased the highest altitudes at most by 10%, and the results also revealed the interesting facts that the most dominant phenomena on flight performances are masses of residual propellants and enthalpy shifts due to O/F shifts. After advantages and disadvantages of several O/F shift elimination technologies were compared, Altering-intensity Oxidizer Flow Type (A-SOFT) hybrid rocket engine was selected as the most promising technology. A-SOFTs apply the dependence of regression rates on swirl strength of the oxidizer injection to control regression rates, O/F ratio, and thrust. The advantages and disadvantages revealed no practical limitation on throttle range and favorable qualitative performances of A-SOFTs compared to the other candidates. The static firing experiments were carried out as the conceptual demonstration of A-SOFTs. This set of the experiments showed monotonous and stable dependence of regression rate, O/F ratio and thrust on oxidizer mass flux and swirl strength. These results are parts of favorable characteristics of A-SOFTs in practical use.

Apart from the above purpose, the mechanism of enhancement of regression rates using swirling injection was also analytically investigated. The classical analytical evaluation of heat transfer to solid fuels was extended in axi-symmetric flows, and static regression rates in swirling hybrids were evaluated. This evaluation indicated that the boundary layer thickness in swirling hybrids reaches the port radius in the middle of the fuel port, and starts to transit to the developed turbulent pipe flow. The predicted results agreed with the previous experimental results of the swirling hybrids. The axial distributions of regression rates of A-SOFTs were also compared between the predictions and the experiments. The predicted curves agreed well with the experimental results, but the transitions to the developed turbulent pipe flow in the large swirl strengths were not clear due to the existence of the nozzle.

## Acknowledgements

It would have been greatly difficult to complete this research or acquire doctoral degree without many types of supports and guidance from a number of individuals. In this paragraph, I will try to acknowledge few of them.

I would like to start with the deepest appreciation to my principal advisor Professor Toru Shimada. From my master degree, he accepted me to enter his laboratory to research hybrid rocket propulsion. During total 5 years with him, I learned the mentality as a scientist and an educator. He always guided me with his great knowledge and kindly accepted to discuss at any available time.

The person who guided me especially from the aspects of experimental researches is Dr. Koki Kitagawa. Even in his extremely busyness on the national rocket projects, he kindly reviewed my planning, discussed results and supervised some parts of my experiments. Without his great know-hows on experiments of rocket engines, it would have been impossible to complete our firing experiments. I would like to great appreciation to him.

Also in our burning experiments, I would like to express my gratitude to Prof. Shigeru Aso in Kyushu University. During the temporary closure of JAXA Akiruno Research Center, he kindly offered the joint research with us, and accepted us to experiment the A-SOFT BBM hybrid rocket engine. I would like to thank also his students, Masato Yamashita, Masato Mizuchi, Koki Katakami and Yudai Maji, and Mr. Kazuhiko Morishita, a technical staff in Kyushu University. Without their great help, I could not complete our firing experiments.

I would like to thank Prof. Wada in Chiba Institute of Technology. He also supervised and gave us many important tips on firing experiments as a co-manager of the Hybrid Rocket Research Working Group. Moreover, I would like to also thank other professors in Hybrid Rocket research Working Group for fruitful discussion and comments on our research in regular meetings and academic conferences.

I would like to express appreciation to the following committee members; Professor Mitsuhiro Tsue, Professor Kimiya Komurasaki, Professor Ichiro Nakagawa, Professor Takehiro Himeno, and Professor Shinji Nakaya. They gave me insightful comments on my thesis in my thesis defense.

My research was supported also by nice lab members. My senior alumni, Dr. Mikiro Motoe and Dr. Yuki Funami gave me many advices and knowledge related to their own research topics of hybrid rocket propulsion. I have many memories on our research activities and study lives with Shota Yamanaka, Akimasa Takayama and Valerian Piento, the members in the same generation in my master course. In my doctoral course, I discussed many topics on aerospace technologies with Goutham Karthikeyan, Tomoaki Usuki, and Akiyo Takahashi. The latter two members and Genki Mishima helped our firing experiments in Kyushu University. Without their support, our firing experiments would have not completed. I would like to show my appreciation to Ms. Saori Sakamoto, the secretary in our lab. She continuously supported our researches from the aspects of many kinds of clerical procedures. I also would like to thank the new comers in our lab in this year; Kei Obata, Tomoaki Matsuno, and Yadav Krishan. They brought fresh energy to promote researches into our lab. Many short-term visitors made my research life stimulating. I would like to acknowledge Dr. Pietro Tadini, Serafin Venegas, Dr. Ippei Takahashi and Ai Watanabe for making my research life enjoyable. I would like to appreciate Dr. Kotaro Matsumoto, Akihiro Iwasaki, and Noboru Itoyama in Hori and Habu Laboratory. They were so nice to give me many advices on our experiments and sometimes they let me borrow experimental goods or use facilities in their lab.

Finally, I would like to express my best gratitude to my parents who always and secretly supported me through my life in the graduate school.

This research was financially supported by JSPS KAKENHI 15J08028. I also would like to acknowledge Global Leader Program for Social Design and Management on financial supports of living expenses for a year of my doctoral course and travel fees for some international conferences.

Table of Contents

## Lists of Figures

## Lists of Tables

# Chapter 1

# Introduction

A hybrid rocket engine is generally a type of rocket engine using solid fuel and liquid or gaseous oxidizer. As is shown in Figure 1.1, a solid fuel is stored inside a combustion chamber and liquid or gaseous oxidizer, stored outside the combustion chamber, is injected into the combustion chamber to burn the solid fuels. The reactant gas is ejected from the nozzle, and yields the thrust. The one using liquid fuel and solid oxidizer is called reverse hybrid rocket, is not currently studied generally.

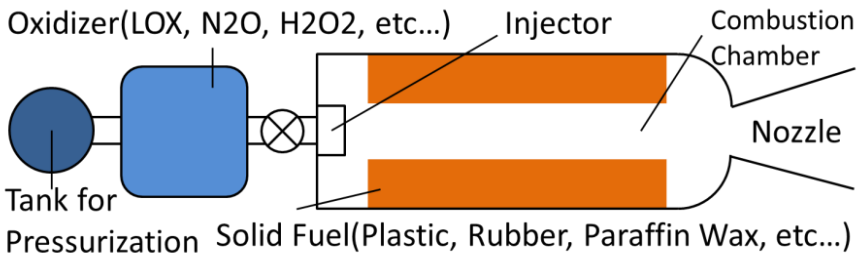


Figure 1.1. A concept of hybrid rocket engines.

## 1.1. Fuel Regression and Combustion Mechanisms of Hybrid Propulsion

Many previous studies[1] reported the fundamental mechanisms of combustion in hybrid rocket propulsion. In the combustion of hybrid rockets, the boundary layer formed over the fuel port wall becomes turbulent due to the scales of the port length larger than lab-scale hybrids, and thickened diffusion flame that located inside the turbulent boundary layer covers all the range of the fuel grain as is shown in Figure 1.2 and Figure 1.3.

In the turbulent boundary layer, oxidizer rich gas is fed from the main flow, and oxidizer rich zone is located between the diffusion flame and the leading edge. Fuel rich zone is located between the fuel port wall and the diffusion flame because pure pyrolyzed and vaporized solid fuel is fed from the fuel wall. Owing to the gasification of the solid fuel, fuel port wall regresses and its rates are called fuel regression rate. In the individual zone, these species distrubute with their density gradients, and the mass of the species and heat flux is transferred by convection and molecular and thermal diffusion.

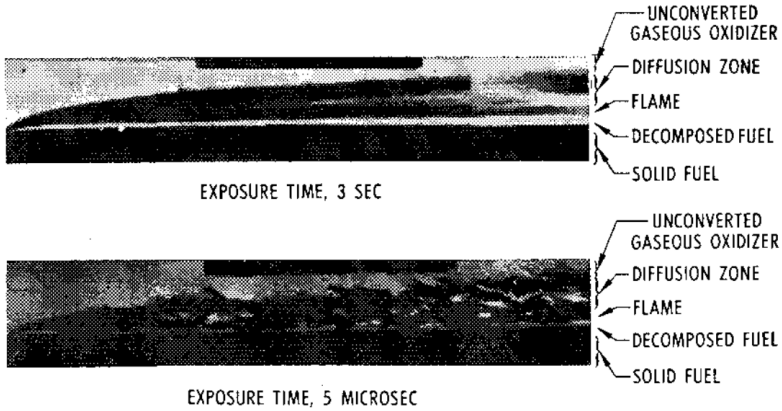


Figure 1.2. Visualizations of diffusion flame of hybrid rocket propulsion[2].

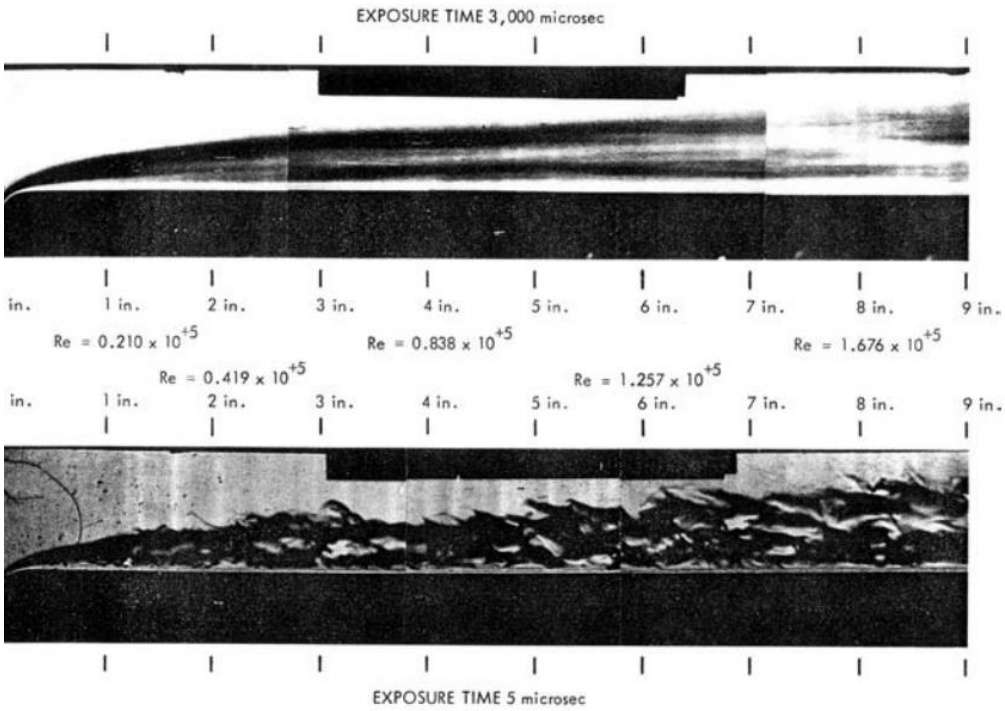


Figure 1.3. Higher resolution figures[3] of Figure 1.2.

Figure 1.4 shows the schematic of the boundary layer combustion in hybrid rocket propulsion. The dominant mechanism of the heat transfer to gasify solid fuels is thermal convection, and the secondary factor is radiation heat transfer. The transferred heat into the wall is divided into two physical phenomena. One is used for gasification of the solid fuel, and the other is the thermal conduction into the solid fuel web. In the cases of transparent solid fuels, radiation can also be transferred directly into the inner solid fuels. We should note that the heat convection with blowing of the solid fuel is smaller than that without

blowing because the gasified fuel makes the temperature gradient gradual at the solid fuel wall.

As explained above, the mechanism of combustion in hybrid rocket propulsion is more complex than in solid or liquid propulsion because fluid dynamics and combustion or chemical reaction are tightly coupled and cannot be separated from each other. Moreover, several non-dominant phenomena such as radiation heat transfer and thermal conduction practically affects the balance of mass and heat transfer and chemical reactions.

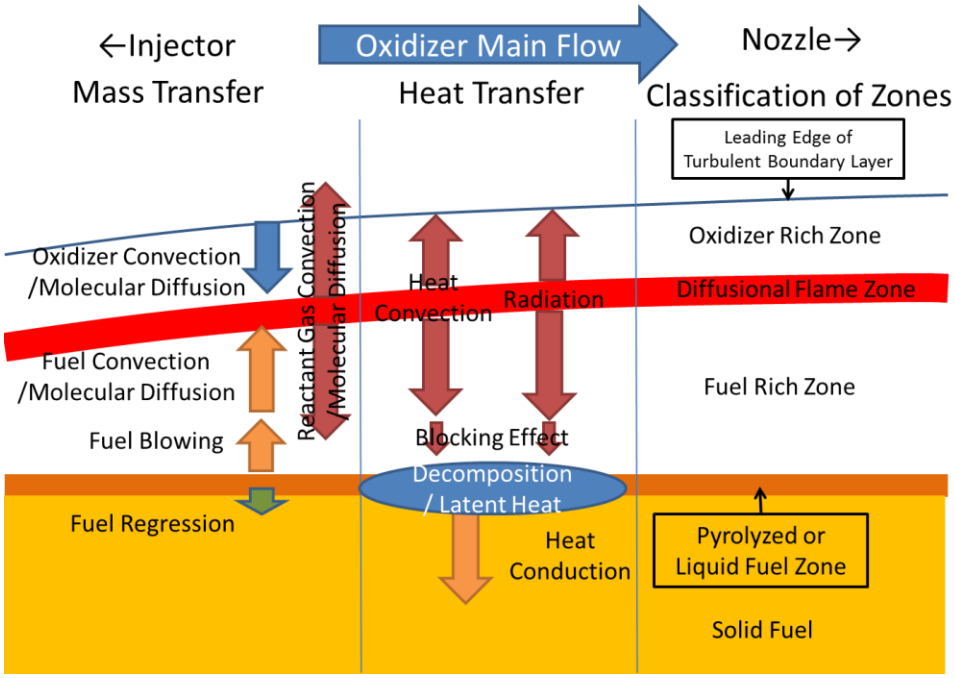


Figure 1.4. A schematic of diffusion combustion in hybrid rocket propulsion.

## 1.2. Advantages, Challenges and Progress of Hybrid Rocket Propulsion

Instead of the complexity of combustion mechanism, hybrid rocket propulsion has many advantages originated from its inherent characteristics over other types of chemical propulsion. Some of the advantages of hybrid rocket propulsion are 1) inherent safety and non-explosiveness, 2) no or less toxicity, 3) simpler structure than liquid propulsion 4) lower manufacture, storage, transportation and operational costs owing to the former three advantages, 5) higher theoretical specific impulse compared to solid propulsion, 6) restart capability and thrust controllability. Non-explosiveness is one of the most unique characteristics. Current launch companies compete their success rates of launches to acquire reliability from customers and to decrease insurance fees included into some percent of launch costs. Insurance fees are calculated by the risk of the damages, namely the

integration of the expected damage and their probability distribution. Besides the cost reduction in lifecycle of rockets, decreasing the damages in failure is also an important strategy of hybrid rocket propulsion.

The major disadvantages of hybrid rocket propulsion are 1) low regression rates of classic fuels, 2) combustion instability in scaled up engines, and 3) O/F shifts. Historically, due to some of these disadvantages, launching rocket projects are set back or cancelled. Most of the researches and developments on hybrid rocket propulsion were aimed to the launch system from the earth. A representative project where the full-scale motors were practically burnt was conducted by the Starstruck and American Rocket Company (AMROC) from 1980s. Their aim was to decrease launch costs of satellites drastically using hybrid rocket propulsion having the advantages mentioned above. As is shown in Figure 1.5, their project reached the practical launch of the sounding rocket SET-1[4] having 75,000 lbf (340kN) class engine. Their launch at the Vandenberg Air Force Base failed because of the frozen LOX main valve, but the rocket finally did not explode even after the collapse of the rocket, and the damage of the launch site was less than $1000 as long as AMROC told[5]. This launch failure unintentionally demonstrated non-explosiveness and safety of hybrid rockets. Despite their failure, their project proceeded and developed full scale 250,000 lbf (1.1MN) class hybrid motors using liquid oxygen (LOX) and Hydroxyl-terminated polybutadiene (HTPB). During this period, AMROC issued a paper on their plan of launch vehicle "Aquila"[4] as is shown in Figure 1.6. The payload performance and the gross weight of this launch vehicle are in the same order as the ones of Mu-V rockets[6]. However, this plan was cancelled because of the shortage of the investment. Because NASA evaluated that hybrid propulsion is a promising candidate of the replacement of the solid rocket boosters (SRBs), after the Space Shuttle Challenger disaster occurred on January 28, 1986, the Hybrid Propulsion Demonstration Program (HPDP) was formed by NASA. In order to mature the technologies on large scale hybrid rocket propulsion, AMROC continued R&Ds on large scale hybrid rocket engines until 1996 under this program. However, they could not completely reveal the mechanism of a mode of combustion instability or solve low regression rates. The intellectual properties of AMROC was bought by Space Dev, currently a department of Sierra Nevada Corporation, and they also opened planning of hybrid launch vehicle "Streaker" series[7] using turbo pumps to feed oxidizer as is shown in Figure 1.7, but this plan was possibly cancelled after this publication.


Figure 1.5. The launch of the sounding rocket of SET-1 by AMROC[8].

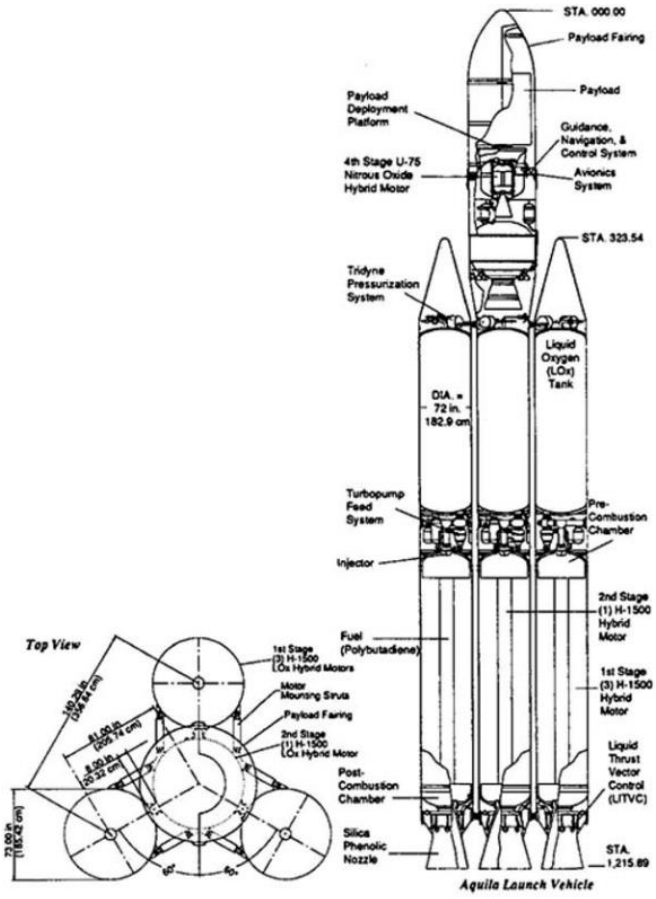


Figure 1.6. Schematics of Aquila by AMROC[4].

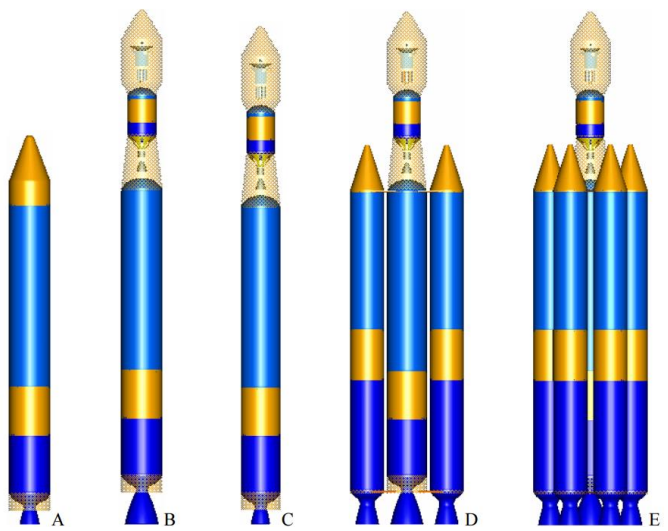


Figure 1.7. Schematics of Streaker series by SpaceDev[7].

On the other hand, besides the failure of the projects to develop large scale hybrids, some project where the disadvantages or challenges did not appear but the advantages of hybrid propulsion were effectively applied successfully ended or evaluated well. Actually, the application of hybrids had shifted to smaller scale missions not having strict requirements on mass fractions or thrust density but severely requiring safety or easiness of handling. A representative successful application is the SpaceShipOne (SS1) project by Scaled Composites as is shown in Figure 1.8. This vehicle achieved the first private ballistic manned space flight in the world only by private resources. As the propulsion system of SS1, hybrid rocket propulsion was selected as the safest propulsion system for manned space vehicle. The propulsion system was developed by Space Dev possibly using the multiport designing technologies acquired by AMROC. This project successfully ended and won Ansari X Prize. Scaled Composites and Virgin Galactic are now planning to commercialize this project by developing a larger vehicle designated as SpaceShipTwo as is shown in Figure 1.9. During a hot firing flight test, SpaceShipTwo broke up as is shown in Figure 1.10, but it was clarified that the reason for this accident was not due to the hybrid propulsion system. Even though the breakup happened, hybrid propulsion system rather did not reach catastrophic explosion and the engine components such as oxidizer tank and combustion chamber dropped on the ground as it was, and the safety of hybrid propulsion system was demonstrated. SpaceDev planned to develop another vehicle using hybrid propulsion designated as DreamChaser as is shown in Figure 1.11. This vehicle is a reusable orbiter to access the International Space Station, and hybrid propulsion system was planned to be applied as the deorbit thruster for reentry into the atmosphere. The design of grains was

also possibly multiport type. DreamChaser survived until the 4th round of CCDev, but lost there for lack of reliability on the delivery term. After this round, hybrid propulsion system was replaced by the liquid propulsion system. These full or partial successes demonstrate the worth in the characteristics of hybrid rocket propulsion.


Figure 1.8.The SpaceShipOne by Scaled Composites[9].


Figure 1.9. The SpaceShipTwo by Scaled Composites[10].

Figure 1.10. The crash of the SpaceShipTwo[11]


Figure 1.11. The DreamChaser by Sierra Nevada Corporation[12].

Some of the challenges setting the projects of hybrid rockets back were improved by recent researches. Karabeyoglu et al. revealed a new intrinsic instability[13] of combustion in hybrid propulsion and found paraffin based fuels[14] as a high regression rate fuel as is shown in Figure 1.12. On the other hand, Yuasa et al.[15] and Knuth et al.[16] independently revealed that the swirling oxidizer injection in hybrid rockets can significantly enhance fuel regression rates[17] as is shown in Figure 1.13. We call this type of engines as Swirling Oxidizer Flow Type (SOFT) hybrid rocket engines. Their approach from the aspect of flow dynamics in the combustion chamber was different from Karabeyoglu's one.

Figure 1.12. A visualization of diffusion combustion of a paraffin based fuel[18].


Figure 1.13. A visualization of a SOFT hybrid rocket engine[19].

Some of these significant researches led to founding new projects. NASA Ames Research Center, Stanford University and Space Propulsion Group (SPG) planned to develop Peregrine sounding rocket for the flight demonstration of high thrust density hybrid propulsion using paraffin based fuels. Figure 1.14 shows a burn test of a prototype engine of Peregrine hybrid sounding rockets[20]. This project is still being continued as of April 2016. NASA Jet Propulsion Laboratory, Stanford University and SPG started to research hybrid propulsion system for the ascent propulsion system from the ground of Mars to orbit[21] as is shown in Figure 1.15. On other planets smaller than the earth, the propulsion system is required to resist to environment in the planet during long term mission over several years instead of its thrust density. The main reason for the selection of hybrid propulsion system is that solid fuels of hybrids have less sensitivity to temperature change or cracks than solid propellants, and have competitiveness on propulsion performances to them. Moreover, hybrid propulsion system has a possibility to produce fuel grains or oxidizers on site in the future. Owing to the large fund for this project from NASA, some unique studies necessary to use hybrids in space have already started[21,22,23,24].

Figure 1.14. A burn test of the engine of the Peregrine hybrid sounding rocket[20].

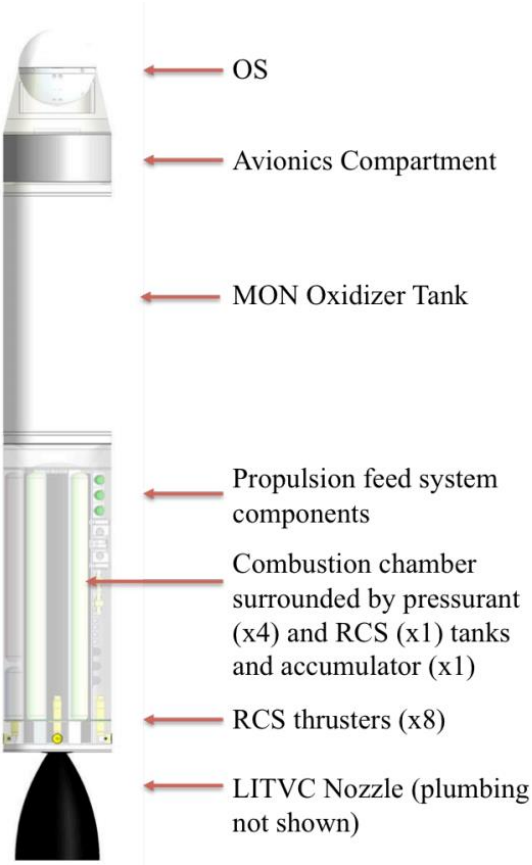


Figure 1.15. A concept of Mars Ascent Vehicle using hybrid rocket propulsion[21].

## 1.3. O/F Shifts of Hybrid Rocket Propulsion

Unlikely other major disadvantages of hybrid rocket propulsion, many previous

researches to discuss O/F shifts are not found. Even if there are, these researches did not comprehensively handle the sources and effects of O/F shifts. Figure 1.16. summarizes the sources and effects of O/F shifts. Originally, there are three sources to cause O/F shifts. The first and the second mechanisms are caused by nonlinear dependence of fuel mass flow rates on oxidizer mass flow rates. Owing to these characteristics, O/F shifts always occur in throttling or expansion of port diameter in the courses of solid fuel consumption. The third mechanism is random or systematic errors of practical fuel regression rates or oxidizer mass flow rates from the modelled ones. This type of O/F shifts can always occur during combustion.

Compared to liquid or solid propulsion, in hybrid propulsion, the scale of the errors of fuel mass flow rates or fuel regression rates is large from the predicted one as is shown in Figure 1.16. This is because fuel regression is not independent of oxidizer mass flow and the complex mechanisms of fuel regression and combustion in hybrid propulsion make it difficult to predict fuel regression rates accurately. Computer fluid dynamics (CFD) is a promising solution to this problem, but it seems to be too difficult still now to develop the comprehensive and practical codes to predict regression rates in wide range of scales and conditions. This is mainly because dominant chemical reactions and intermediate reactants changes in wide range of local O/F ratio and temperature in turbulent boundary layer, and it is difficult to include so complex solid fuel decomposition process as is shown in Figure 1.18. Moreover, in high regression rate fuels, CFD models should be more complex because entrainment of high density paraffin wax observed in Figure 1.12 and supercritical flow of the melted fuels[25,26] should also be modeled. Therefore, currently O/F shift caused by random or systematic errors of fuel regression rates should be taken into account.

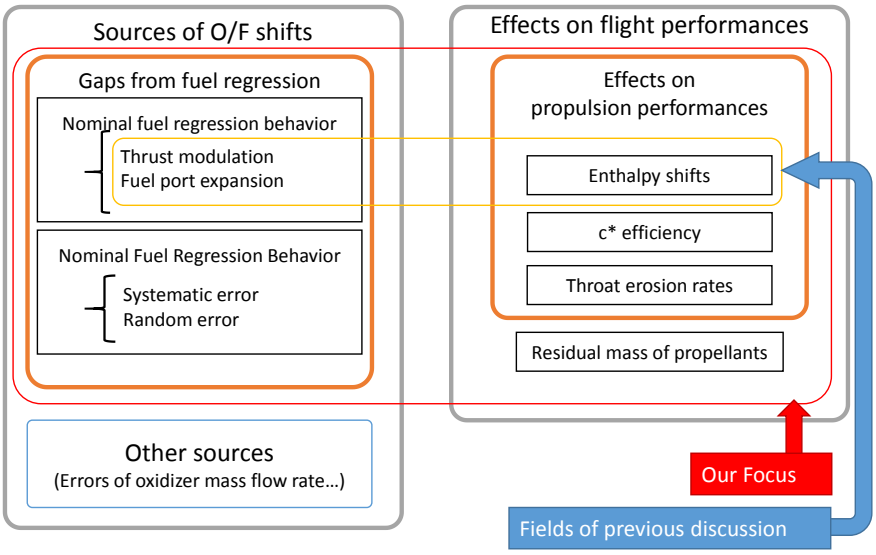


Figure 1.16. Sources and effects of O/F shifts.

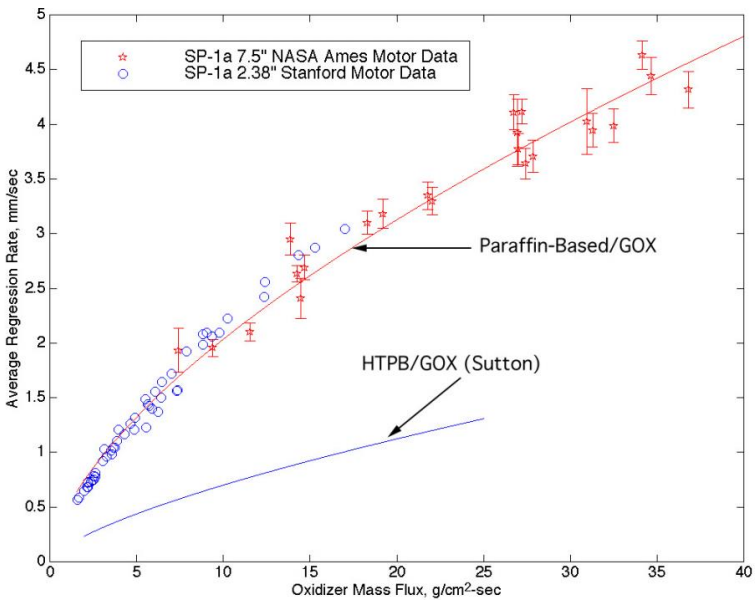


Figure 1.17. Fuel regression behavior of paraffin based fuels[27].

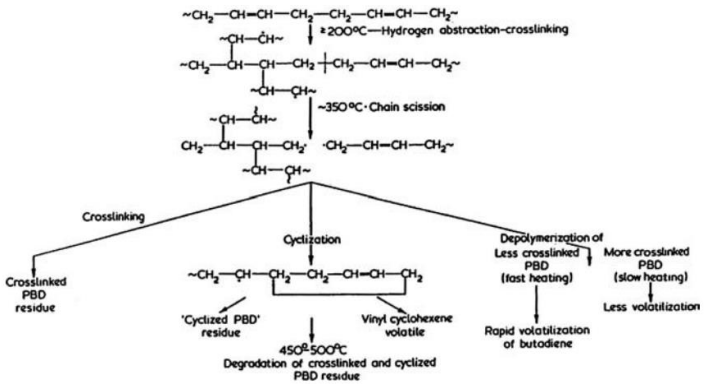


Figure 1.18. Schematics of thermal degradation of HTPB[1].

O/F shifts should affect the several phenomena on propulsion performances as is shown in Figure 1.16. A major effect of O/F shifts is to shift enthalpy per unit mass of the productive gas (enthalpy shift), other thermodynamic variables, the exit velocity of the burnt gas from the nozzle exit and finally the thrust or the specific impulse. These effects of O/F shifts are discussed in several previous papers[2,28,29,30], and they evaluated their impacts as small or negligible under constant thrust level while they said there is at most 10% Isp loss in throttling. The secondary effects are shifts of c* efficiency and nozzle throat erosion rates. In chemical rocket propulsion, c* efficiency is related with normalized chamber length by ideal chamber length necessary to complete chemical reaction inside chamber[31]. O/F shifts affect ideal representative chamber length because O/F ratio is a variable to determine ideal characteristic exhaust velocity of the productive gas. The erosion of nozzle throat carbon materials is also affected by O/F shifts because O/F shifts change molecular fractions of the oxidizing species in the reactant gas such as $H_2O$, OH, $O_2$, O and $CO_2$[32]. These two phenomena should also be affected by O/F shifts through these mechanisms, but these impacts had not been evaluated.

Moreover, O/F shifts can influence not only propulsion performance but also flight performance. Residual mass of propellants due to O/F shifts tends to be overlooked because this performance loss is not classified into propulsion performance, but into flight performance. When a single type of hybrid propulsion system is used for several purposes of different thrust curve, it is easy to expect generation of residuals due to O/F shifts in throttling. The series of flight simulations by Usuki et al.[33] is a representative evaluation of the impacts of O/F shifts and residual mass on the flight performances in the multipurpose missions requiring individually different thrust curves. The mission was hovering mission at constant altitude, and the evaluation variable was hover duration. The results are summarized in Figure 1.19, and it is clear that residual mass affects a large impact on flight

performances because the O/F uncontrolled rocket generated 2.8% residual of all the propellants and lost 40% hover duration of the O/F controlled one at 50 [km] altitude while they similarly performed at 400 [km] altitude. Moreover, even if thrust profiles are fixed, residual problem can be generated due to the O/F shifts caused by the fuel regression errors. Some papers evaluated impacts of the residual caused by the systematic errors of fuel regression rates[34,35], but the scale of them were not based on the static ones derived from experimental data but parametrically given ones.

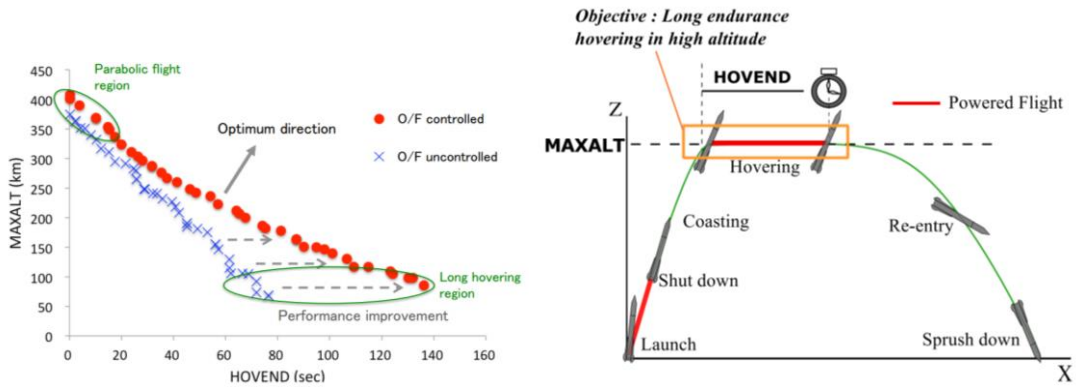


Figure 1.19. The results of the simulations of a multipurpose mission using hybrid sounding rockets.

Though the causes or risks of O/F shifts were not considered comprehensively, some previous researches proposed the several systems to eliminate O/F shifts. A representative system is the Aft-end Oxidizer Injection System[2] as is shown in Figure 1.20. In this system, reactant gas always in fuel rich condition is ejected from the tail-end of the combustion chamber, and the oxidizer injector is located also in the aft-combustion chamber. The O/F ratio is adjusted by the oxidizer flow from the tail injector. The paper briefly reported that this technology had basically demonstrated in 1965, but the detailed experimental results were not reported. The other paper in 1995 reported the results of the demonstration of the real-time data acquisition of regression rates using ultrasound devices to sense remained fuel grain web-thickness for a feedback system of the Aft-end Oxidizer Injection System. Another representative method to eliminate O/F shifts using pressure sensitive fuels (PSF) was mentioned also in the reference[28]. PSF is to add sensitivity to chamber pressure into regression rate behaviors. Most conventional solid fuels of hybrids have less sensitive to chamber pressure, but it is possible to add pressure sensitivity using self-decomposing or reactive propellants such as glycidyl azide polymer[1] and solid oxidizers as additives because solid propulsion has strong pressure sensitivity[36].

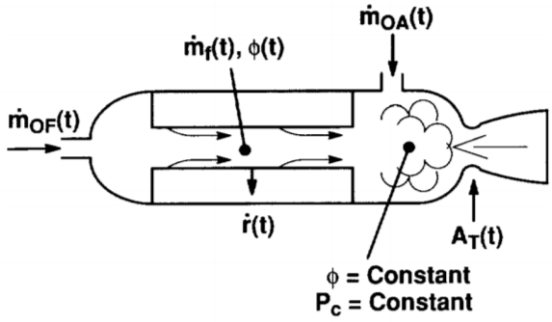


Figure 1.20. A concept of Aft-end Oxidizer Injection method[29].

## 1.4. Purposes and Approaches of the Thesis

The major purpose of this thesis is to reveal that the impact of O/F shifts on flight performances is considerable even for single purpose missions, propose the O/F controlled and throttlable hybrid propulsion systems as "highly functional hybrid propulsion systems" and to experimentally demonstrate the concept of the O/F shift elimination technology using swirling oxidizer injection as one of the most promising solutions to O/F shifts. Apart from the demonstration of this technology, the mechanism of the fuel regression rates in SOFTs is analytically discussed in order to compare with and apply for the O/F controlled hybrid propulsion. This work is intended not only to reveal the qualitative mechanisms of fuel regression rates unique to this type of engines, but also to contribute to the fuel regression rate prediction and designs of fuel grain port of our proposing type of engines. Moreover, the difference of the fuel regression rates between SOFTs and our proposing ones can be discussed in more detail.

In order to accomplish this goal, one has to divide the research into 3 individual topics such as 1) evaluation of the impacts of O/F shifts on flight performances, 2) trade-offs among the several ideas to eliminate O/F shifts, 3) analytical evaluation of fuel regression rates of SOFT hybrid rockets and 4) experimental demonstration of the concept of the selected O/F shift elimination technology.

This thesis focuses on the impossibility of direct control of fuel regression rate behaviors. Therefore, O/F shifts caused by other factors such as oxidizer feed system and machining accuracy of engine components is not handled in this thesis. In the evaluation of the impacts of O/F shifts, it is necessary to specify the mission to evaluate the impacts of O/F shifts because it is totally difficult to comprehensively evaluate the impacts of O/F shifts on flight performances. Also in the conceptual demonstration of the technology, this thesis only

focuses on the experimental demonstration of the most fundamental characteristics for O/F shift elimination, the monotonous dependence of regression rates on other operational variable than oxidizer mass flow rate or oxidizer mass flux.

In Chapter 2, as the evaluation of the impacts of O/F shifts on flight performances, the flight simulation of vertical launches of single stage sounding rocket is set as the problem. This is because the sounding rocket is a representative mission to practically demonstrate or to develop a new conceptual propulsion system, because it includes throttling to acquire altitude efficiently under aerodynamic drag, and because the highest altitude is one of the simplest evaluation variables for flight performances. The flight and propulsion performances of O/F uncontrolled hybrid rockets are compared with the ones of hypothetical O/F controlled hybrid rockets.

In Chapter 3, the characteristics of the several ideas for O/F shift elimination are compared. As explained before, the two candidates of O/F shift elimination technologies are previously proposed. In this comparison, throttle ranges of the individual methods available at constant O/F ratio is evaluated, and qualitative trade-offs are compared from the aspects of structural coefficient, combustion stability, complexity of the system, and so on. At the end of this chapter, from the above aspects, whether our proposing technology applying SOFTs is selected as the most favorable technology for O/F shift elimination is discussed.

In Chapter 4, the fuel regression rates behaviors of SOFTs are analytically modeled and axial distribution of regression rates in SOFTs are predicted. In this chapter, the classic diffusion limited analysis to evaluate heat transfer from the diffusion flame into the solid fuel wall in flat plate turbulent boundary layer is extended for in axisymmetric flow. In this extended analysis, the cross-sectional momentum and angular momentum in the main flow are also evaluated because local heat transfer in the boundary layer and the main flow influence each other in SOFT hybrid rockets. The axial distribution of regression rates predicted from the analyses is compared with several experimental results, and the differences between the analytical and experimental results and characteristics of the analytical method are discussed.

Finally, in Chapter 5, the concept of our proposing technology to eliminate O/F shifts is experimentally demonstrated. In order to show monotonous dependence of regression rates on both oxidizer mass flux and swirl strength, static firing experiments are carried out in several operational conditions of oxidizer mass flow rate and swirl strength.

After the experiments, characteristics of time averaged fuel regression rates and their axial distribution are measured. These results are compared with the ones of SOFTs, and the analytical prediction of regression rates created in the prior section.

In Chapter 6, this thesis is concluded by summarizing the conclusions of the prior chapters, and the future works on the thrust and O/F control system in hybrid rocket propulsion are discussed.

Bibliography of Chapter 1


1 Chiaverini, M. J., Kuo, K. K., *Fundamentals of Hybrid Rocket Combustion and Propulsion*, Virginia: AIAA, 2007.

2 Ordahl, D. D., "Recent Developments and Current Status of Hybrid Rocket Propulsion," *Journal of Spacecraft and Rockets*, vol. 2, 1965, pp. 923–926.

3 Marxman, G. A., Wooldridge, C. E., and Muzzy, R. J., "Fundamentals of Hybrid Boundary Layer Combustion," *Heterogeneous Combustion Conference*, vol. 63–505, 1963.

4 Estey, P., and Flittie, K., "Aquila - The Next Generation Launch Service for Small Satellites," *14th International Communication Satellite Systems Conference and Exhibit*, Washington, D.C.: AIAA, 1992, p. AIAA 92-1844.

5 Kniffen, R. J., McKinney, B., and Estey, P., "Hybrid Rocket Development at the American Rocket Company," *AIAA/SAE/ASME/ASEE 26th Joint Propulsion Conference*, Orlando, FL: AIAA, 1990, p. AIAA 90-2762.

6 Onoda, J., Sato, E., Y., I., K., M., and T., S., "Return to the Flight of M-V Rocket," *55th International Astronautical Congress*, Vancouver, Canada: IAF, 2004, p. IAC-04-V.1.02.

7 Macklin, F., Grainger, C., Veno, M., and Benson, J., "New Applications For Hybrid Propulsion.," *39th AIAA/ASME/SAE/ASEE Joint Propulsion Conference and Exhibit*, Huntsville, AL: AIAA, 2003, p. AIAA 2003-5202.

8 "SET-1 Launch Attempt" Available: https://www.youtube.com/watch?v=zhlbnbIuUxk.

9 "SpaceShipOne Press Gallery," *Scaled Composites* Available: http://www.scaled.com/hires_gallery/gallery/press_gallery/single/SS1_on_ground_lr.

10 "Our Vehicles," *Virgin Galactic* Available: http://www.virgingalactic.com/human-spaceflight/our-vehicles/.

11 Kenneth, C., "Virgin Galactic Is Rattled, but Undeterred, by Deadly Space Plane

Crash," *The New York Times*, 2014.

12 "SNC's Dream Chaser On Runway at NASA's Dryden Flight Research Center at Dawn (Profile)," *Sierra Nevada Corporation* Available: http://www.sncspace.com/Mediakit/Images.

13 Karabeyoglu, A., Zilwa, S. De, Cantwell, B., and Zilliac, G., "Modeling of Hybrid Rocket Low Frequency Instabilities," *Journal of Propulsion and Power*, vol. 21, 2005, pp. 1107–1116.

14 Karabeyoglu, M. a, Cantwell, B. J., and Altman, D., "Development and Testing of Paraffin-Based Hybrid Rocket Fuels," *37th AIAA/ASME/SAE/ASEE Joint Propulsion Conference and Exhibit*, Salt Lake City, UT: AIAA, 2001, p. AIAA 2001-4503.

15 Yuasa, S., Shimada, O., Imamura, T., Tamura, T., and Yamamoto, K., "A Technique for Improving of Hybrid Rocket Engines the Performance," *35th AIAA/ASME/SAEASEE Joint Propulsion Conferenceand Exhibit*, Los Angeles, CA: AIAA, 1999, p. AIAA 99-2322.

16 Knuth, W. H., Chiaverini, M. J., Gramer, D. J., and Sauer, J. a, "Experimental Investigation of a Vortex-Driven High-Regression Rate Hybrid Rocket Engine," *34th AIAA/ASME/SAE/ASEE Joint Propulsion Conference and Exhibit*, Cleveland, OH: AIAA, 1998, p. AIAA 98-3348.

17 Tamura, T., Saburo, Y., and Kengo, Y., "Effects of Swirling Oxidizer Flow on Fuel Regression Rate of Hybrid Rockets," *35th AIAA/ASME/SAE/ASEE Joint Propulsion Conference and Exhibit*, Los Angeles, California: AIAA, 1999, p. AIAA 99-2323.

18 Nakagawa, I., and Hikone, S., "Study on the Regression Rate of Paraffin-Based Hybrid Rocket Fuels," *Journal of Propulsion and Power*, vol. 27, 2011, pp. 1276–1279.

19 Yuasa, S., Shiraishi, N., and Hirata, K., "Controlling Parameters for Fuel Regression Rate of Swirling-Oxidizer-Flow-Type Hybrid Rocket Engine," *48th AIAA/ASME/SAE/ASEE Joint Propulsion Conference & Exhibit*, Atlanta, GA: AIAA, 2012, p. AIAA 2012-4106.

20 "NASA Ames Tests Peregrine Hybrid Sounding Rocket Motor," *NASA's Ames Research Center* Available: https://www.youtube.com/watch?v=d8iOzQXyMA4.

21 Karp, A. C., Nakazono, B., Benito, J., Shotwell, R., Vaughan, D., and Story, G., "A Hybrid Mars Ascent Vehicle Concept for Low Temperature Storage and Operation," *52nd AIAA/SAE/ASEE Joint Propulsion Conference*, Salt Lake City, UT: AIAA, 2016, p. AIAA 2016-4962.

22 Stober, K. J., Thomas, A., Evans, B. J., and Cantwell, B. J., "Investigation of Green Hypergolic Propellants for Hybrid Rockets," *52nd AIAA/SAE/ASEE Joint Propulsion Conference*, Salt Lake City, UT: AIAA, 2016, p. AIAA 2016-4991.

[23] Costantino, A. M., Narsai, P., and Cantwell, B. J., "Nondestructive Mapping of Hybrid Rocket Fuel Grains," *52nd AIAA/SAE/ASEE Joint Propulsion Conference*, Salt Lake City, UT: AIAA, 2016, p. AIAA 2016-4866.

[24] Farias, E., Redmond, M., Karp, A., Shotwell, R., Mechentel, F., and Story, G., "Thermal Cycling for Development of Hybrid Fuel for a Notional Mars Ascent Vehicle," *52nd AIAA/SAE/ASEE Joint Propulsion Conference, 2016, July 25, 2016 - July 27, 2016*, Salt Lake City, UT: AIAA, 2016, p. AIAA 2016-4563.

[25] Karabeyoglu, M. a., Altman, D., and Cantwell, B. J., "Combustion of Liquefying Hybrid Propellants: Part 1, General Theory," *Journal of Propulsion and Power*, vol. 18, 2002, pp. 610–620.

[26] Karabeyoglu, M. a., and Cantwell, B. J., "Combustion of Liquefying Hybrid Propellants: Part 2," *Journal of Propulsion and Power*, vol. 18, 2002, pp. 621–630.

[27] Karabeyoglu, A., Zilliac, G., Cantwell, B. J., DeZilwa, S., and Castellucci, P., "Scale-Up Tests of High Regression Rate Paraffin-Based Hybrid Rocket Fuels," *Journal of Propulsion and Power*, vol. 20, 2004, pp. 1037–1045.

[28] Waidmann, W., "Thrust Modulation in Hybrid Rocket Engines," *Journal of Propulsion and Power*, vol. 4, 1988, pp. 421–427.

[29] Boardman, T., Porter, L., Brasfield, F., and Abel, T., "An Ultrasonic Fuel Regression Rate Measurement Technique for Mixture Ratio Control of a Hybrid Motor," *31st Joint Propulsion Conference and Exhibit*, San Diego, CA: AIAA, 1995, p. AlAA 95-3081.

[30] Karabeyoglu, A. M., and Evans, B. J., "'O/F Shift' in Hybrid Rockets," *50th AIAA/ASME/SAE/ASEE Joint Propulsion Conference*, Cleveland, OH: AIAA, 2014, p. AIAA 2014-3851.

[31] Huzel, D. K., and Huang, D. H., *Modern Engineering for Desing of Liquid-Propellant Rocket Engines*, AIAA, 1992.

[32] Chelliah, H. K., Makino, A., Kato, I., Araki, N., and Law, C. K., "Modeling of Graphite Oxidation in a Stagnation-Point Flow Field Using Detailed Homogeneous and Semiglobal Heterogeneous Mechanisms with Comparisons to Experiments," *Combustion and Flame*, vol. 104, 1996, pp. 469–480.

[33] Usuki, T., and Shimada, T., "Investigation of Flight Profiles Suitable for Altering-Intensity Swirling-Oxidizer-Flow-Type Hybrid Rocket," *51st AIAA/SAE/ASEE Joint Propulsion Conference*, Orlando, FL: AIAA, 2015, p. AIAA 2015-3939.

[34] Barato, F., Grosse, M., and Bettella, A., "Hybrid Rocket Fuel Residuals - an Overlooked Topic," *50th AIAA/ASME/SAE/ASEE Joint Propulsion Conference*,

Cleveland, OH: AIAA, 2014, p. AIAA 2014-3753.

[35] Casalino, L., and Pastrone, D., "A Straightfotward Approach for Robust Design of Hybrid Rocket Engine Upper Stage," *51st AIAA/SAE/ASEE Joint Propulsion Conference*, Orlando, FL: AIAA, 2015, p. AIAA 2015-4202.

[36] Sutton, G., and Biblarz, O., *Rocket Propulsion Elements*, John Wiley & Sons, Inc, 2001.

# Chapter 2.

# Evaluations of Effects of O/F Shifts on Flight Performances of Sounding Rocket Mission Using Hybrid Rocket Propulsion

In this chapter, intensity of O/F shifts and their impacts on flight performances of rockets are evaluated. As explained in the prior chapter, scales of O/F shifts depend on missions, thrust curves, scales and designs of fuel grains or propellant options. Moreover, physical phenomena dependent on O/F shifts in engines are also affected by these factors. Thus, it is greatly difficult to comprehensively evaluate those impacts about all individual missions. Therefore, in this chapter, vertical launch of S-520-class[1] single stage sounding rocket is set as a mission to be evaluated as a case study. This is because a new concept of propulsion systems are typically demonstrated in sounding rocket missions before starting launching rocket missions to put satellites into orbits. Moreover, single stage sounding rocket missions usually include throttling to acquire altitude efficiently under aerodynamic drag and gravity loss. Performances of sounding rockets can easily be evaluated with the highest altitude, which is one of the simplest evaluation variables for flight performances. Flight and propulsion performances of O/F uncontrolled hybrid rockets are compared with those of hypothetical O/F controlled hybrid rockets using O/F shift elimination technologies. In this chapter, the highest altitude in an individual flight is regarded as a primary evaluation variable for simplicity.

## 2.1. Hybrid Rocket Engine Model

Our hybrid rocket engine model simulates propulsion performances of hybrid rocket engines during engine operations in flight simulations. From the purpose of this chapter, the engine model has both individual physical phenomenon being a source of O/F shifts and ones affected by O/F shifts. As explained in the prior chapter, the former is the solid fuel regression phenomenon. The latter ones are the combustion to yield enthalpy in the gaseous products, c* efficiency, nozzle throat erosion, and nozzle flow. All these phenomena are modeled in this section. In the following subsections, the analytical expressions of these models are derived or introduced, and if necessary, their validations are shown.

2.1.1. Solid Fuel Regression Rate Models

In this model, the fuel regression rate behavior is given in order to assume realistic order of magnitude of regression rates and controllable range of O/F ratios.

In this chapter, a combination of paraffin wax and gaseous oxygen (WAX+GOX) is selected as the propellants used in the hybrid rocket engine models because of high baselines of regression rates whereas oxidizer is assumed to be stored in liquid state in the rocket model. In O/F-controlled cases, O/F ratio is assumed to be controllable using variable geometric swirl number, which is defined as ideal angular momentum normalized by axial momentum a tangential injector of SOFTs yields. This assumption is based on the previous researches which proved the monotonous dependence of fuel regression rates on geometric swirl number of tangential injectors of SOFTs. However, there are few existing researches on dependence of regression rates on swirl number using WAX+GOX. The only two accessible papers by Nakagawa et al.[2] and Saito et al.[3] have reported that WAX+GOX has far higher sensitivity to geometric swirl number than other conventional propellants. However, the number of experimental conditions and trials in these researches were too small, and currently it is too difficult to model practical characteristics of fuel regression behavior of SOFTs using WAX+GOX.

On the other hand, there are relatively broad data on the dependence of geometric swirl number in SOFTs using polymethyl methacrylate and gaseous oxygen (PMMA+GOX)[4,5]. Both of the results were reported by Yuasa's group. The geometry of the fuel grains used in these series of burning experiments were 40[mm] initial port diameter and 150 or 500[mm] in lengths. The experimental conditions had the 5 options of geometric swirl numbers of 0, 7.1, 9.7, 19.4 and 32.3. In these set of experiments, geometric swirl number is defined as the following equations as

$$S_g = \frac{R_m \rho u_{inj}^2 A_{inj}}{R \rho u_{z_e}^2 A_{port}} = \frac{R_m A_{port}}{R A_{inj}} \tag{2.1}$$

where $R_m$ refers to the moment arm of the injector ports, the subscripts of "inj" and "port" refer to injector ports and injector outlet, and mass conservation law of $\rho u_{inj} A_{inj} = \rho u_{z_e} A_{port}$ is applied. The regression rates in their experiments were measured as averaged ones along with time and axial directions and approximated with a fuel regression model dependent on timely averaged oxidizer mass flux from the expression by Marxman et al.[6] as

$$\dot{r}(t) \approx \overline{\dot{r}_p} \equiv \frac{\int_0^L \int_0^T aG^{0.8}x^{-0.2}dx}{LT} \approx aG_o{}^n \tag{2.2}$$

where $\overline{\dot{r}_p}$, $L$, $T$, $x$, $a$ and $G$ respectively refer to timely and axially averaged fuel regression rates, fuel port length, burn time, axial distance, a constant coefficient and mass flux at an axial position, and $G_o$ and $n$ respectively refer to time averaged oxidizer mass flux and a constant exponent. According to the previous experiments, the dependence of $n$ on geometric swirl number were relatively small, and $a$ was approximated by the following equation as

$$a/a_0 = \left(1 + S_g{}^2\right)^m \tag{2.3}$$

where $a_0$, $S_g$ and $m$ respectively refer to a constant coefficient in $S_g = 0$, geometric swirl number and a constant exponent. Because this approximation can fit the results well, the regression rate equation used in this chapter is assumed to be

$$\dot{r}(t) = a_0 G_o(t)^n \left(1 + S_g(t)^2\right)^m \tag{2.4}$$

where $G_o$ is a function of time because $G_o$ changes due to the increases of the port diameter or due to throttling. $S_g$ can also be a function of time when manipulability of $S_g$ is assumed in order to control O/F ratio. This expression of regression rates is also applied to the SOFTs using WAX+GOX in the flight simulations. Practically, representative values of $a_0$, $n$ and $m$ of WAX+GOX cannot be found from previous researches. Therefore, $a_0$ and $n$ are approximated from experimental data of axially-injected hybrids (axial hybrids) using WAX+GOX[7], and $m$ is approximated from those of the researches by Yuasa et al.[4,5] In addition to the median regression rate behavior, the uncertainty of regression rates should also be combined using the two series of fuel regression data of axial hybrids using WAX+GOX and those of SOFTs using PMMA+GOX. In the next subsections, the results of the data analyses and the median and error models used in the simulations are shown.

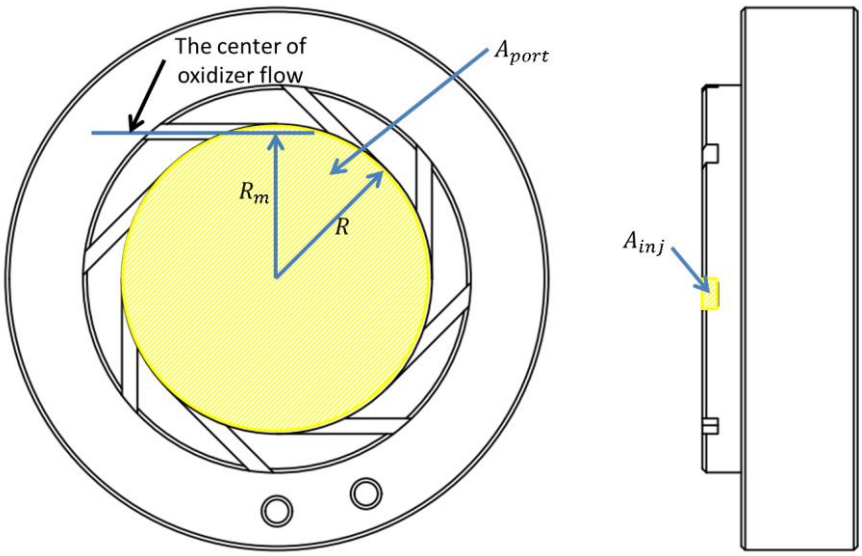


2.1.1.1. Multiple Regression Analyses of Fuel Regression Behaviors from Existing Researches

In this subsection, using multiple regression analyses, median and error models of fuel regression rates of axial hybrids using WAX+GOX and SOFTs using PMMA+GOX are constructed. Before analyzing the existing experimental data, multiple linear regression analysis[8] is briefly explained. From this analytical method, not only uncertainty of errors from median value, but also that of median value are modelled.

First, a relation to estimate between a result $y$ and a set of experimental conditions $x$ ( a $1 \times n$ matrix : $(x_1 = 1, x_2, \ldots, x_n)$) should be assumed as the following equation:

$$y = x\beta + e \tag{2.5}$$

where $\beta$ is a constant $n \times 1$ matrix, and $e$ is an error subject to a normal distribution. Now, let us suppose that $m$ experiments subject to Eq. (2.5) output a dataset of a $m \times n$ matrix of the experimental conditions $X$ and a $m \times 1$ matrix $Y$. According to a multiple regression analysis theory[8], the estimated coefficient vector $B = \mathrm{E}(\beta)$ can be expressed as

$$B = (X^T X)^{-1} X^T \tag{2.6}.$$

The residual sum of squares ($SSR$) and the variance of $Y$ ($\sigma$) have the following relation as

$$SSR = (m-n-1)\sigma^2 = \sum_{i=1}^{m}(Y_i - X_i B)^2 = Y^T Y - B^T X^T Y \qquad (2.7).$$

A confidence interval (a CI) refers to an estimated existing area of the median linear relation between $x$ and $y$ with two-sided probability of $a$. The upper and lower limits of the CI are

$$y = Bx \pm \sqrt{\frac{SSR x^T (X^T X)^{-1} x}{m-n-1}} t_{\frac{a}{2},m-n-1} = Bx \pm \sigma\sqrt{x^T (X^T X)^{-1} x} t_{\frac{a}{2},m-n-1} \qquad (2.8)$$

where $t_{\frac{a}{2},m-n-1}$ refers to the $m-n-1$th Student's t-distribution[8] of two-sided probability of $a$. A CI means uncertainty of an estimated median equation. If the range and the number of experimental points become large, the term $x^T (X^T X)^{-1} x$ in Eq. (2.8) should become small and finally converges to zero. A prediction interval (a PI) refers to an estimated existing area of the median linear relation between $x$ and $y$ with two-sided probability of $a$. The upper and lower limits of the PI are

$$y = Bx \pm \sqrt{\sigma^2 + \sigma^2 x^T (X^T X)^{-1} x} t_{\frac{a}{2},m-n-1} = Bx \pm \sigma\sqrt{\{1 + x^T (X^T X)^{-1} x\}} t_{\frac{a}{2},m-n-1} \qquad (2.9).$$

The uncertainty of PI should converge to $\sigma t_{\frac{a}{2},m-n-1}$ after infinite experiments because regression analyses generally take normal distribution errors from model equations into account in advance.

Using this method, we analyze the existing regression rate data. The linear regression analysis is applicable to the regression rate equation by taking logarithm of the both sides of Eq. (2.4) as

$$\ln \dot{r} = \ln a_0 + n \ln G_o + m \ln\left(1 + {S_g}^2\right) \qquad (2.10).$$

The fuel regression data of axial hybrids using WAX+GOX are quoted from the research by Karabeyoglu et al.[7] This paper showed the total 69 data points in a broad range of oxidizer mass flux and fuel regression rates. The upper and lower limits of the CI in the axial hybrids using WAX+GOX are

$$\ln \dot{r} = -2.22 + 0.640 \ln G_o \pm \sigma\sqrt{x^T (X^T X)^{-1} x} t_{\frac{a}{2},67} \qquad (2.11)$$

$$\sigma^2 = 4.61 \times 10^{-3}, x^T(X^TX)^{-1}x = (1 \quad \ln G_o)\begin{pmatrix} 31.3 & -7.06 \\ -7.06 & 16.7 \end{pmatrix}(1 \quad \ln G_o)^T \times 10^{-2}$$

where $\dot{r}$ in [mm/s] is approximated with $G_o$ in [kg/m²s]. In Figure 2.1, the median of the fuel regression rates and its limits of PI and CI of $\pm 3\sigma$ in normal distribution are compared with the experimental results. Figure 2.2 shows the uncertainty model of the CI $\sigma\sqrt{x^T(X^TX)^{-1}x}$. The errors of the CI and PI take the minimum values at the averaged operating point of the burning experiments.

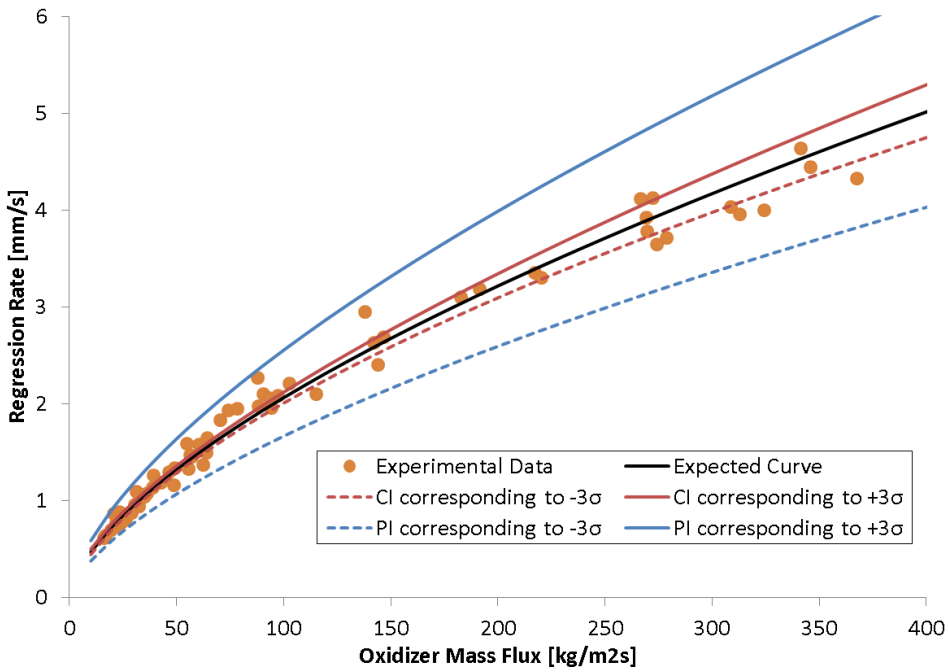


Figure 2.1. Comparison of the limits of CI and PI of the regression rate model of the axial hybrids using WAX+GOX with the experimental results.

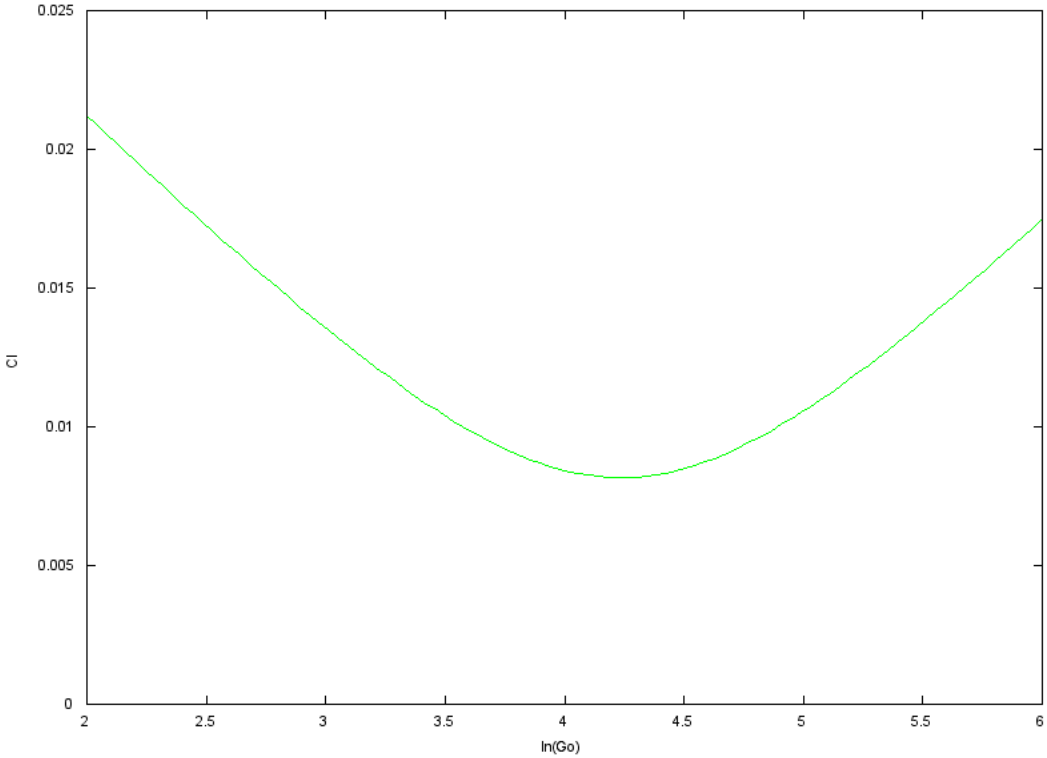


Figure 2.2. Plot of the distribution of the error of the CI of the axial hybrids using WAX+GOX.

The fuel regression data of SOFTs using PMMA+GOX are quoted from the researches by Yuasa et al.[4,5] These papers show the total 45 data points in a relatively small range of oxidizer mass flux with 5 options of geometric swirl numbers. The upper and lower limits of the CI of SOFTs using PMMA+GOX are

$$\ln \dot{r} = -3.70 + 0.616 \ln G_o + 0.156 \ln\left(1 + S_g^2\right) \pm \sigma\sqrt{x^T (X^T X)^{-1} x}\, t_{\frac{a}{2},42} \tag{2.12}$$

$$\sigma^2 = 4.13 \times 10^{-4}, x^T (X^T X)^{-1} x$$

$$= \begin{pmatrix} 1 \\ \ln G_o \\ \ln\left(1 + S_g^2\right) \end{pmatrix}^T \begin{pmatrix} 80.2 & -23.1 & -1.85 \\ -23.1 & 7.33 & 0.145 \\ -1.85 & 0.145 & 3.62 \end{pmatrix} \begin{pmatrix} 1 \\ \ln G_o \\ \ln\left(1 + S_g^2\right) \end{pmatrix} \times 10^{-2}$$

where $\dot{r}$ in [mm/s] and $G_o$ in [kg/m²s] are assumed. In Figure 2.3, the median of the fuel regression rates and its limits of the PI and CI in $\pm 3\sigma$ in normal distribution are compared with the experimental results. Figure 2.4 shows the uncertainty model in the CI

$\sigma\sqrt{x^T(X^TX)^{-1}x}$. As is in the case of the axial hybrids using WAX+GOX, the errors of the CI and PI take the minimum values at the averaged conditions of the burning experiments.

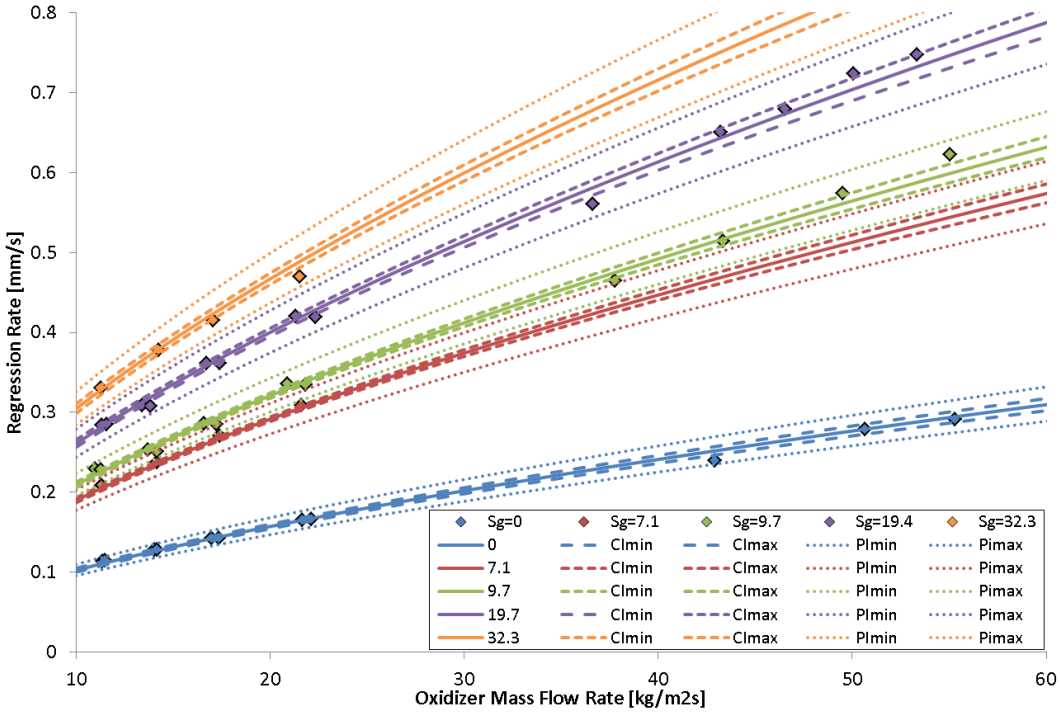


Figure 2.3. Comparison of CI and PI of the regression rate characteristics of SOFTs using PMMA+GOX with the previous experimental results.

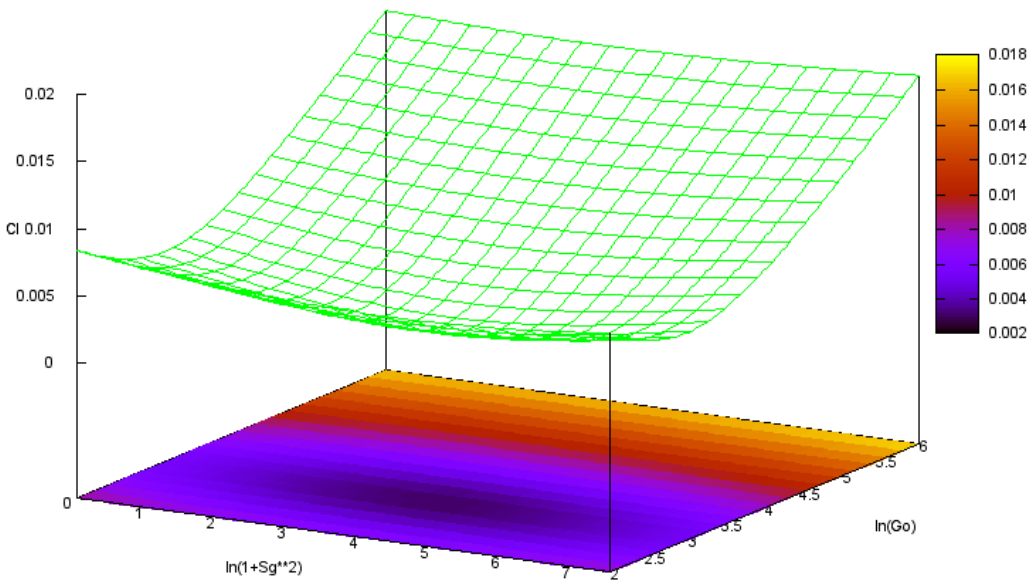


Figure 2.4. Plot of the uncertainty model of the CI of the SOFTs using PMMA+GOX.

2.1.1.2. Median Fuel Regression Model

The median fuel regression model of the SOFTs assuming WAX+GOX consists of the baseline axial model and the sensitivity of regression rates to geometric swirl number. As mentioned in the section 2.1.1.1, the former comes from the result of the axial hybrids using WAX+GOX in Eq. (2.11) and the latter is taken from that of the SOFTs using PMMA+GOX in Eq. (2.12). Therefore, the median model is expressed as

$$\dot{r} = \exp(-2.22)\, G_o^{0.640}\left(1 + S_g^2\right)^{0.156} \tag{2.13}$$

where $\dot{r}$ in [mm/s] and $G_o$ in [kg/m2s] are assumed.

2.1.1.3. Fuel Regression Model Including Systematic Errors

When an error model on the fuel regression behavior of SOFTs assuming WAX+GOX is built, a problem of how to build covariance matrix using both the results occurs. In this research, all the components in the covariance matrix of WAX+GOX in Eq. (2.11) are used as they are because originally no information about those related to the exponent $m$ in Eq. (2.4) is included in the first $2 \times 2$ matrix in $(X^T X)^{-1}$ in Eq. (2.12). On the other hand, the remained components of the covariance matrix related to geometric swirl number is adopted from Eq. (2.12) because these remained components in the covariance matrix are required to have information about the correlations on $m$. Therefore, the confidential interval model of the artificial fuel regression behavior on SOFTs assuming WAX+GOX is modelled as

$$\dot{r} = \exp(-2.22)\, G_o^{0.640}\left(1 + S_g^2\right)^{0.156} \exp\left(\pm\sqrt{x^T A x}\, t_{\frac{\alpha}{2},67}\right) \tag{2.14}$$

$$x = \begin{pmatrix} 1 \\ \ln G_o \\ \ln\left(1 + S_g^2\right) \end{pmatrix}, A = \begin{pmatrix} a_{11} & a_{12} & a_{13} \\ a_{21} & a_{22} & a_{23} \\ a_{31} & a_{32} & a_{33} \end{pmatrix}$$

$$\begin{pmatrix} a_{11} & a_{12} \\ a_{21} & a_{22} \end{pmatrix} = \sigma_{WAX}^2 (X_{WAX}^T X_{WAX})^{-1}$$

$$a_{31} = a_{13} = \sigma_{PMMA}^2 [(X_{PMMA}^T X_{PMMA})^{-1}]_{(1,3)}$$

$$a_{32} = a_{23} = \sigma_{PMMA}^2[(X_{PMMA}^T X_{PMMA})^{-1}]_{(2,3)}$$

$$a_{33} = \sigma_{PMMA}^2[(X_{PMMA}^T X_{PMMA})^{-1}]_{(3,3)}$$

are determined. Figure 2.5 shows the error model $\sqrt{x^T A x}$. The size of the error is slightly larger over all the operational range than that of the SOFTs using PMMA+GOX, and the operating point to minimize the error shifts to larger oxidizer mass flux.

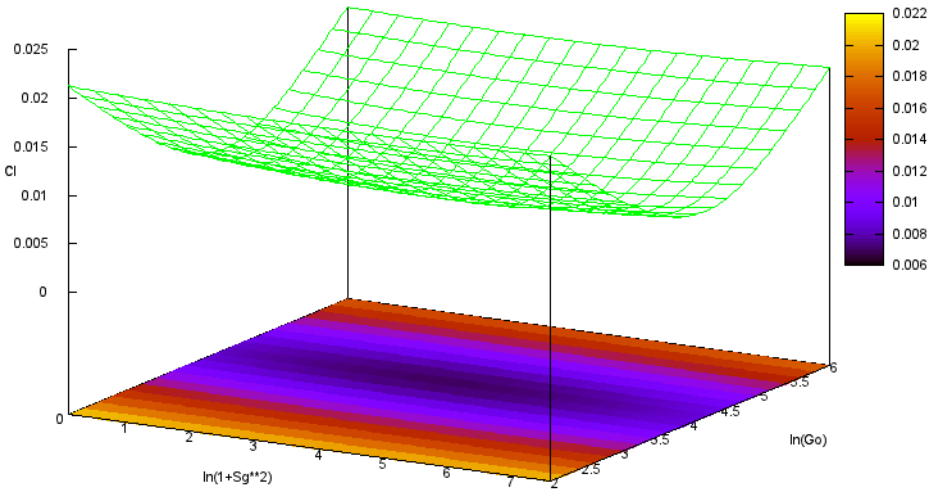


Figure 2.5. Plot of the artificial error model of the CI of the SOFTs assuming WAX+GOX.

In this research, confidential interval was used as the systematic error model in the practical simulations. This is because systematic errors should be residual after subtraction of random errors subject to the normal distribution, and the definition of confidential interval is similar to that of systematic errors in terms of errors of median models. However, we should emphasize that these two models originally have different concepts. In the practical simulations, the 67th t-distribution is adopted as the deviation model.

2.1.1.4. Fuel Regression Model Including Random Errors

In this chapter, a prediction interval model is used for the fuel regression model including random errors. It is easier to determine the random error models after modelling the confidential interval because the variance $\sigma^2$ in Eq. (2.9), which is added into the error model of the confidential interval, is the only new parameter to be determined. It seems to be appropriate to adopt $\sigma_{WAX}^2$ from the aspects of scales of regression rates and numbers of

experiments. In this fuel regression model, pseudorandom progression between -1 and +1 of the normal distribution is applied instead of those of t-distribution for simplicity of the program. The pseudorandom progression subject to the normal distribution is transformed from the uniform ones yielded by the intrinsic subroutine in Fortran 90. The transformation method is the Box-Muller transformation[9]. The fuel regression model including the random error model is expressed as

$$\dot{r} = \exp(-2.22)\, G_o^{0.640}\left(1 + S_g^2\right)^{0.156} \exp\left(s\sqrt{\sigma_{WAX}^2 + x^T A x}\right) \tag{2.15}$$

where $s$ refers to the pseudorandom error subject to the normal distribution of $\sigma = 1$.

2.1.2. Ideal Combustion Model

In this flight simulation, after calculating chemical equilibrium of the gasified fuel and oxidizer as the ideal combustion, ideal characteristic velocity is multiplied by c* efficiency to reflect combustion efficiency. In this subsection, the ideal combustion model is explained.

The thermodynamic data of 1-octene $C_8H_{16}$ in "thermo.inp" in NASA CEA[10] is substituted instead of the ones of paraffin wax fuel. Chemical equilibrium states are calculated by solving minimization problem of Gibbs Energy[10]. Reaction products are assumed to consist of the 11 species of $CH_4$, $O_2$, $H_2O$, $CO_2$, $H_2$, CO, OH, O, H, $C_2H_2$ and C (solid graphite). The first 9 species is often assumed in CFDs handling chemical reaction of hydrocarbon and oxygen assuming local chemical equilibrium states. In addition to this set, the latter two species are added because fuel-rich productive gases of equivalent ratios larger than 5 often contain relatively large molecular fractions of these two species. The thermodynamic data of all these chemical species are quoted from "thermo.inp" in NASA CEA[10].

At the begging of the subroutine of the ideal combustion model, in addition to a given oxidizer mass flow rate, chamber pressure is temporarily given. From these parameters, O/F ratio is determined from the following equation as

$$\frac{O}{F} = \frac{\dot{m}_o}{2\pi\rho_f \dot{r} r_p^2} \tag{2.16}$$

where $r_p$ and $\rho_f$respectively refer to fuel port radius and density of the solid fuel. After calculating chemical equilibrium, "equilibrium specific heats" and "ratio of specific heat"[10] are also calculated to validate a choking condition and to use for engine performance calculations. The detailed analytical procedures to minimize Gibbs Energy and to calculate the thermodynamic parameters are explained in the reference[10].

Under the thermodynamic state at the calculated chemical equilibrium, chamber pressure is iterated to balance the propellant mass flux at the nozzle throat from the given oxidizer mass flow rate and the one calculated from the given pressure. The latter can be calculated from the choking condition as

$$G_t = \frac{p_c}{\sqrt{RT_c}}\sqrt{\gamma\left(\frac{2}{\gamma+1}\right)^{\frac{\gamma+1}{\gamma-1}}} \tag{2.17}$$

where $\gamma$ is ratio of specific heat, $R$ is gas constant and $T_c$ is combustion chamber temperature in a chemical equilibrium state.

2.1.3. C* Efficiency Evaluation Model

In solid and liquid propulsion, a conceptual chamber length parameter $L^*$ is used to evaluate c* efficiency[11]. This method is called "L* theory", and is based on the assumption that the diffusion time scales and are smaller than or in the same order of magnitude of the gaseous phase kinetic time scale in well-designed solid or liquid propulsion, therefore, reaction rates limit chemical reaction, and this method evaluates residence times of propellants to reach chemical equilibrium.

In the L* theory of liquid or solid propulsion, propellants injected into a combustion chamber need a residence time $\tau_{stay}$ to perfectly reach chemical equilibrium in the combustion chamber. The ideal residence time $\tau_i$ can be expressed with the ideal chamber volume to reach chemical equilibrium $V_{c_i}$ and operational conditions of chamber density $\rho_c$, propellant mass flow rate $\dot{m}$, nozzle throat area $A_t$ and mass flux at nozzle throat $G_t$ as

$$\tau_i = \frac{V_{c_i}}{\dot{m}/\rho_c} = \left(\frac{V_c}{A_t}\right)_i \frac{\rho_c}{G_t} \tag{2.18}$$

where $V_c/A_t$ refers to $L^*$. Using the ideal gas state equation and the choking condition at

the throat Eq. (2.17), Eq. (2.18) can be transformed into the following equation as

$$L_i^* = \tau_i \sqrt{\gamma R T_c \left(\frac{2}{\gamma+1}\right)^{\frac{\gamma+1}{\gamma-1}}} \qquad (2.19).$$

This equation shows the method to calculate $L_i^*$ because if $\tau_i$ is given, the other valuables have been already known in the last section. Note that $L_i^*$ should depend on O/F ratio and throttle ratio because thermodynamic state and properties to determine $L_i^*$ depend on them. If the gaseous residential time is assumed to be proportional to $L^*$ (this assumption implies that the gaseous velocity in a combustion chamber is a constant independent of O/F ratio), real-to-ideal $L^*$ ratio should be similar to real-to-ideal residence time ratio as

$$\tau_{stay}/\tau_i = L^*/L_i^* \qquad (2.20)$$

where $\tau_{stay}$ refers to a practical residence time scale. This simple assumption can be validated with a set of experimental results on the hypergolic liquid rocket engines[11]. The propellants in this series of experiments were the pair of $N_2O_4$ and Aerozine-50. Assuming the largest $c^*$ at the largest $L^*$ in the experimental results as the ideal results and $L^*$, the relation between $c^*$ efficiency $\eta_{c^*} = c^*/c_i^*$ and $L^*/L_i^*$ can be described in Figure 2.6. If the combustion reaction is subject to first order chemical reaction and c* efficiency is proportional to the density of the products, the fitting curve of c* efficiency should be expressed as

$$\eta_{c^*} = \frac{c^*}{c_{ref}^*} = 1 - \exp\left(-a\frac{L^*}{L_{ref}^*}\right) \qquad (2.21)$$

where $a = 6.6$ fit the experimental results well.

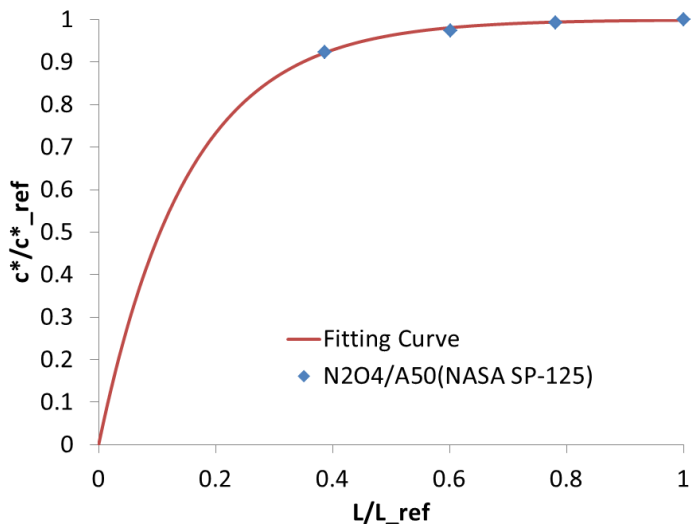


Figure 2.6. Comparison between the fitting model and the experimental results[11] of c* efficiency of the liquid propulsion using $N_2O_4$ and Aerozine-50.

The prior explanations focused on L* theory determined by the gaseous kinetic timescales of chemical reaction in liquid and solid propulsion. Practically, the gaseous kinetic timescales directly related with $\tau_i$ in liquid or solid propulsion is estimated[12] in the order of magnitude of $10^{-3}$ [s]. However, in hybrid rocket propulsion, the existing researches said that chemical reaction in boundary layer combustion is determined by the diffusion timescale in turbulent boundary layer[12]. The diffusion timescale is 10 times larger than the gaseous kinetic timescale[12] as

$$\tau_i \sim \begin{cases} 10^{-2}[s] & \text{(Diffusion timescale)} \\ 10^{-3}[s] & \text{(Gaseous kinetic timescale)} \end{cases} \tag{2.22}$$

Moreover, the system of the function in Eq. (2.21) is based on the reaction rate limiting theory, and originally this system is not applicable to boundary layer combustion. Therefore, even the modelling of L* theory applicable to hybrid propulsion should be an important work because no alternative theoretical evaluation of the c* efficiency applicable to hybrid rocket propulsion was found. In this chapter, for simplicity, Eq. (2.11) of 10 times larger $L_i^*$ for the liquid propulsion is adopted as the c* efficiency model for hybrid rocket propulsion.

As is in the case of the liquid propulsion, this model is also validated with a set of experimental results. The only existing research we found about the dependence of c* efficiency in hybrids on chamber length without any mixing enhancers is the firing experiments using WAX+GOX reported by Nakagawa et al.[13] Figure 2.7 shows a comparison

of normalized $c^*$ and $L^*$ between our model and the experimental data. In the evaluation model, half length of the practical fuel port is used for the calculations of c* efficiency because the center of the fuel port grain is located at the half length from the head end of the fuel port. All the experimental conditions of $L^*$ were so smaller than the estimated $L_i^*$ and located in the range less than $0.4L_i^*$. The result of our model had a good agreement with the experimental results in the low $L^*/L_i^*$. The model curve crossed with the experimental c* efficiency in the middle of the experimental conditions, exceeded those in the larger experimental conditions, and continued to approach to 1. The gaps between our model and the experimental results seemed to be due to the c* efficiency model not assuming boundary layer combustion or lack of considerations on other phenomena related to c* efficiency such as heat loss.

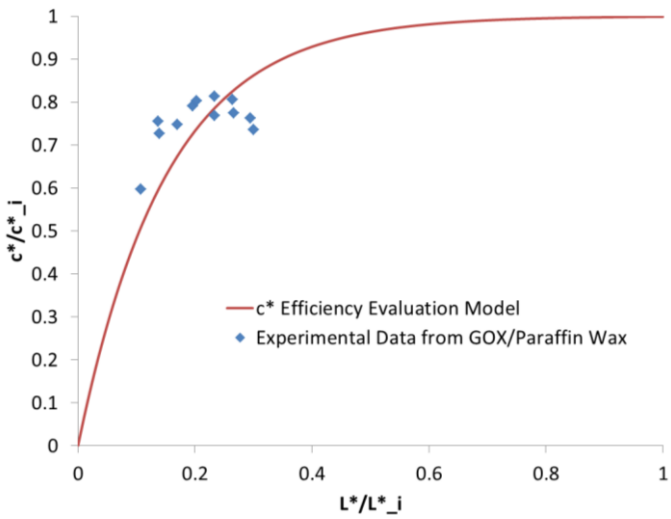


Figure 2.7. Comparison of c* efficiency model Eq. (2.21) with the experimental results[13].

In this research, there are several problems from the theoretical aspects, but as the first step to research c* efficiency model in hybrid propulsion, the following c* efficiency model is applied as

$$\eta_{c^*} = \frac{c^*}{c_i^*} = 1 - \exp\left(-6.6\frac{L^*}{L_i^*}\right) \tag{2.23}$$

$$c_i^* = \frac{p_c}{A_t \dot{m}} \tag{2.24}$$

$$L_i^* = 10^{-2}\sqrt{\gamma R T_c \left(\frac{2}{\gamma+1}\right)^{\frac{\gamma+1}{\gamma-1}}} \tag{2.25}$$

$$L^* = \frac{\pi r_p^2 L_p}{2A_t} \tag{2.26}$$

where $L_p$ and $r_p$ respectively refer to fuel port length and radius. Moreover, we should note that c* efficiency is practically affected also by the mixing effects of swirling flows. However, this effect is not modelled in our engine model.

### 2.1.4. Nozzle Throat Erosion Model

Erosion rates of carbon nozzle throat in hybrid rocket propulsion are said to be larger than solid propulsion because molecular fractions of chemical species oxidizing graphite or carbon composites are larger than ones in solid propulsion. The experimental results[14,15] using GOX or LOX and the solid fuels mainly consisting of polycyclopentsdiene, HTPB and a curative reported that the erosion rates of the throat made of graphite or carbon-carbon were up to 0.97[mm/s]. The chamber pressure and O/F ratio respectively varied between 1.5 and 7[MPa] and between 1.1 and 3.3. Throat erosion rate mainly depends on chamber pressure (or mass flux at the throat) and O/F ratio because throat erosion rate is considered to be determined by the balance between the oxidizing gaseous supplies by molecular diffusion in molecular density boundary layer and reaction rates at the wall[16] as is shown in Figure 2.8.

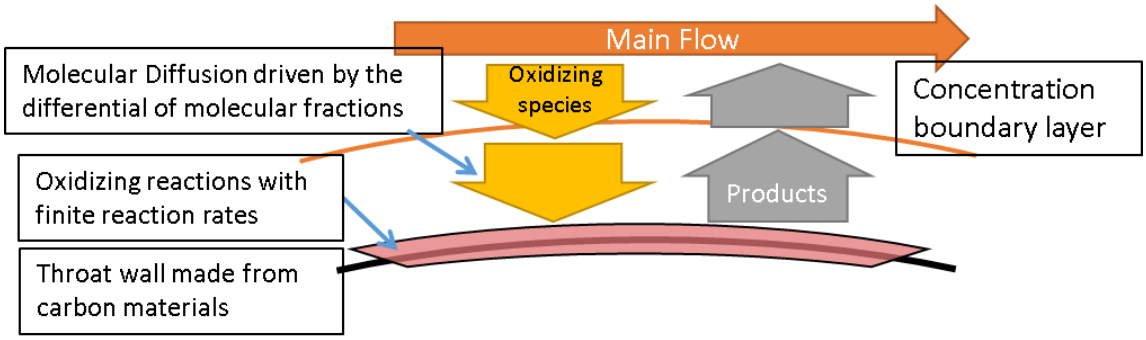


Figure 2.8. Schematics of the nozzle throat erosion model.

In the field of solid rocket propellant including hydrocarbon fuel, chemical erosion of nozzle throat at thermal equilibrium state in combustion flows is dominated by the following 5 chemical reactions[17] as

$$\begin{cases} \mathrm{C(s)} + \mathrm{CO_2} \rightarrow 2\mathrm{CO} \\ \mathrm{C(s)} + \frac{1}{2}\mathrm{O_2} \rightarrow \mathrm{CO} \\ \mathrm{C(s)} + \mathrm{H_2O} \rightarrow \mathrm{CO} + \mathrm{H_2} \\ \mathrm{C(s)} + \mathrm{OH} \rightarrow \mathrm{CO} + \mathrm{H} \\ \mathrm{C(s)} + \mathrm{O} \rightarrow \mathrm{CO} \end{cases} \tag{2.27}$$

In this thesis, the evaluation of molecular flux to the graphite wall at the nozzle throat in solid propulsion by Delaney et al.[16] is adopted. This is because this model is simple enough to be coupled with the reaction rate models explained in the following paragraph. Moreover, this model enables us to reflect the effects of O/F shifts on nozzle throat erosion rates because molecular fluxes of individual oxidizing species are evaluated. In their model, molecular fluxes of individual species are evaluated from the one dimensional Fick's law[16] as

$$N_i = -cD_{i\,gas}\frac{dx_i}{dz} + x_i(N_i + N_k) \tag{2.28}$$

where the subscripts $i$ and $k$ respectively refer to oxidizing species $i$ and productive species $k$, and $c$, $N$ and $x$ respectively refer to molecular density, molecular flux and molecular fraction, and $D_{i\,gas}$ is binary diffusion coefficient between oxidizing species $i$ and the combustion gas. Originally, the second term in the right hand should be the total molecular flux of all the species, but simplified in this form in the reference[16] in order to solve the equations for the individual species. In the reference[16], $D_{i\,gas}$ is assumed to be equal to $D_{ia}$, one between species $i$ and the air. $D_{ia}$ is evaluated from the kinetic theory of ideal gases[18] as

$$\begin{cases} D_{i\,gas} = 2.6280\times10^{-7}\dfrac{T_n^{1.5}\left(\frac{M_i+M_{air}}{2M_iM_{air}}\right)^{1/2}}{p_n\sigma_{i\,air}^2\Omega_{i\,air}^{(1,1)*}} \\ \sigma_{ij} \approx \frac{\sigma_i+\sigma_{air}}{2}, \Omega_{ij}^{(1,1)*} \approx 1.07\left\{\frac{kT_n}{\sqrt{\varepsilon_i\varepsilon_{air}}}\right\}^{-0.159} \end{cases} \tag{2.29}$$

where $\sigma_i$ and $\varepsilon_i/k$ are quoted from the reference[19]. In practical calculations, $1.05T_n$ is used for Eq. (2.29) instead of throat temperature $T_n$ to model recovery temperature in boundary layer. The exact solution of Eq. (2.28) is expressed as

$$N_i = \begin{cases} \frac{cD_{i\,gas}}{\delta}\ln\left(\frac{1+x_{i0}}{1+x_{iw}}\right) & (\mathrm{O_2, CO_2, H_2O, OH}) \\ \frac{cD_{i\,gas}}{\delta}(x_{i0} - x_{iw}) & (\mathrm{O}) \end{cases} \tag{2.30}$$

where the subscripts $0$ and $w$ refer to boundary conditions at the outer edge and the wall, and $\delta$ refers to concentration boundary layer thickness. The boundary conditions at the outer edge are given from the results of the Gibbs Energy minimization at the sonic condition using the scheme mentioned in the section 2.1.2. $\delta$ can be evaluated from the Gilliland-Sherwood equation[20] as

$$\frac{D}{\delta} = 0.023 Re^{0.81} Sc^{0.44} \tag{2.31}$$

where $Re = DG_t/\mu$ and $Sc = \mu/(D_{ia}\bar{M})$ are defined and $\bar{M}$ refers to the averaged molecular weight of the main flow.

On the other hand, according to the reference[21], mass flux of the oxidizing species reacting with the wall $G_{e_i}$ and reaction rate constants of carbon at the wall $k_i$ for oxidizing species $i$ are modeled as

$$\begin{cases} G_{e_1} = \frac{k_1 p_{O_2} Y}{1+k_2 Y} + k_3 p_{O_2}(1-Y) \\ Y = \left(1 + \frac{k_4}{k_3 p_{O_2}}\right)^{-1} \\ G_{e_i} = k_j p_i^{n_i} \ (i=2\sim5) \end{cases} \tag{2.32}$$

$$k_j = A_j T_w^{b_j} \exp\left(-\frac{E_j}{RT_w}\right) \tag{2.33}$$

where $A_j$, $b_j$, $E_j$ and $b_j$ are constants as is shown in Table 2.1. In this thesis, temperature at the wall $T_w$ is fixed to a constant in order to observe the dependence of the throat erosion rates on $T_w$.

Table 2.1. Heterogeneous rate constants and reaction order in oxidational reaction of graphite with $O_2$, $CO_2$, H2O, OH, and O.

| i | j | $A_j$ | $E_j$ [kj/mol] | $b_j$ | $n_i$ | i | j | $A_j$ | $E_j$ [kj/mol] | $b_j$ | $n_i$ |
|---|---|---|---|---|---|---|---|---|---|---|---|
| $O_2$ | 1 | $\mathbf{2.4 \times 10^3}$ | 125.6 | 0 | - | $CO_2$ | 5 | $\mathbf{9.0 \times 10^3}$ | 285 | 0 | 0.5 |
| | 2 | $\mathbf{2.13 \times 10^1}$ | -17.17 | 0 | - | $H_2O$ | 6 | $\mathbf{4.8 \times 10^5}$ | 288 | 0 | 0.5 |
| | 3 | $\mathbf{5.35 \times 10^{-1}}$ | 63.64 | 0 | - | OH | 7 | $\mathbf{3.61 \times 10^2}$ | 0 | -0.5 | 1.0 |
| | 4 | $\mathbf{1.81 \times 10^7}$ | 406.1 | 0 | - | O | 8 | $\mathbf{6.655 \times 10^2}$ | 0 | -0.5 | 1.0 |

In a quasi-steady state, these two phenomena should be balanced and all the molecular fluxes of the oxidizing species Eq. (2.30) are proportional to the carbon mass flux Eq. (2.32) at the stoichiometric mixture ratios Eq. (2.27). Therefore, the oxidizing gaseous supply and reaction should be balanced in the following equation as

$$\begin{cases} \frac{k_1 p_n x_{O^2w} Y}{1+k_2 Y} + k_3 p_n x_{O^2w}(1-Y) = 2M_c \frac{cD_{O^2gas}}{\delta} \ln\left(\frac{1+x_{O^2 0}}{1+x_{O^2w}}\right) \\ k_j (p_n x_{iw})^{n_i} = M_c \frac{cD_{i\,gas}}{\delta} \ln\left(\frac{1+x_{i0}}{1+x_{iw}}\right) \quad (\mathrm{CO_2}, \mathrm{H_2O}, \mathrm{OH}) \\ k_j (p_n x_{Ow})^{n_O} = M_c \frac{cD_{O\,gas}}{\delta} (x_{O0} - x_{Ow}) \end{cases} \tag{2.34}$$

where $M_c$ is molecular weight of carbon nozzle throat. From these equations, molecular fraction at the wall $x_{iw}$ is numerically calculated using the bisection method. Finally, throat erosion rate $\dot{r}_t$ is evaluated as

$$\dot{r}_t = \sum_{i=1}^{5} \frac{G_{ei}}{\rho_n} \tag{2.35}$$

where $\rho_n = 1.7 \times 10^3$[kg/m$^3$] is density of carbon nozzle throat.

In order to validate scales of the evaluated throat erosion rates, the results of our model were compared with those of the existing researches in hybrids. The previous work by Bianchi et al.[17] was found as the only research on the relation of throat erosion rates with O/F shifts. They used the computer fluid dynamics (CFD) to evaluate throat erosion rates. In their work, molecular diffusion and reaction rates are balanced, and heat flux into the nozzle was also evaluated in order to evaluate the nozzle temperature. Molecular diffusion is evaluated by the Fick's law, but a constant diffusion coefficients independent of chemical species were assumed. The heat balance of the nozzle assumed thermal conduction, heat convection assuming the Bartz's equation[11], chemical reaction, radiation and reradiation. The oxidizing reaction rates were modeled in the same way as in our model. As the initial conditions, it was assumed that Hydroxyl-terminated polybutadiene (HTPB) and GOX are used as the propellants, the chamber pressure is 1[MPa], and the nozzle throat diameter is 25.4[mm]. We should note that their work was not validated with the experimental results and there are other previous experimental results[14,15] showing larger erosion rates than the CFD results. However, their modeling was more precise from the aspects of temperature on the surface of the nozzle throat, and other thermal transport and diffusion phenomena. Therefore, their results deserve to be compared with those of our simpler evaluation.

Figure 2.9 shows the comparison of the nozzle erosion rates between the results of our model at $T_w$ =2000, 2250, 2500, 2750, 3000, 3250 and 3500[K] and the referential CFD results. Note that our calculation assumes paraffin wax and GOX as propellants and 1[MPa] in chamber pressure. The referential data show the dependence of erosion rate on O/F ratio, and the wall temperature of the referential data varies between 2400 and 2600[K]. Our results at $T_w$ =2000 and 2250[K] showed similar values and characteristics to the ones of the referential data along with mixture ratio. However, the erosion rates at $T_w$ =2500 and $T_w$ =2750[K] are respectively about 2 and 3 times larger than the referential data. The erosion rates in our results seemed to saturate between $T_w$ =2750 and 3000[K]. This seems to be because reaction rates are large enough compared to molecular diffusion playing a role to carry oxidizing species into the throat surface. Therefore, "molecular diffusion limited" can be assumed in this throat surface temperature range. Our model showed the peaks of the erosion rates exist at an equivalence ratio similarly to the referential data, and they shifts to oxidizer rich direction along with increasing mixture ratio. This seems to be because molecular supply of the oxidizing species directly reacts with the nozzle throat under the diffusion limited conditions. In this series of flight simulations, the wall temperature is fixed to 3000[K] in order to maximize the erosion rates on flight performances and their dependence on O/F shifts.

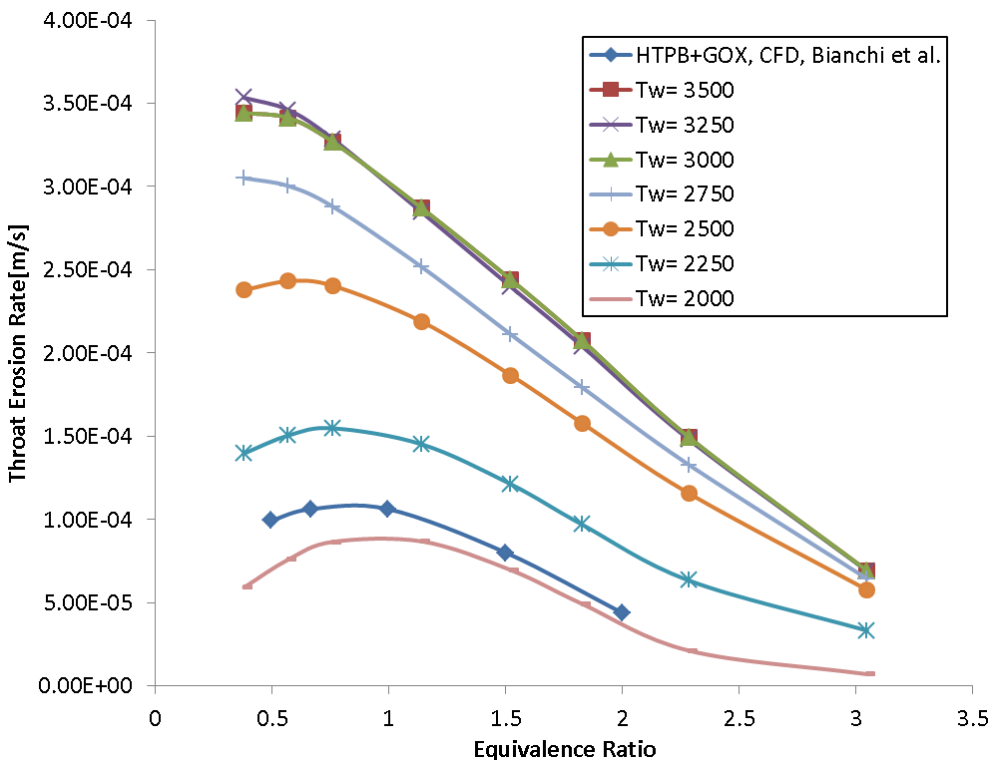


Figure 2.9. Validation of the nozzle throat erosion model with the CFD results[17].

2.1.5. Ideal Nozzle Model

The combustion flow through the nozzle is assumed to be frozen flow, and the nozzle exit pressure $p_e$ and thrust can be calculated from 1 dimensional nozzle theory[22] as

$$\frac{A_e}{A_t} = \left(\frac{p_e}{p_c}\right)^{-\frac{1}{\gamma}} \sqrt{\frac{\left(\frac{2}{\gamma+1}\right)^{\frac{\gamma+1}{\gamma-1}}}{\frac{2\gamma}{\gamma-1}\left\{1-\left(\frac{p_e}{p_c}\right)^{\frac{\gamma+1}{\gamma-1}}\right\}}} \tag{2.36}$$

and

$$F = \dot{m}u_e + (p_e - p_a)A_e = \dot{m}_{gas}u_e + (p_e - p_a)A_e + \dot{m}_{con}u_e$$

$$= A_t p_c \sqrt{\frac{2\gamma^2}{\gamma-1}\left(\frac{2}{\gamma+1}\right)^{\frac{\gamma+1}{\gamma-1}}\left\{1-\left(\frac{p_e}{p_c}\right)^{\frac{\gamma-1}{\gamma}}\right\}} + (p_e - p_a)A_e + \dot{m}_{con}u_e \tag{2.37}$$

where $A$, $F$, $\dot{m}$, $p$, $u$ and $\gamma$ respectively refer to area, thrust, mass flow rate, pressure, velocity and ratio of specific heat, and the subscripts $a$ $c$, $e$, $t$, $gas$ and $con$ refer to ambient, combustion chamber, nozzle exit, throat, gaseous phase and condensed phase. In this equation, the existence of condensed phase such as solid graphite is taken into account. The mass of condensed phase $\dot{m}_{con}$ with exhaust velocity $u_e$ also yields the thrust of $\dot{m}_{con}u_e$.

In this series of flight simulations, the expected flow separation pressure at the nozzle exit is evaluated using an empirical evaluation indicator [23] as

$$\frac{p_s}{p_a} = \frac{2}{3}\left(\frac{p_c}{p_a}\right)^{-0.2} \tag{2.38}$$

where $p_s$ refers to pressure starting flow separation. Through the flight simulations, the least values of the following indicator are recorded in individual flight simulations as

$$\min\left(\frac{p_e}{p_a} - \frac{p_s}{p_a}\right) \tag{2.39}$$

If this parameter has a negative value, the nozzle flow has a possibility to separate from the

nozzle exit during the flight.

## 2.2. Thrust Control Model

The mission scenario of this series of the flight simulations is vertical launches of single stage rockets, and this is similar to Goddard problem[24]. Goddard problem is to find the thrust curve to maximize the highest altitude under several ideal assumptions. The assumptions include the given mass of propellant, aerodynamic drag model $D$ dependent on velocity $v$ and altitude $z$, gravity acceleration $g(z)$, total rocket mass $m$ and propellant mass fraction. The rotation of the earth is ignored. If specific impulse is a given constant, this problem has an analytical solution. The analytical solution is derived by Tsien et al.[25] and this is expressed in a formulas to give a constraint to velocity as

$$\frac{Dv}{c} - D - mg + \frac{\partial D}{\partial v} v = 0 \qquad (2.40).$$

The thrust curve to maximize the highest altitude is to maintain this condition until all the propellants are spent out once Eq. (2.40) is fulfilled. Before this condition is fulfilled, the rocket should output the maximum thrust. In practical rockets, constant specific impulse is not a practical assumption in the atmosphere because nozzle performances depend on pressure ratio $p_c/p_a$. However, thrust curves derived from the Tsien's Goddard problem solution give far better flight performances than ones acquired from a constant throttle rate and are suitable to evaluate effects of O/F shifts on flight performances because typically these thrust curves include deep throttling. Moreover, this method is easy to calculate thrusts at the next time step. For these reasons, the Tsien's Goddard problem solution is adopted in our flight simulations.

Technically, the target thrust at the next time step cannot be directly calculated from Eq. (2.40). In order to calculate the next target thrust, using the time derivative of Eq. (2.40) and equation of the motion, next propellant mass flow rates should be derived. The equation of motion of the rocket is

$$m\dot{v} = -\dot{m}c - D - mg \qquad (2.41)$$

The time derivative of Eq. (2.40) and the equation of motion Eq. (2.41) can be summarized as

$$A(z,v,m)\frac{d}{dt}\begin{pmatrix} z \\ v \\ m \end{pmatrix} = f(z,v,m) \tag{2.42}$$

$$A(z,v,m) \equiv \begin{pmatrix} 1 & 0 & 0 \\ 0 & \frac{v}{c}\frac{\partial D}{\partial v} + \frac{D}{c} + v\frac{\partial^2 D}{\partial v^2} & -g \\ 0 & m & c \end{pmatrix}, f(z,v,m) \equiv \begin{pmatrix} v \\ -\frac{v^2}{z}\frac{\partial D}{\partial z} + v\frac{\partial D}{\partial z} - v^2\frac{\partial^2 D}{\partial v \partial z} \\ -D - mg \end{pmatrix}$$

where $D \equiv D(z,v)$ is assumed. Therefore, this set of the differential equations can be handled as a simultaneous ordinary differential equation as

$$\frac{d}{dt}\begin{pmatrix} z \\ v \\ m \end{pmatrix} = A^{-1}(z,v,m)f(z,v,m) \tag{2.43}$$

and this type of problems can be numerically solved with high accuracy by the fourth order Runge-Kutta method[26]. In this series of simulations, in order to fulfill the choke condition and yield more practical trajectories, the throttle range is limited between 10% and 100% of the maximum oxidizer mass flow rates. This throttle range seems to be broad enough for rockets of reasonable thrust-to-mass ratios to evaluate potential flight performances because practical rocket engines have more narrow throttle ranges.

In cases of O/F-controlled engines, O/F shifts are assumed to be eliminated by controlling geometric swirl number $S_g$. The target $S_g$ can be analytically calculated using the following condition derived from Eq. (2.4) as

$$\frac{O}{F} = \left(\frac{\dot{m}_o}{\pi}\right)^{1-n} \frac{{r_p}^{2n-1}}{a_0 \rho_f L}\left(1 + S_g^2\right)^{-m} \tag{2.44}$$

where $\rho_f$ refers to the density of the solid fuel grain. $S_g$ to fulfill the target O/F ratio is easily derived. If the solution $S_g$ is out of the controllable range, the nearest value from the solution is applied in the available range.

When fuel regression behavior has any systematic or statistical errors, a simple feedback control system of O/F ratio can correct these errors. In this feedback control system, the onboard computer is assumed to be able to acquire the remained masses of the oxidizer and the solid fuel. Practically, oxidizer consumption is observable using flow meters, and the remained solid fuel grain also conceptually can be estimated by locating several MIRRAS

elements[27] or ultrasound sensors[28] measuring the local solid fuel web thickness. Therefore, in O/F controlled cases, in order to minimize the residuals at the engine shutdown, the target O/F ratio is updated to the new one calculated from the remained propellants at each time step.

### 2.3. Conceptual Geometric Design of Sounding Rockets

Before the performance evaluations, "reasonable" geometries of hybrid sounding rockets should be conceptually designed. The components dominantly affecting the geometric designs of rockets are the oxidizer tank and the solid fuel grain. In this subsection, for the simplicity, regarding geometric swirl number and aspect ratio of solid fuel and oxidizer tank as design variables, reasonable geometries of sounding rockets are determined.

In this chapter, hybrid sounding rockets are assumed to have the same scale of the S-520 sounding rockets[1]. This is because it is easy to fit some specifications of the hybrid sounding rockets with those of the S-520 due to the open information on the S-520[1].

We selected paraffin wax and oxygen as the propellants, and we assumed oxygen is used in gaseous state but stored as liquid state. The liquid oxygen is assumed to be vaporized by any gas generators or regenerative cooling nozzles. The gross payload and the gross mass of the rocket are assumed to be 100[kg] and 2100[kg]. In this series of simulations, propellant mass ratio is also a given constant in order to simplify the determination of geometries though propellant mass ratio practically depends on the variables determining structural mass fraction[22] such as the maximum acceleration, dynamic pressure, the aspect ratio of the rocket, the maximum angle of attack, and alignment of thrust and components. In our rocket design, the range of aspect ratio of the rocket is also restricted between 8 and 12 because those of well-known single stage sounding rockets[22] are located in this range and this fact may suggest that this range gives "reasonable" structural coefficient, propellant mass ratio and flight performances. Initial port diameter to throat diameter ratio $\varphi_{in}$ is also an important parameter in this series of flight simulations because this parameter determines filling rates of the solid fuel and velocity of the productive gases in combustion chamber affecting propulsion performances[22]. From the aspect of the latter reason, lower limit of this design variable exists and practically $\varphi_{in}$ should be larger than $\sqrt{3}$. In this series, $\varphi_{in}$=2 is given. The maximum oxidizer mass flow rate $G_{o_{max}}$ should also be given. Large oxidizer mass flux gives advantage to the flight

performance because thrust density is improved and the condition of Eq. (2.40) in the Goddard problem solution is fulfilled earlier from the lift-off. However, this parameter has upper limit from the aspect of the "flooding phenomenon[27]" in hybrid rocket propulsion. Flooding phenomena refer to the difficulty of flame stabilization in higher oxidizer mass flux, and the lower limit to cause flooding depends on designs of engines. However, typical upper limits of instantaneous oxidizer mass flux in burning tests are said to be in the order of magnitude of 1000 [kg/m$^2$s][27]. In this series of simulations, $G_{o_{max}}$ of 350 [kg/m$^2$s] is given because the largest averaged $G_o$ is 368.7[kg/m$^2$s] in the burning tests of the large scale axial hybrids using WAX+GOX[7]. $G_{o_{max}}$ and the initial port cross-section area gives the maximum oxidizer mass flow rate from the requirement of the Goddard problem solution. The mass flow rates at the lift off is assumed to be the maximum throttle ratio. In the cases of the propellants, the optimal O/F ratio to maximize flight performances can be located between 1.7 and 2.5. In order to determine some of the design variables, O/F ratio of total propellants $(O/F)_{total}$ is temporarily fixed to 2 at this step.

Next, from the above given design variables, the possible range of the aspect ratio is roughly calculated. Initial port radius $r_{in}$ and outer radius $r_{out}$ of the solid fuel grain are expressed with throat radius $r_t$ as

$$\begin{cases} r_{in} = \varphi_{in} r_t \\ r_{out} = \varphi_{out} r_t \end{cases} \tag{2.45}$$

where $1 < \varphi_{in} < \varphi_{out}$ should stand. Using port length $L_{sf}$ and densities of paraffin wax $\rho_{sf}$ and liquid oxygen $\rho_o$, the masses of solid fuel grain $m_f$ and oxidizer $m_o$ can be expressed as

$$\begin{cases} m_f = \pi \rho_{sf} (\varphi_{out}^2 - \varphi_{in}^2) r_t^2 L_{sf} \\ m_o = \rho_o \pi \varphi_{out}^2 r_t^2 L_o \end{cases} \tag{2.46}$$

From Eq. (2.44), O/F ratio of the productive gas at ignition can be expressed as

$$\left(\frac{O}{F}\right)_i = \frac{\varphi_{in} r_t G_{o_{max}}^{1-n}}{2\rho_{sf} a_0 (1+S_g^2)^m L_{sf}} \tag{2.47}$$

Eliminating solid fuel length $L_{sf}$ in Eq. (2.47) with Eq. (2.46) yields throat radius as

$$r_t = \left\{ \frac{2a_0\left(1+S_g^2\right)^{n_s} m_f\left(\frac{O}{F}\right)_i}{\pi\left(\varphi_{out}^2-\varphi_{in}^2\right)\varphi_{in} G_{o_{max}}^{1-n_o}} \right\}^{\frac{1}{3}} \quad (2.48).$$

Using Eqs. (2.46) and (2.47), the total aspect ratio of the fuel grain and the oxidizer tank $AR$ can be expressed as

$$AR = \frac{L_{sf}+L_o}{2r_{out}} = \frac{\varphi_{in} G_{o_{max}}^{1-n}}{4\left(\frac{O}{F}\right)_i \rho_{sf}\varphi_{out} a_0\left(1+S_g^2\right)^m} + \frac{\frac{\varphi_{in}}{\varphi_{out}}\left\{1-\left(\frac{\varphi_{in}}{\varphi_{out}}\right)^2\right\} G_{o_{max}}^{1-n}}{4\rho_o a_0\left(1+S_g^2\right)^m} \quad (2.49)$$

where $(O/F)_{total} = (O/F)_i$ is assumed. If $I_{sp}$, $S_g$ and $AR$ are given, $\varphi_{in}/\varphi_{out}$ is determined and initial thrust $F_0$ is roughly expressed as

$$F_0 = \frac{\pi G_{o_{max}} \varphi_{in}^2 r_t^2}{1+\left(\frac{O}{F}\right)_i} I_{sp} g \quad (2.50)$$

where $I_{sp}$ at sea level of 280[s] is temporarily assumed. The given design variables are summarized in Table 2.2.

Table 2.2. The given variables in the design of single stage A-SOFT sounding rocket.

| | | | |
|---|---|---|---|
| Propellants | WAX + LOX(storage condition) | $m_{rocket}$[kg] | 2000 |
| $\rho_o$[kg/m3] | 1140 (preserved in liquid state) | Structural coefficient | 3.5 |
| $\rho_{sf}$[kg/m3] | 760 | $\varphi_{in}$ | 2 |
| $a_0$ | $1.08 \times 10^{-4}$ | $G_{o_{max}}$[kg/m2s] | 350 |
| $n$ | 0.640 | $I_{sp}$[s] | 280(temporary) |
| $m$ | 0.156 | $(O/F)_{total}$ | 2 (temporary) |
| $m_{payload}$[kg] | 100 | | |

The initial geometric swirl number $S_g$ still remains to be an unknown variable. Practically, $S_g$ has physical limitations due to choking or large pressure loss at the injector ports. Therefore, it is realistic that the range of $S_g$ is between 0 and 50. Practically, small $S_g$ between 0 and 10 should be enough to fulfill the requirement of aspect ratios because the propellant combination of WAX+GOX has relatively large regression rates even in axial injection.

Figure 2.10 shows the relations among aspect ratios, inner port diameter and outer diameter. Figure 2.11 shows the relations between aspect ratio and initial acceleration. When aspect ratio $AR$ is regarded as a function of $\varphi_{in}/\varphi_{out}$, it has the maximum value at $\frac{\varphi_{in}}{\varphi_{out}} = \sqrt{\frac{1}{3}\left(1 + \frac{\rho_o}{\rho_{sf}(O/F)_i}\right)}$. The curves in these figures have their endpoints at the respective maximum aspect ratios. These figures say that there is wider options of aspect ratio in $S_g$= 0 but the initial thrust and acceleration are relatively low compared to existing sounding rockets such as S-520 due to small initial regression rates. Moreover, if $S_g$= 0 is applied, it is impossible to control O/F ratios toward oxidizer rich direction. In cases of $S_g$ ≥10, the possible design solutions give too small aspect ratios due to too large initial regression rates. Compared to the design of S-520 rockets, 6 [G] in the initial acceleration and 10.3 in the solid propellant aspect ratio, $AR$=8 and $S_g$=5 are considered to be good design parameters. The nozzle expansion ratio of 7 is also selected.

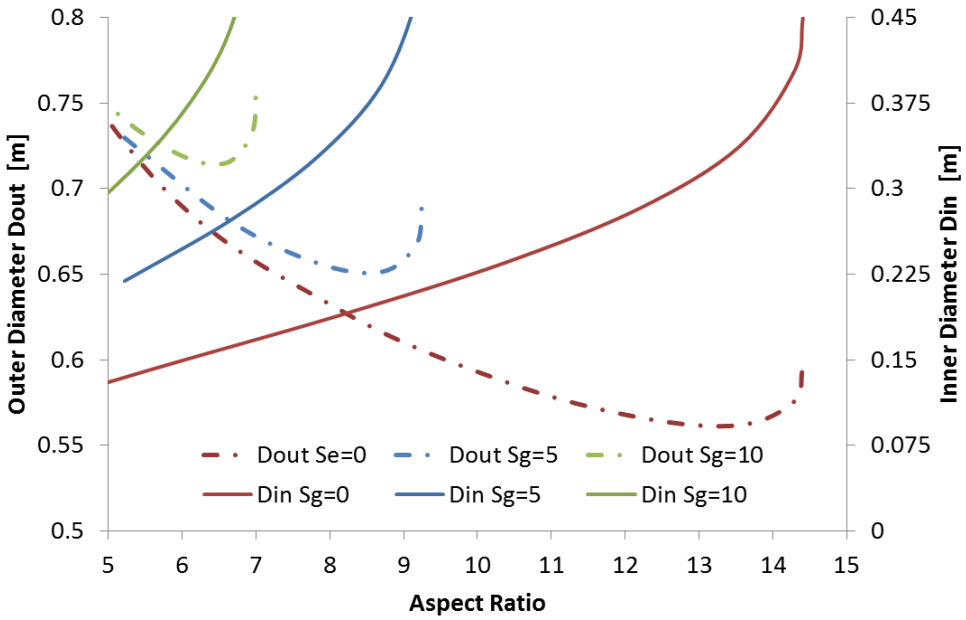


Figure 2.10. Relations among aspect ratios, inner port diameter and outer diameter in the hybrid sounding rocket design solutions.

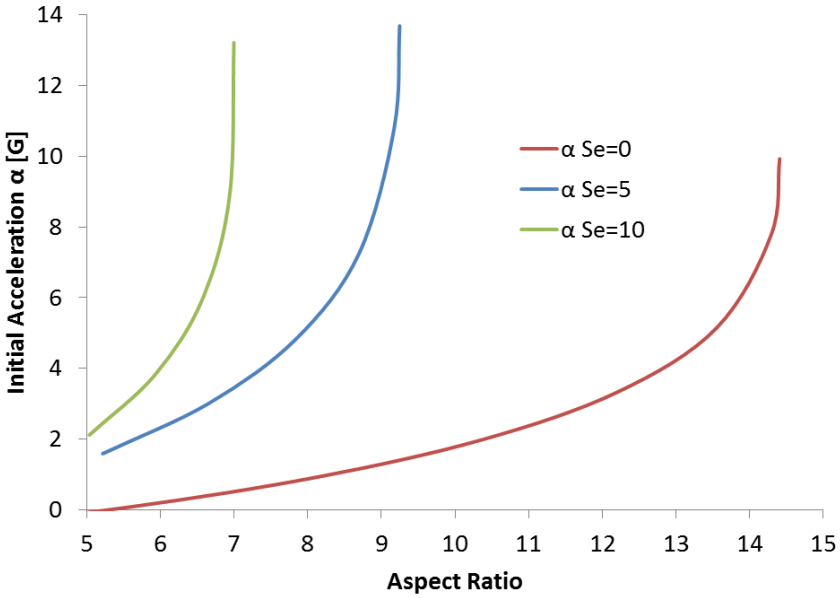


Figure 2.11. Relations between aspect ratios and initial thrust in the hybrid sounding rocket design solutions.

In the practical simulations, before the calculations of flight, fuel grain port diameter ratio $\varphi_{in}/\varphi_{out}$ is calculated from Eq. (2.49) using the given parameters above and the given $(O/F)_{total}$ equivalent to $(O/F)_i$. The throat diameter is calculated from Eq. (2.48). Finally, the lengths of the fuel grain and the oxidizer tank are calculated from Eq. (2.46). The design solutions in the cases of $(O/F)_{total} = 1.7\text{-}2.1$ are compared with the solid propellant design of S-520[1] in Figure 2.12.

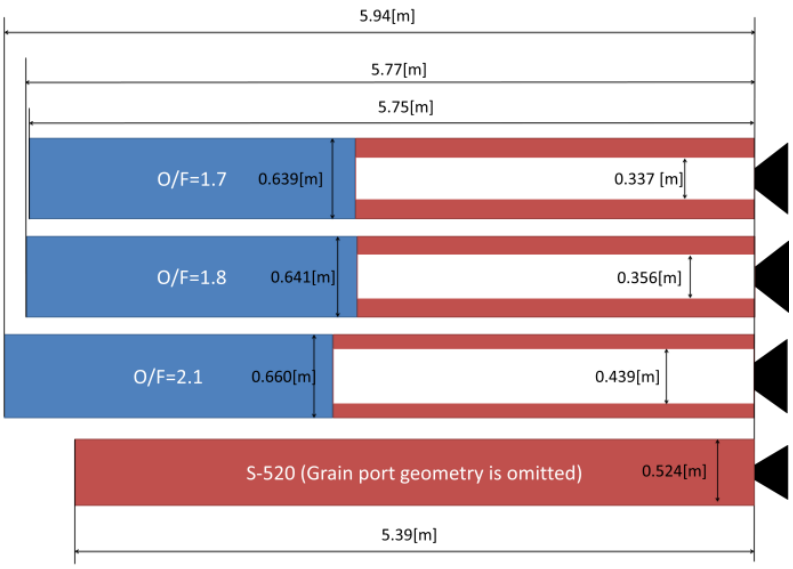


Figure 2.12. Schematics of the geometries of hybrid sounding rocket designs dependent on

total O/F ratios.

## 2.4. Environmental Models

The environmental model describes the ambient environment affecting the motion of rockets and consists of aerodynamic drag, ambient pressure to determine nozzle performance and gravity acceleration.

In our simulations, the simple drag model proposed by Akiba et al.[29] is adopted. The aerodynamic drag model consists of the following equations as

$$\begin{cases} D = D_0(v)\exp(-0.133\times 10^{-3}x) \\ D_0(v) = \frac{1}{2}\rho_0 v^2 S C_D \\ C_D = \begin{cases} 0.3(1+M^2)\ (M \le 1) \\ 0.3\left(1+\frac{1}{M^2}\right)\ (M > 1) \end{cases} \\ M = \frac{v}{a_0} \end{cases} \tag{2.51}$$

where $x$[m] is altitude, and $a_0$[m/s] and $v$[m/s] are respectively sonic velocity at sea level and velocity of rocket, and $D$[N] and $D_0$[N] respectively refer to aerodynamic drags at an altitude $x$ and at sea level. In Figure 2.13, the drag coefficient model is compared with the practical ones. The drag coefficient model is located between those of V-2 and Deacon sounding rocket. The adopted model showed in the middle of these practical data.

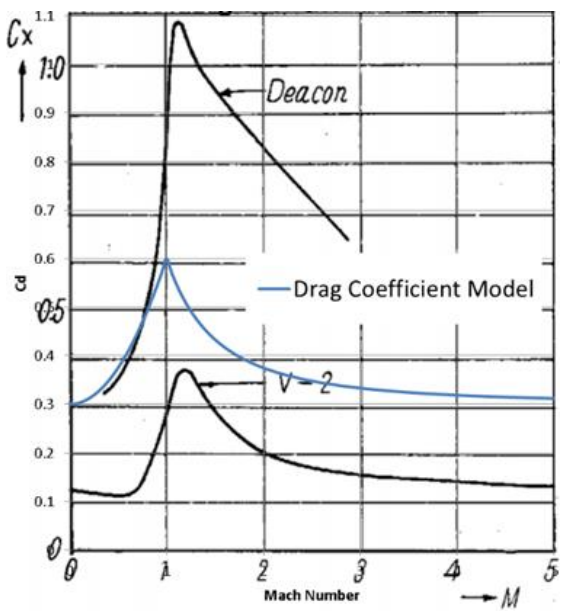

Figure 2.13. Comparison of the aerodynamic drag coefficients between the quoted model and the practical data[29].

As the ambient pressure model and the gravity model, International Standard Atmosphere (ISA) model[30] and gravitational acceleration at sea level of 9.80665 [m/s$^2$] are respectively adopted.

## 2.5. Calculation Diagram in the Flight Simulations

Figure 2.14 shows the diagram of the sounding rocket flight simulation program. First, from the dynamic state of the rocket at the time step, the program judge whether the dynamic state of the rocket fulfills the condition Eq. (2.40) to throttle under Eq. (2.42). If the dynamic state agrees with the condition, the optimal thrust is calculated from Eq. (2.43) and the oxidizer mass flow rate is calculated using the iteration including the nominal fuel regression model, Gibbs energy minimization, the choking condition, c* efficiency mode and the ideal nozzle theory. During this iteration, in O/F controlled cases, the optimal $S_g$ for the oxidizer mass flow rate is calculated from Eq. (2.44). This iteration continues until the choking condition agrees and the target thrust is acquired. After the oxidizer mass flow rate and $S_g$ are determined, the practical thrust is calculated. In this calculation, fuel regression errors are added if assumed. The acquired thrust is used for the time integration of the flight dynamics. If the dynamic state of rocket does not agree with the condition Eq. (2.40), the practical thrust is directly calculated with the maximum oxidizer mass flow rate. After the thrust calculation, the throat erosion rate is calculated using Eqs. (2.34) and (2.35). In this calculation, in order to know the molecular fraction in the main flow at the nozzle throat, Gibbs energy minimization of the gaseous products is calculated again assuming that the kinetic energy of the gas ${a_n}^2/2$ is subtracted from the unit mass total enthalpy at the combustion chamber. Finally, the dynamic states of the rocket such as height, velocity and acceleration are calculated by the time integration of the motion of the equation Eq. (2.41). At this step, the remained masses of the propellants, the fuel port diameter and the nozzle throat diameter are also timely integrated. These time integrations are calculated with the Euler method for the simplicity of the program. The timescale of our simulations is 0.01 [s] to compensate the low order of the time integration. At the end of the time step, the specific impulse of the engine at the 50% throttle ratio is calculated to be used for the target thrust calculation in the following time step. After either of the fuel or oxidizer runs out, only the flight dynamics is timely integrated until the altitude starts to decrease.

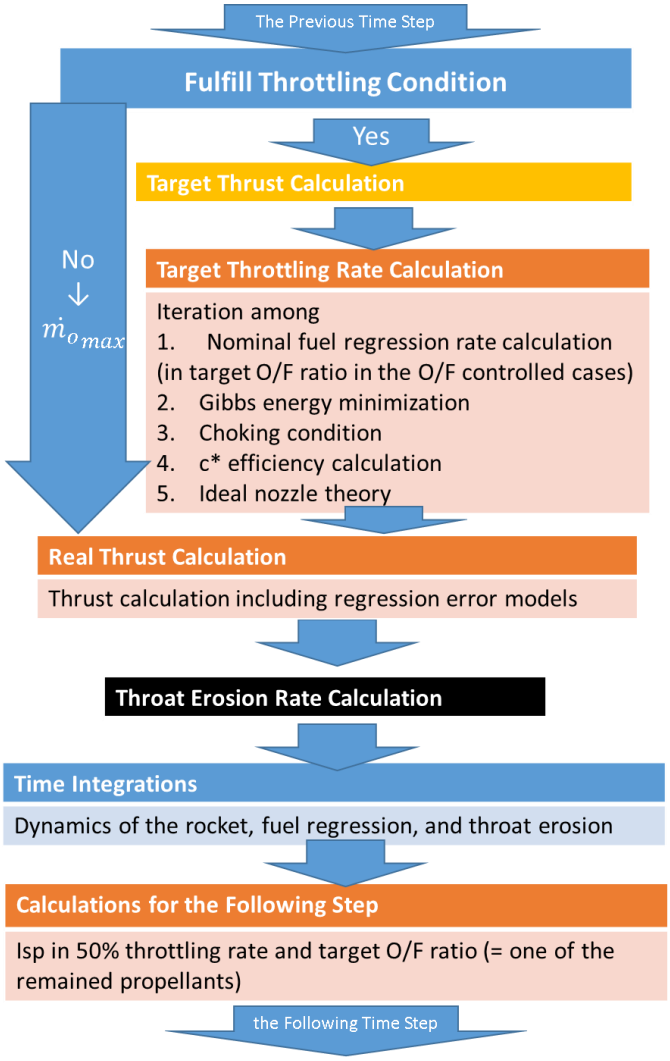


Figure 2.14. Diagram of the single stage sounding rocket flight simulation program.

## 2.6. Problem Settings

In this research, three sets of flight simulations are performed for the particular specific purposes. The main purpose for the first set is to evaluate the effects of the O/F shifts due to nominal fuel regression behavior Eq. (2.13) on the propulsion performances. The other purpose is to investigate the total O/F ratio to maximize the highest altitudes under this set of the given problem settings and the design criteria of the rocket. The target phenomena caused by O/F shifts to be evaluated are enthalpy shifts, throat erosion and c* efficiency. The total O/F ratio is varied between 1.7 and 2.1. In the flight simulations of the O/F-uncontrolled hybrids, the initial geometric swirl number is adjusted to consume both of the propellants at the engine shut down.

The purpose of the second set is to add the effects of O/F shifts caused by the systematic errors of the fuel regression behavior. The total O/F ratio is the fixed one to maximize the flight performance determined in the previous set of the simulations. The flight performances are calculated in several sizes of the systematic errors of the fuel regression behavior of WAX+GOX. The confidential interval of the regression rate behavior Eq. (2.14) is used for the systematic error model, and the size of the systematic errors is varied between $-3\sigma$ and $+3\sigma$.

The purpose of the last set of the flight simulations is to evaluate the effects of O/F shifts caused by the random errors of the fuel regression behavior. As explained in the prior subsection, the random errors subject to the normal distribution are added to the nominal regression rate behavior at every time step. The regression rate equation including random errors is the prediction interval Eq. (2.15). Because the regression errors are given randomly, it is necessary to repeat the simulation and acquire the statics of the performances. The flight simulations are repeated for 3000 times. This trial number is based on the probability of the appearance of $\pm 3\sigma$, and the probability of the appearance of $+3\sigma$ or $-3\sigma$ is 0.27%.

## 2.7. Results and Discussions

The simulations of the nominal fuel regression behavior and those with the systematic errors carried out without any calculation errors. However, in some cases of the simulations with the random errors, iteration errors occurred during engine performance calculations. These errors were found only in the iteration with bisection method to fulfill the choking condition, and in the final phases of the iteration of these cases, the chamber pressures of the two different oxidizer mass flow rates in bisection method reversed from the oxidizer mass flow rates. The reason for this error is possibly due to the empirical judgement conditions[10] in the iteration of chemical equilibrium. The latest version of NASA CEA[10] does not cause such errors, but the latest empirical judgement conditions of the Gibbs energy minimization could not be found. As the error processing, the throttle ratios are determined as the mean value of the two throttle ratios in the bisection method. Owing to this error processing, the flight simulations with the random errors of fuel regression behavior finally completed. In the following small sections, the results of the flight performances of the O/F controlled and uncontrolled hybrid rockets are discussed.

2.7.1. Nominal Performances

Figure 2.15 shows the highest altitudes and the averaged specific impulse of the results of the first set of the simulations, and the cases in $(O/F)_{total}$=1.9 had the best performances whether O/F ratio is controlled or not. The performance gaps between the O/F controlled cases and the O/F uncontrolled cases were relatively small. The highest altitude in the O/F controlled case in $(O/F)_{total}$=1.9 was 472.1[km] while the one in the uncontrolled case was 461.8[km], and the performance increase was by 2.2%. The averaged specific impulse in the O/F controlled case in $(O/F)_{total}$=1.9 was 288.2[s] while the one in the uncontrolled case was 285.1[s], and the performance improvement was by 1.1%.

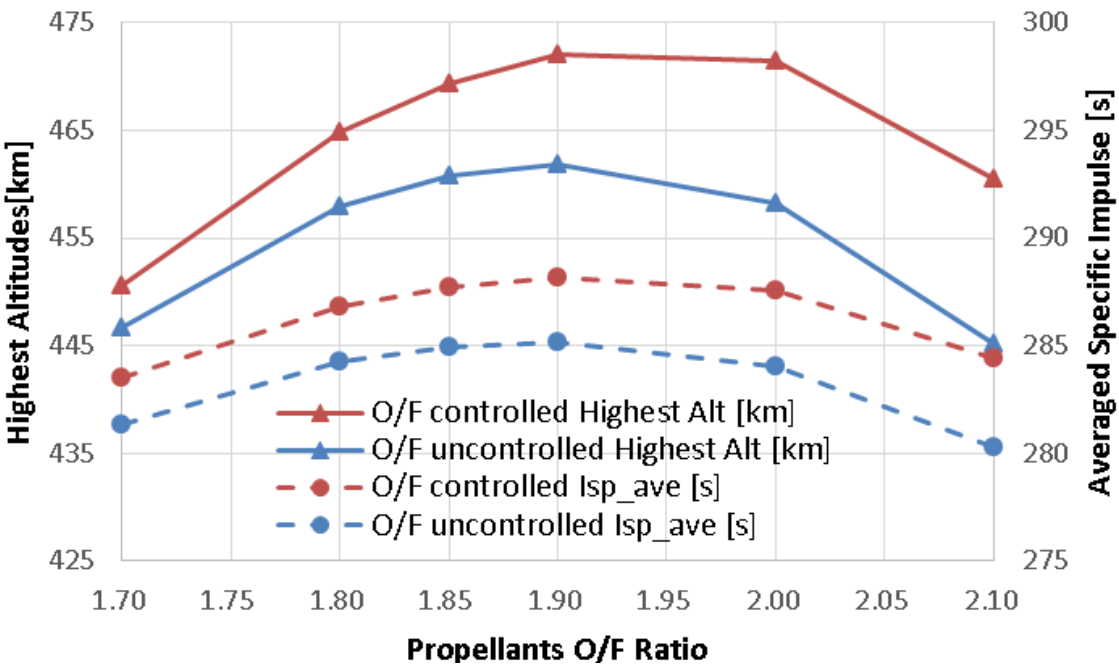


Figure 2.15. Comparison of the highest altitudes and time averaged specific impulse between the O/F controlled and O/F uncontrolled hybrid rockets under the nominal fuel regression behaviors.

Figure 2.16 shows the traces of instantaneous O/F ratio, c* efficiency and nozzle throat area of the O/F controlled/uncontrolled cases in $(O/F)_{total}$=1.9. c* efficiency in the both cases was always larger than 98 % and negligible difference between the two cases because the port volume is large enough for the ideal $L^*$. The throat areas at the end of the engine operations was also near to the same results between the two cases whereas there is a slight difference in the middle of the operation. At the beginning of the engine operations, in the O/F uncontrolled case, the engine operates in oxidizer richer conditions and has larger

throat erosion rates due to lower fuel regression rates. However, during throttling, the engine operates in fuel richer conditions, and the throat erosion rate decreased in the middle of the operation. At the end of the engine operation, the engine operates in 100% throttle again, and O/F ratio is larger than the averaged ones. This is the mechanism to cause the difference of the traces of the throat area between the O/F controlled and uncontrolled cases. The total throat areal expansion was by 20% in the both cases.

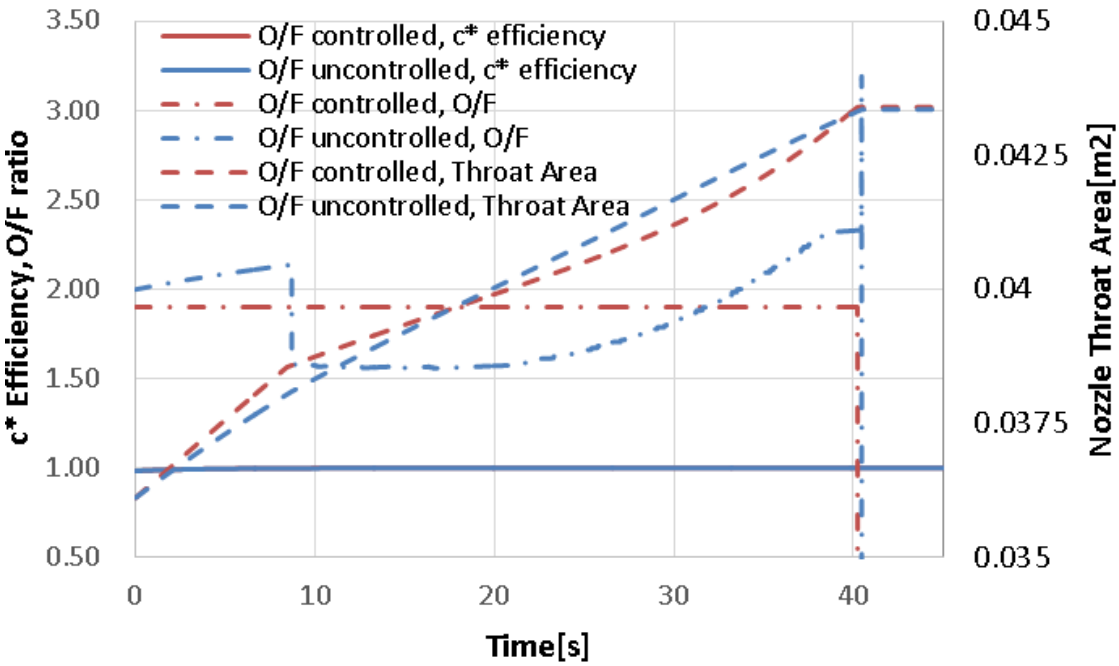


Figure 2.16. Comparison of the traces of instantaneous O/F ratio, c* efficiency and nozzle throat expansion in the flight simulations of O/F controlled and O/F uncontrolled hybrid rockets under the nominal fuel regression behaviors.

Figure 2.17 shows the traces of instantaneous oxidizer mass flow rates and specific impulse in the both O/F controlled and uncontrolled cases in $(O/F)_{total}$=1.9. There is slight difference between the two traces of oxidizer mass flow rate, but there is a clear performance gap in specific impulse in deep throttling. The instantaneous largest gap of specific impulse between the two cases was by 5.5% and located at 14[s]. This relatively large performance loss could not be observed in throat erosion or c* efficiency. Therefore, the performance loss seemed to be due to the enthalpy shift and the nozzle performance losses induced by the enthalpy shift.

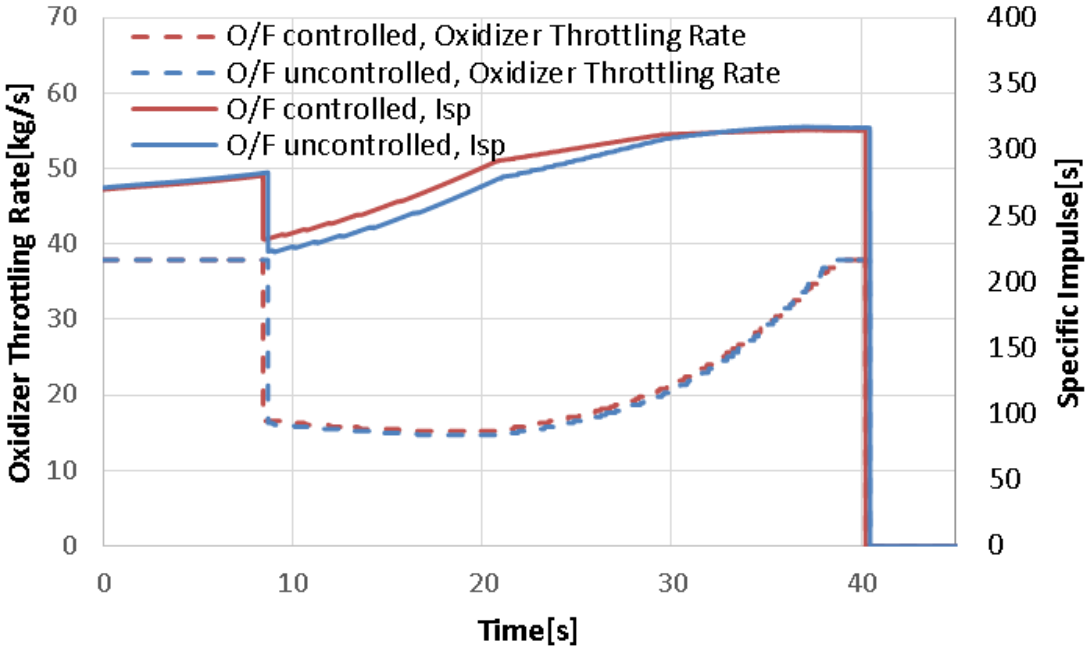


Figure 2.17. Comparison of the traces of the instantaneous oxidizer throttle ratio and specific impulse in the flight simulations of O/F controlled and O/F uncontrolled hybrid rockets under the nominal fuel regression behaviors.

Figure 2.18 shows the minimum values of Eq. (2.38) through the engine operations to evaluate the possibilities of nozzle flow separation. In the O/F controlled cases in the total O/F ratios larger than 1.9, nozzle flow separation can occur. In the best performance case of $(O/F)_{total}$=1.9, nozzle separation does not occur at least in the O/F controlled case. On the other hand, about the O/F uncontrolled cases, nozzle flow separation can occur during their operations in the cases of the total O/F larger than 1.8. Therefore, the nozzle expansion ratio of 7 is the most suitable for the O/F controlled case of $(O/F)_{total}$=1.9. The O/F uncontrolled cases of $(O/F)_{total}$=1.9 did not pass this design criteria for nozzle flow separation, but the duration of this parameter below 0 is just less than 2 [s] after the start point of the throttling, and the gap from the estimated nozzle separation pressure was at least by -8%. Moreover, during that time, heat flux is expected to be added into the nozzle flow from the nozzle structure heated in the 100% throttle. Therefore, the nozzle expansion ratio is not changed also in the following subsections.

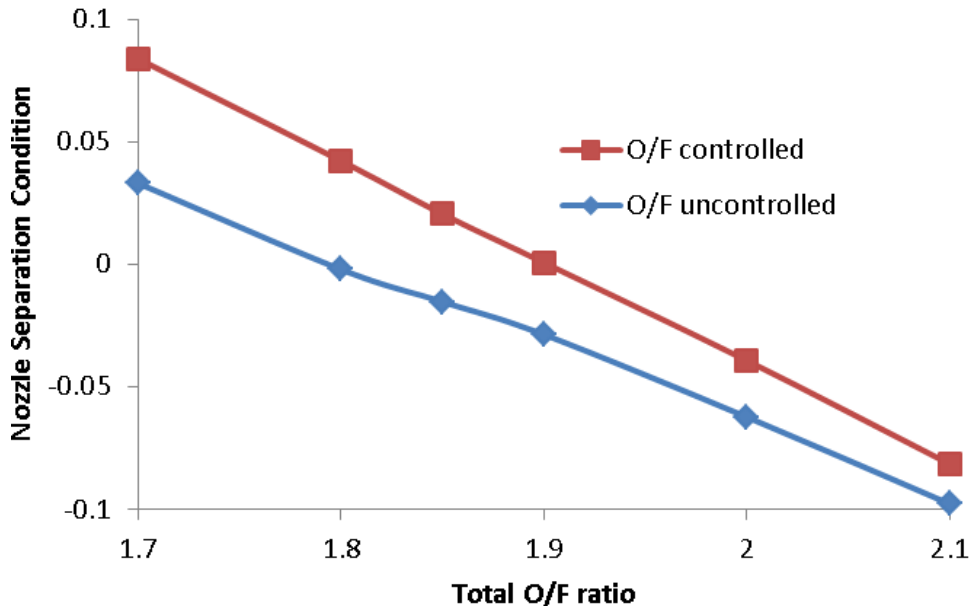


Figure 2.18. Comparison of the worst values of the nozzle flow separation condition Eq. (2.38) in the flight simulations of O/F controlled and O/F uncontrolled hybrid rockets under the nominal fuel regression behaviors.

2.7.2. Flight and Propulsion Performances in Systematic Errors

Figure 2.19 shows the highest altitude and the averaged specific impulse in the second set of the simulations. The O/F controlled cases maintained almost the best flight performances. We should note that the cases in positive systematic errors in regression rate behaviors resulted in the slightly higher altitudes than those in the nominal regression behavior by at most 0.25[km], but the specific impulse in the nominal case is the best one and the gap of the specific impulse from in the case of $+3\sigma$ error was just 0.2[s]. This reversal between the highest altitudes and the specific impulse is possibly because the total O/F ratio is not the optimal one to maximize the highest altitude with the accuracy less than 0.1 or the optimal instantaneous O/F ratio is dependent on chamber pressure or nozzle expansion ratio. On the other hand, in the O/F uncontrolled cases, the flight performances in the cases with the systematic errors did not maintain the best flight performance. The performance losses of the highest altitudes and the specific impulse are almost linear along with the size of the errors. The highest altitude in $+3\sigma$ regression error was 411.8[km] and lower than in the nominal regression behavior by 10.8%. The specific impulse in $+3\sigma$ regression error was 277.0[s], and the performance loss was by 2.9%. The altitude loss is relatively large compared to that of specific impulse. The reason for the gap between these two kinds of performance losses was easily estimated from the Figure 2.20.

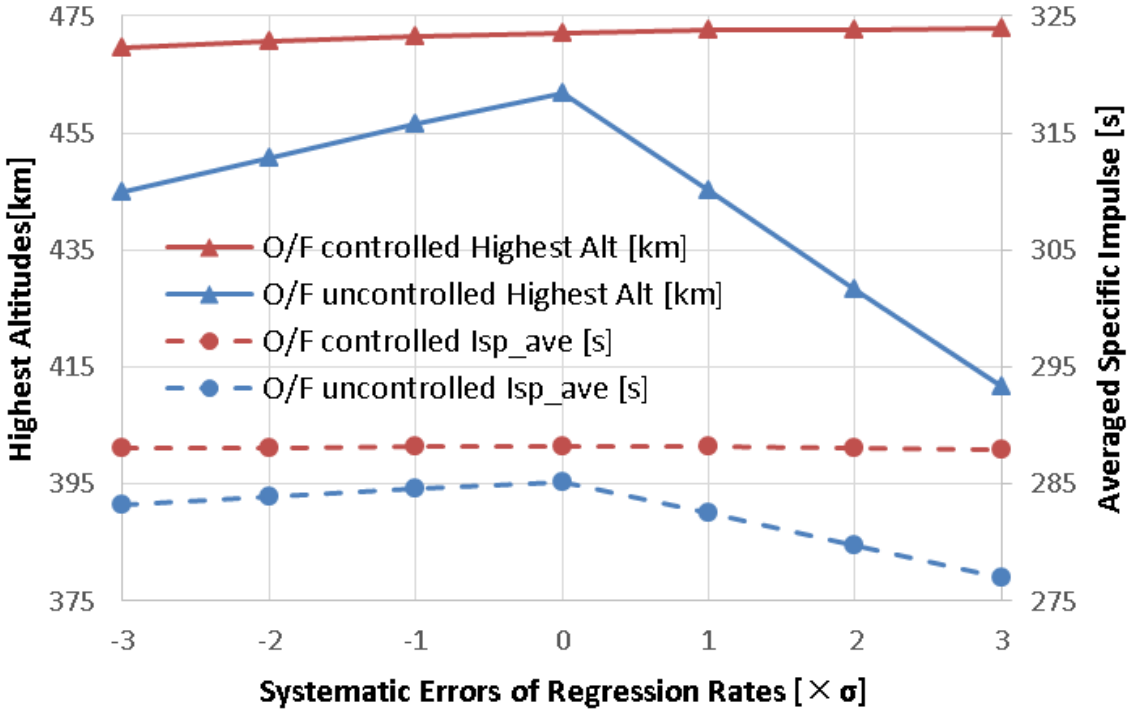


Figure 2.19. Comparison of highest altitudes and time averaged specific impulse between O/F controlled and O/F uncontrolled hybrid rockets under the existence of the systematic fuel regression errors.

Figure 2.20 shows the relation of total impulse and residual mass of the propellants with systematic errors of the fuel regression rates. The total impulse in the O/F controlled cases maintained the nominal one, and the residuals of the propellants were not yielded. On the other hand, in the O/F uncontrolled cases, the total impulse in the cases with fuel regression errors did not maintain the nominal ones. The loss of total impulse was also almost linear along with the size of the fuel regression errors, and 3.9% loss of the total impulse was observed in $+3\sigma$ regression error. The residual mass of the propellants in $+3\sigma$ regression error was 32.4[kg], and this amount of residual mass corresponds to the increase of final mass of the rocket by 5.4%. It is clear that the large amount of the residual compared to the losses of total impulse and specific impulse significantly affected the flight performances.

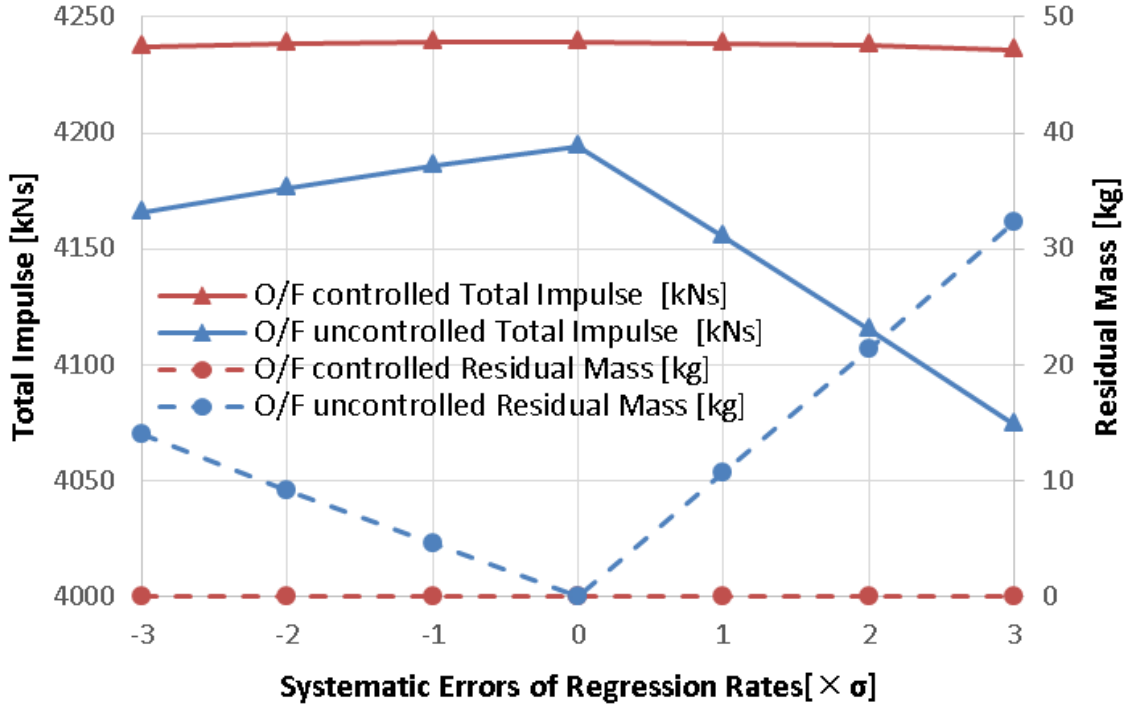


Figure 2.20. Comparison of the time averaged specific impulse and the residual mass of propellants between O/F controlled and O/F uncontrolled hybrid rockets under the existence of the systematic fuel regression errors.

The total performance loss of the highest altitudes in the O/F uncontrolled case can be roughly explained by the combined evaluation using the residual mass and the loss of specific impulse. When the aerodynamic drag, the duration of acceleration and the acquisition of altitudes during acceleration are neglected, the following simple dynamic energy conservation is applicable as

$$h \sim \frac{v^2}{2g} = \frac{1}{2g}\left(I_{sp} g \ln \frac{m_i}{m_f}\right)^2 \tag{2.52}$$

where velocity is evaluated with Tsiolkovsky rocket equation. The small changes of the final mass of rocket $m_f$ and specific impulse $I_{sp}$ are linked with the small change of the highest altitude $h$ using the following equations as

$$\Delta h \sim \frac{\partial h}{\partial m_f}\Delta m_f + \frac{\partial h}{\partial I_{sp}}\Delta I_{sp} \tag{2.53},$$

and the normalized expression by a referential performance is

$$\overline{\Delta h} \sim 2\left(\overline{\Delta I_{sp}} - \frac{\overline{\Delta m_f}}{\ln\frac{m_i}{m_f}}\right) \quad (2.54).$$

In the O/F uncontrolled case with $+3\sigma$ regression error, $\overline{\Delta I_{sp}} = -0.029$ and $\overline{\Delta m_f} = 0.054$ was substituted into Eq. (2.54), and $\overline{\Delta h}$ is approximately evaluated as $-0.144$. The practical altitude loss was 0.108. The gap of the simulation and the simple evaluation seems to be due to the ignored effects in the simple evaluation, but the simple evaluation resulted in the same order of magnitude. In this case, the second term in Eq. (2.54) was evaluated as -0.043 compared to the first term of -0.029. This analysis shows that there is a large impact of the residuals on the flight performances. Throughout this set of the simulations, the significance of the physical phenomena related to O/F shifts can be summarized in the following order: residual mass of propellants, total enthalpy at chemical equilibrium, and c* efficiency or nozzle throat erosion. The order of the former two effects can be reversed in some cases, but the effects of O/F shifts in the latter two phenomena are negligible.

### 2.7.3. Flight and Engine Performances in Random Errors

Figure 2.21-Figure 2.23 show the histograms of the distributions of the highest altitudes, specific impulse and residual mass of the propellants for 3000 times of the flight simulations including random errors in the fuel regression behaviors. In this set of the simulations, the prediction interval model Eq. (2.15) was adopted as the distribution of the random errors. The statistic peak of the highest altitudes in the O/F controlled cases was between 468.0 and 468.5 [km] compared to the range between 452.5 and 453.0 [km] in the O/F uncontrolled cases. In the former cases, the O/F shift elimination system succeeded to eliminate the variance of flight performances and residual mass. On the other hand, in the O/F uncontrolled cases, the variance of random errors directly yielded the residual masses of the propellants, and the wide distribution of penalty mass led to the wide range of the highest altitude. The peaks of specific impulse were respectively located nearly in the same range, between 287.2 and 287.3 [s] and between 284.0 and 284.1 [s]. Therefore, the performance gap of specific impulse is considered to be so small. However, there was a large gap in residual mass. In the O/F controlled cases, the residual mass was less than 0.08[kg] due to the O/F feedback control. On the other hand, in the uncontrolled cases, the peak of residual mass was 4.05[kg], and it affected their flight performances as the penalty mass. The maximum residual mass was 8.75[kg], and this amount corresponds to 1.46% of the final mass of the rocket.

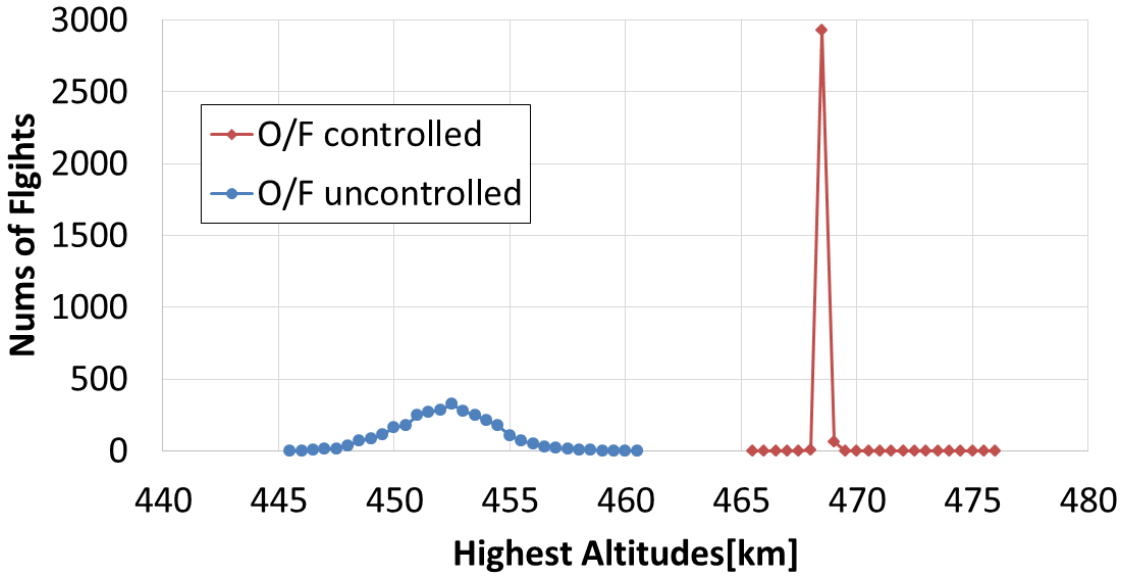


Figure 2.21. Histogram of highest altitudes of O/F controlled and O/F uncontrolled hybrid rockets under the existence of the random fuel regression errors.

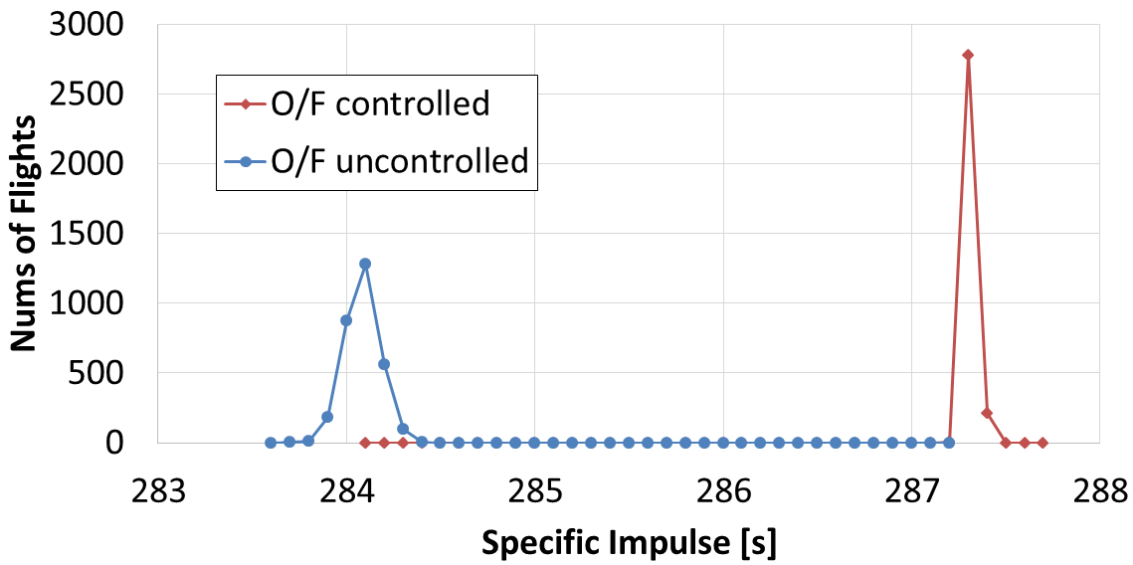


Figure 2.22. Histogram of time averaged specific impulse of O/F controlled and O/F uncontrolled hybrid rockets under the existence of the random fuel regression errors.

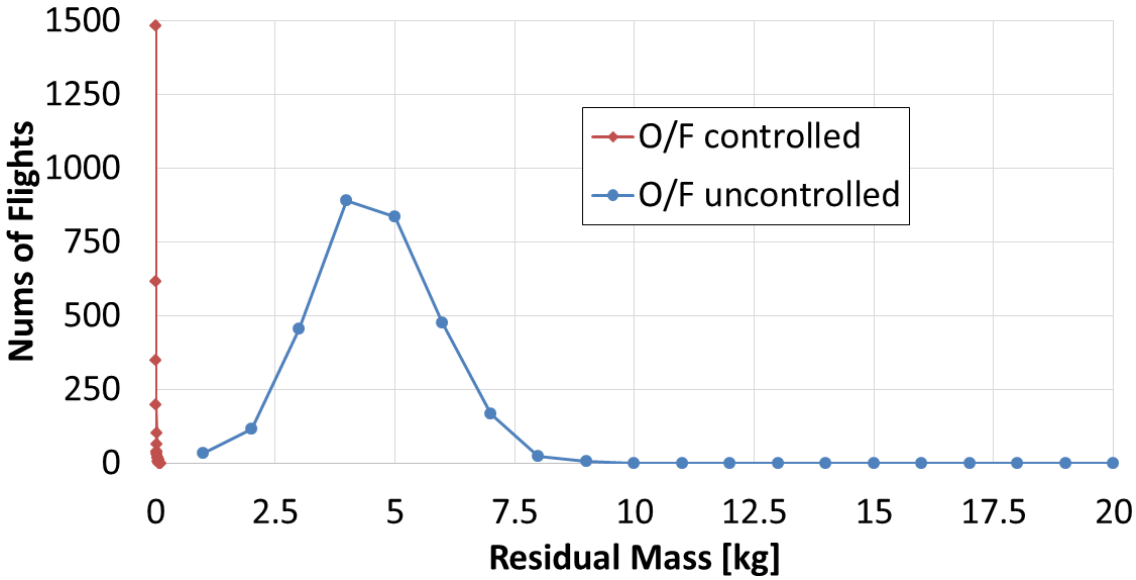


Figure 2.23. Histogram of residual mass of propellants of O/F controlled and O/F uncontrolled hybrid rockets under the existence of the random fuel regression errors.

The averaged value of the highest altitudes in the O/F uncontrolled cases was 452.0 [km] while that in the O/F controlled cases was 468.3 [km]. The shift of the peak of the highest altitudes is due to the loss of total impulse and penalty of the residual mass of the propellants. This is the same mechanism as in the previous subsection. The shares of these factors in the flight performance losses are roughly estimated from Eq. (2.54). In the current cases, the normalized gaps of the specific impulse and final mass in the worst performances in the O/F uncontrolled cases by the best performance in the O/F controlled cases can be evaluated as $\overline{\Delta I_{sp}} = -0.0157$ and $\overline{\Delta m_f} = 0.0146$, and the normalized loss of the highest altitude $\overline{\Delta h}$ is roughly evaluated as -5.47% from Eq. (2.54). This value is near to the practical gap of -5.80%. The weighting of the impacts of the loss of specific impulse and the increase of the final mass is 4:6.

In order to understand the results in more detail, the trace of the instantaneous O/F ratio and specific impulse should be observed. Figure 2.24 and Figure 2.25 respectively show their typical traces in the 3000 times flight simulations. They are compared with the nominal traces in the O/F uncontrolled cases. The random errors in O/F ratio equally distributed in both fuel and oxidizer rich sides over the duration of the engine operation. These errors tended to decrease the specific impulse in large throttle ratios because O/F ratios in high throttle ratios are near to the optimum ones, but the performance losses themselves are relatively small. On the other hand, in the deep throttle rates, the impacts of random O/F shifts in the O/F uncontrolled cases are relatively large. However, O/F shifts

toward the oxidizer rich side improved instantaneous specific impulse and compensated the large performance losses due to O/F shifts toward fuel rich side. Therefore, the overall loss of specific impulse in the random error cases are moderate compared to in the systematic errors cases.

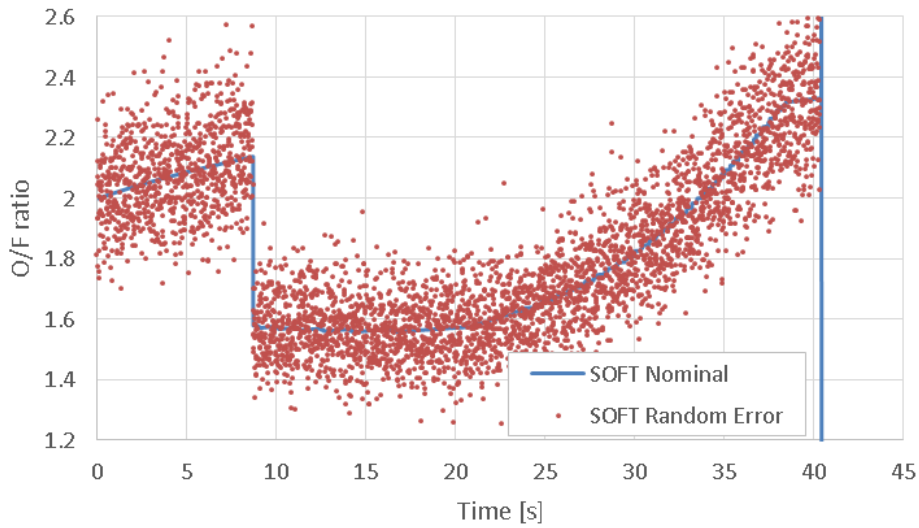


Figure 2.24. Comparison of instantaneous O/F ratio of O/F uncontrolled hybrid rockets between the nominal fuel regression behavior and the one with the random errors.

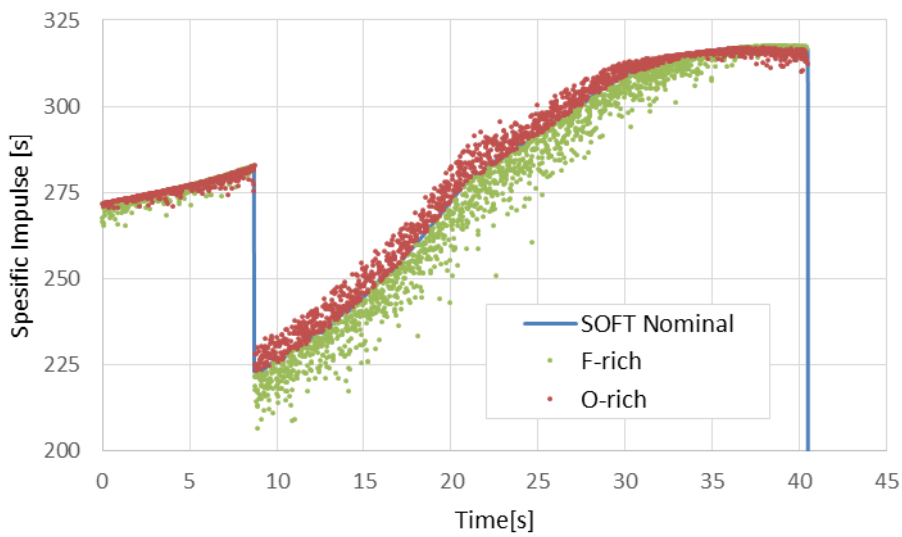


Figure 2.25. Comparison of instantaneous specific impulse of O/F uncontrolled hybrid rockets between the nominal fuel regression behavior and the one with the random errors.

## 2.8. Conclusions

In this chapter, in order to evaluate the effects of O/F shifts in hybrid rocket propulsion on the flight performances, the vertically launched single stage sounding rockets were simulated. The flight performances were compared between the O/F controlled and uncontrolled cases. In our flight simulations, the scale of the rockets was the fixed one similar to that of S-520 rockets. After giving the reasonable design parameters, the geometries of the fuel grain and the liquid oxygen tank were calculated on each total O/F ratio. The given parameters were gross, structural and payload masses, density of paraffin wax and liquid oxygen, solid fuel regression rate behavior, initial port to throat diameter ratio, and the maximum oxidizer mass flux. The design point was chosen from the relations among the undetermined design variables of fuel grain diameters, aspect ratio, initial acceleration and geometric swirl number at the lift off. These design variables were selected while referring to those of the practical sounding rockets.

The hybrid rocket engine model simulates the three physical phenomena to be affected by O/F shifts and to affect propulsion performances in addition to other necessary models to calculate thrust. They are the thermodynamic state of the gaseous products, c* efficiency and throat erosion. These models consist of the combinations of the previous researches and had been validated. The engine operation includes thrust control based on the Tsien's Goddard problem solution to increase the flight performances and give O/F shifts due to throttling. The fuel regression behavior was modeled from the results of the previous burn tests of axial hybrids using paraffin wax and oxygen and the SOFTs using PMMA and GOX. This model includes the confidential interval used for the systematic error model of the fuel regression rates and the prediction interval used for the random error model.

The three sets of the flight simulations were carried out in our study, and they had the individual purposes. The first set simulated the flight performances in the nominal fuel regression behavior to evaluate the impacts of the three physical phenomena affected by O/F shifts and to determine the total O/F ratio to maximize the highest altitudes. The purpose of the second set was to evaluate the effects of O/F shifts caused by the systematic errors in the fuel regression behavior. The total O/F ratio was fixed to the optimal one of 1.9. The size of the systematic errors was varied between $-3\sigma$ and $+3\sigma$ of the confidential interval. The purpose of the last set was to evaluate the effects of O/F shifts caused by the random errors in the fuel regression behavior. The error model was based on the prediction interval. The flight simulations were repeated for 3000 times.

In the first set, the cases of total O/F=1.9 resulted in the best flight performances in both of the O/F controlled and uncontrolled cases. Their performance gaps of the highest altitudes and specific impulse were respectively 2.2% and 1.1%. These gaps were due to the decrease of the enthalpy shift in the deep throttling operation. The other phenomena related to O/F shifts hardly affected the flight performances. In the second set, the O/F uncontrolled hybrids linearly decreased the flight performances along with the systematic errors of the fuel regression behavior whereas the O/F controlled hybrids maintained the best flight performances. The O/F uncontrolled case lost 10.8% of the highest altitude in the $+3\sigma$ error case. The expected and worst values of the highest altitude in the O/F uncontrolled cases were respectively 445[km] and 412[km] with 99.73% probability whereas those in the O/F controlled cases were 472[km] with the same probability. One of the main reasons for the performance loss was the penalty of the final mass up to 32.4[kg] due to the residual mass of the propellants. This penalty corresponds to the 5.4% increase of final mass and the loss of 2.2% of the propellants. The other major reason was the loss of averaged specific impulse by 2.9%. From these results, the second set of the flight simulations revealed that O/F shifts due to the systematic errors of the regression rates yield residual mass of the propellants in addition to losses of propulsion performances, and the conceptual O/F shift elimination technology perfectly prevented the performance losses. In the last set of the flight simulations, the flight performances in the both O/F controlled and uncontrolled systems decreased to some degree from their best performances in the nominal regression behavior. In the O/F controlled cases, the highest altitudes were located in the narrow range between 468.0 and 468.5 [km] compared to the range between 452.5 and 453.0 [km] in the O/F uncontrolled cases. The conceptual O/F shift elimination technology succeeded to eliminate most of the residual propellants and the performance losses from the nominal ones, but the O/F uncontrolled cases less decreased their performances than in the systematic errors. This seems to be because the improvement of specific impulse due to the positive O/F shifts compensated the lower specific impulse due to the negative ones. The residual mass in the O/F uncontrolled cases was yielded along with the variance of the random errors and decreased the averaged value of the highest altitudes further than those in the O/F controlled cases. Thee flight performances in the O/F uncontrolled cases widely distributed compared to those in the O/F controlled cases because the variance of random errors in the fuel regression behavior directly affected their flight performances. The expected highest altitude of the O/F uncontrolled hybrid rocket was 452.0[km] and higher than 445.0[km] with 99.73% probability while the O/F controlled hybrid rocket reaches 468.0[km] with the same probability. In other words, the guaranteed performance in the O/F controlled cases is 5.2% higher than that in the O/F uncontrolled cases. Therefore, this set of the flight

simulations revealed that random errors of the fuel regression behavior also yield residual mass of the propellants and affect flight performances and the O/F shift elimination technologies nearly perfectly prevent the performance losses.

Finally, this chapter clarified that O/F shift elimination technologies in hybrid rocket propulsion improve flight performances in vertically launched hybrid sounding rockets with the scale of S-520 rockets at most by 10 % and highly functional hybrid rockets capable of both thrust and O/F control are meaningful for sounding rockets.

Bibliography of Chapter 2


1 Matsuno, H., Kohno, M., Onoda, J., Kawashima, T., Murakami, T., and Onojima, N., "Development of the S-520 Single Stage Sounding Rocket," *Acta Astronautica*, vol. 9, 1982, pp. 631–635.

2 Shinohara, K., and Nakagawa, I., "Regression Rate Characteristics of Paraffin-based Fuel under Swirled Oxidizer Flow," *48th AIAA/ASME/SAE/ASEE Joint Propulsion Conference & Exhibit*, Atlanta, GA: AIAA, 2012, p. AIAA 2012-4104.

3 Daisuke, S., Saburo, Y., Kousuke, H., Takashi, S., and Noriko, S., "Combustion Characteristics of Paraffin-Fueled Swirling Oxidizer-Flow-Type Hybrid Rocket Engines," *48th AIAA/ASME/SAE/ASEE Joint Propulsion Conference & Exhibit*, Atlanta, GA: AIAA, 2012, p. AIAA 2012-3904.

4 Tamura, T., Saburo, Y., and Kengo, Y., "Effects of Swirling Oxidizer Flow on Fuel Regression Rate of Hybrid Rockets," *35th AIAA/ASME/SAE/ASEE Joint Propulsion Conference and Exhibit*, Los Angeles, California: AIAA, 1999, p. AIAA 99-2323.

5 Yuasa Saburo, Yamamoto Kengo, Hachiya Hitoshi, Kitagawa Koki, O. Y., "Development of a Small Sounding Hybrid Rocket with a Swirling-Oxidizer-Type Engine," *37th AIAA / ASME / SAE / ASEE Joint Propulsion Conference & Exhibit*, Salt Lake City, UT: AIAA, 2001, p. AIAA 2001-3537.

6 Marxman, G. A., Wooldridge, C. E., and Muzzy, R. J., "Fundamentals of Hybrid Boundary Layer Combustion," *Heterogeneous Combustion Conference*, Palm Beach,FL: AIAA, 1963, p. AIAA 63-505.

7 Karabeyoglu, A., Zilliac, G., Cantwell, B. J., DeZilwa, S., and Castellucci, P., "Scale-Up Tests of High Regression Rate Paraffin-Based Hybrid Rocket Fuels," *Journal of Propulsion and Power*, vol. 20, 2004, pp. 1037–1045.

8 Ross, S. M., *Introduction to Probability and Statistics for Engineers and Scientists*, Elsevier, 2009.

[9] Box, G. E. P., and Muller, M. E., "A Note on the Generation of Random Normal Deviates," *The Annals of Mathematical Statistics*, vol. 29, 1958, pp. 610–611.

[10] Gordon, S., and McBride, B. J., *Computer Program for Calculation of Complex Chemical Equilibrium Compositions and Applications*, 1994.

[11] Huzel, D. K., and Huang, D. H., *Modern Engineering for Desing of Liquid-Propellant Rocket Engines*, AIAA, 1992.

[12] Karabeyoglu, A., Zilwa, S. De, Cantwell, B., and Zilliac, G., "Modeling of Hybrid Rocket Low Frequency Instabilities," *Journal of Propulsion and Power*, vol. 21, 2005, pp. 1107–1116.

[13] Ishiguro, T., Sinohara, K., Sakio, K., and Nakagawa, I., "A Study on Combustion Efficiency of Paraffin-based Hybrid Rockets," *47th AIAA/ASME/SAE/ASEE Joint Propulsion Conference & Exhibit*, San Diego, CA: AIAA, 2011, p. AIAA 2011-5679.

[14] Jones, M. D., Abel, T. M., and Weeks, D. J., "Subscale Hybrod Rocket Motor Testing at the Marshall Space Flight Center in Support of the Hybrid Propulsion Demonstration Program (HPDP)," *33rd AIAA/ASME/SAE/ASEE Joint Propulsion Conference & Exhibit*, Seattle, WA: AIAA, 1997, p. AIAA 97-2800.

[15] Boardman, T. A., Carpenter, R., Goldberg, B., and Shaeffer, C. W., "Development and Testing of 11- and 24-Inch Hybrid Motors Under the Joint Governmental Industry IR & D Program," *29th AIAA/SAE/ASME/ASEE Joint Propulsion Conference and Exhibit*, AIAA, 1993, p. AlAA 93-2552.

[16] Delaney, L. J., and J, W. H. J., "Erosion of Graphite Nozzle Inserts," *AIAA Journal*, vol. 2, 1964, pp. 1428–1433.

[17] Bianchi, D., and Nasuti, F., "Numerical Analysis of Nozzle Material Thermochemical Erosion in Hybrid Rocket Engines," *Journal of Propulsion and Power*, vol. 29, 2013, pp. 547–558.

[18] Bartlett, E. P., Kendall, R. M., and Rindal, R. A., *An Analysis of the Coupled Chemically Reacting Boundary Layer and Charring Ablator. Part IV: A Unified Approximation for Mixture Transport Properties for Multicomponent Boundary-Layer Applications*, 1968.

[19] Svehla, R. a., "Estimated Viscosities and Thermal Conductivities of Gases at High Temperatures," *NASA Lewis Research Center Technical Report*, vol. No. R-132, 1962.

[20] Ratcliff, G. A., *Unit Operations of Chemical Engineering*, McGraw-Hill Education, 1957.

[21] Chelliah, H. K., Makino, A., Kato, I., Araki, N., and Law, C. K., "Modeling of Graphite Oxidation in a Stagnation-Point Flow Field Using Detailed Homogeneous and Semiglobal Heterogeneous Mechanisms with Comparisons to Experiments,"

*Combustion and Flame*, vol. 104, 1996, pp. 469–480.

[22] Sutton, G., and Biblarz, O., *Rocket Propulsion Elements*, John Wiley & Sons, Inc, 2001.

[23] Stark, R. H., "Flow Separation in Rocket Nozzles, a Simple Criteria," *41st AIAA/ASME/SAE/ASEE Joint Propulsion Conference & Exhibit*, Tucson, AR: AIAA, 2005, p. AIAA 2005-3940.

[24] Goddard, R. H., "A Method of Reaching Extmeme Altitudes," *Smithsonian Miscellaneous Collections*, vol. 71, 1919, pp. 1–79.

[25] Ben-Asher, J. Z., "Application to Rocket Performance: The Goddard Problem," *Optimal Control Theory with Aerospace Applications*, AIAA, 2010, pp. 217–229.

[26] Suli, E., Suli, E., Mayers, D., and Mayers, D., *An Introduction to Numerical Analysis*, Cambridge University Press, 2003.

[27] Chiaverini, M. J., Kuo, K. K., *Fundamentals of Hybrid Rocket Combustion and Propulsion*, AIAA, 2007.

[28] Lengelle, G., Fourest, B., Godon, J., and Guin, C., "Condensed-Phase Behavior and Ablation Rate of Fuels for Hybrid Propulsion," *29th Joint Propulsion Conference and Exhibit*, Monterey, CA: AIAA, 1993, p. AIAA 93-2413.

[29] Akiba, R., "Vertical Flight Performance of Rockets and Thrust Planning," *Bimonthly journal of Institute of Industrial Science, University of Tokyo*, vol. 8, 1956, pp. 256–259.

[30] *Standard Atmosphere ISO 2533-1975*, 1975.

# Chapter 3

# Comparison of Advantages and Disadvantages of O/F Shift Elimination Technologies

The prior chapter revealed that O/F shifts have not small impacts on the flight performances of sounding hybrid rockets. Though several O/F shift elimination technologies had already been proposed, their characteristics in practical use had not been discussed. In this chapter, the advantages and disadvantages among the several ideas to eliminate O/F shifts are compared, and the most promising candidate for practical use is selected. The two of them are those previously proposed, Aft-end Oxidizer Injection method and pressure sensitive fuels (PSF). In this chapter, throttle ranges at a constant O/F ratio are quantitatively compared. Other qualitative advantages and disadvantages are also compared from the aspects of structural coefficient, combustion stability, and complexity of the systems.

## 3.1. Altering-intensity Swirling Oxidizer Flow Type Hybrid Rocket Engines

In this section, Altering-intensity Swirling Oxidizer Flow Type (A-SOFT) Hybrid Rocket Engines are newly proposed as an O/F shift elimination technology. The concept of this type of engines is to control both thrust and O/F ratio by changing geometric swirl number of Swirling Oxidizer Flow Type (SOFT) hybrid rocket engines.

SOFT is a technique to increase fuel regression rates by adding circumferential velocity component in oxidizer main flows, and regression rates of SOFTs depend also on swirl strength as mentioned in the previous chapter. The indicator of swirl strength created by the injectors is expressed by geometric swirl number as

$$S_g = \frac{R_m \rho u_{inj}^2 A_{inj}}{R \rho u_{z_e}^2 A_{port}} = \frac{R_m A_{port}}{R A_{inj}}$$

(3.1).

This is the same equation as Eq. (2.1). In SOFTs, geometric swirl number is a constant

dependent on geometries of tangential injectors.

The concept of A-SOFT is to vary $S_g$ as an operating variable to control regression rates and finally both O/F ratio and thrust in combination with oxidizer mass flow rate because oxidizer mass flow rate is an independent operating variable of $S_g$. This concept seems to be realized by the dual injection of axial and tangential injections of oxidizer flows as is shown in Figure 3.1. A-SOFT has the two kinds of injectors. One is an axial injector and the other is a tangential injector. The oxidizer mass flow rates from the two injectors are controlled independently of each other by the individual control valves, and the "effective" geometric swirl number should be determined dominantly by the geometry of the tangential injector and the mass flow ratio of the oxidizer from the two injectors. In order to evaluate swirl strength after merge of the two flows, effective geometric swirl number $S_e$ is newly defined. Under the assumption of axial injection of oxidizer flow in addition to tangential injection, as is in the definition of geometric swirl number $S_g$, the ideal angular momentum normalized by injector outlet radius and the ideal momentum can be evaluated as

$$S_e \equiv \frac{M}{RI} = \frac{\frac{R_m}{2}\frac{\dot{m}_{o_{tan}}^2}{\rho A_{inj}}}{R\frac{(\dot{m}_{o_{ax}}+\dot{m}_{o_{tan}})^2}{\rho A_{port}}} = \frac{R_m A_{port}}{R A_{inj}}\frac{1}{(1+\dot{m}_{o_{ax}}/\dot{m}_{o_{tan}})^2} = \frac{S_g}{(1+\dot{m}_{o_{ax}}/\dot{m}_{o_{tan}})^2}$$

(3.2)

where $M$ and $I$ respectively refer to the ideal angular momentum and the ideal momentum, and $\dot{m}_{o_{ax}}$ and $\dot{m}_{o_{tan}}$ respectively refer to oxidizer mass flow rates from axial and tangential injectors. The other variables have the same determinations as in Eq. (2.1). This evaluation suggests that effective geometric swirl number $S_e$ which affects fuel regression rates in A-SOFTs should be controlled dominantly by axial to tangential oxidizer mass flow ratio. This parameter is independent of total oxidizer mass flow rate $\dot{m}_o = \dot{m}_{o_{ax}} + \dot{m}_{o_{tan}}$. That is why fuel regression rate, thrust and O/F ratio of A-SOFTs should be controlled by $\dot{m}_o = \dot{m}_{o_{ax}} + \dot{m}_{o_{tan}}$ and $\dot{m}_{o_{ax}}/\dot{m}_{o_{tan}}$.

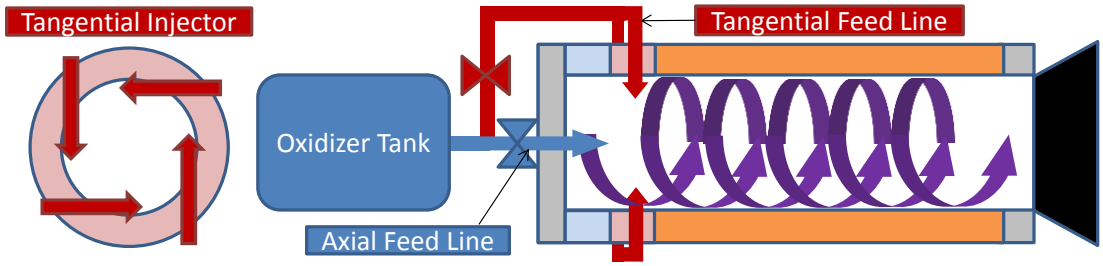


Figure 3.1. Schematics of the concept of Altering-intensity Swirling Oxidizer Flow Type Hybrid Rocket Engines

## 3.2. Evaluations of Throttle Ranges

In this section, throttle range of the individual candidates of the O/F elimination technologies are quantitatively evaluated. About Aft-end Oxidizer Injection method and Altering-intensity Swirling Oxidizer Flow Type (A-SOFT), possible throttle ranges are evaluated just under the minimal restrictions of these methods. On the PSF method, necessary conditions to eliminate O/F shifts will be discussed.

### 3.2.1. Aft-end Oxidizer Injection Method

As in A-SOFTs, also in the Aft-end Oxidizer Injection method, the oxidizer flow splits into the two branches as is shown in Figure 3.2. The one flow is injected from the head-end of the fuel port and contributes to the fuel regression, and the other flow is injected into the aft-combustion chamber to adjust O/F ratio. Therefore, the following inequality on oxidizer mass flow rates stands as

$$\dot{m}_o = \dot{m}_{o_1} + \dot{m}_{o_2}, 0 \leq \dot{m}_{o_1}, \dot{m}_{o_2} \leq \dot{m}_o \tag{3.3}$$

where the subscripts 1 and 2 respectively refer to the head-end injection and the aft-end injection. Because $\dot{m}_{o_1}$ only contributes to the fuel regression, the fuel mass flow rate is

$$\dot{m}_f = 2\pi^{1-n} a L r^{1-2n} \rho_{sf} \left(\dot{m}_o - \dot{m}_{o_2}\right)^n = A\left(\dot{m}_o - \dot{m}_{o_2}\right)^n \tag{3.4}$$

This equation means that the start point of the relation between the fuel and oxidizer mass flow rates shifts by $\dot{m}_{o_2}$. The condition to keep O/F ratio $1/k$ is

$$A\left(\dot{m}_o - \dot{m}_{o_2}\right)^n \leq \dot{m}_f = k\dot{m}_o \leq A\dot{m}_o{}^n$$

(3.5).

Figure 3.3 shows the geometric expression of Eq. (3.5). The blue colored zone is the throttlable region. The black line refers to the constant O/F ratio $1/k$. The lower limit condition $\dot{m}_f = A\left(\dot{m}_o - \dot{m}_{o_2}\right)^n$ in Eq. (3.5) can shift toward positive direction of the $x$ axis because any $\dot{m}_{o_2} \geq 0$ can be taken, and finally the operational area of this method can be shown in the right figure in Figure 3.3. From Eq. (3.5), the throttle range should be

$$0 \leq k\dot{m}_o \leq A\dot{m}_o{}^n$$

(3.6).

Therefore, the throttling range at a constant O/F ratio is

$$0 \leq \dot{m}_o \leq \left(\frac{A}{k}\right)^{\frac{1}{1-n}}$$

(3.7)

Conceptually, in the Aft-end Oxidizer Injection method, an upper thrust limit at a constant O/F ratio always exists, but we can confirm whether the referential (100%) oxidizer mass flow rate $\dot{m}_{o_{max}}$ agrees with $\dot{m}_{o_{max}} \leq \left(\frac{A}{k}\right)^{\frac{1}{1-n}}$ in the design phase of the engine. If the parameter $A$ proportional to $Lr$ is designed to fulfill the condition of Eq. (3.7), the lower limit of the thrust is negligible in practical operations.

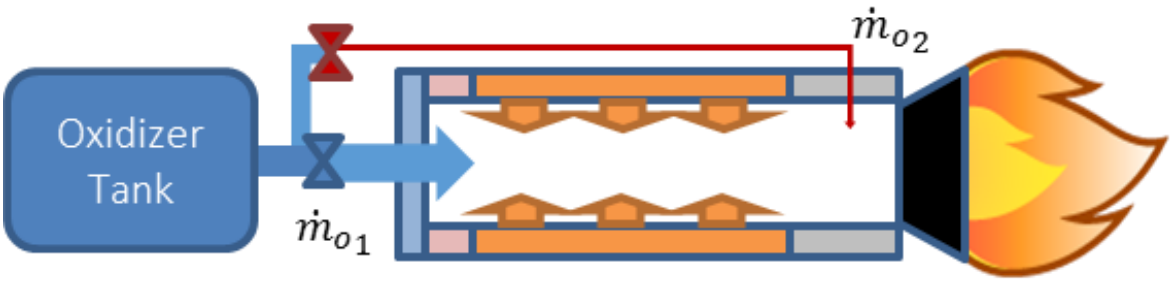

Figure 3.2. A schematic of the concept of Aft-end Oxidizer Injection Method and the definitions of the variables.

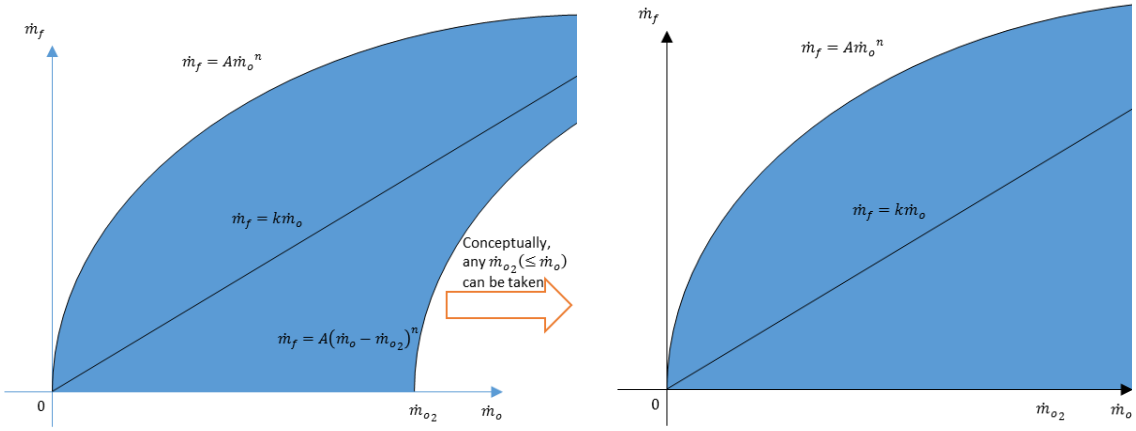


Figure 3.3. Geometric expression of the throttle range of Aft-end Oxidizer Injection Method using $\dot{m}_{o_2}$ with an upper limit (left) and $\dot{m}_{o_2}$ without its upper limit (right).

3.2.2. Pressure Sensitive Fuels

The fuel regression rates of PSFs are conceptually expressed in the following equation as

$$\dot{r} = ap^m G_o^n$$

(3.8)

where $p$ refers to chamber pressure. Chamber pressure is approximately proportional to the total mass flow rate as

$$p = l\dot{m}_o\left(1 + \frac{1}{O/F}\right)$$

(3.9)

where $l$ is a constant. The O/F ratio is evaluated using Eqs. (3.8) and (3.9) as

$$\frac{O}{F} = \frac{r^{2n-1}\dot{m}_o^{1-n}p^{-m}}{2\pi^{1-n}L\rho_{sf}a} = \frac{r^{2n-1}\dot{m}_o^{1-n-m}}{2\pi^{1-n}L\rho_{sf}al^m}\left(1 + \frac{1}{O/F}\right)^{-m}$$

(3.10).

In order to maintain O/F ratio, the right hand of this equation is kept constant through the engine operation. This condition corresponds to

$$r^{1-2n}\dot{m}_o^{m+n-1} = const.$$
(3.10).

In order to fulfill this condition, the chamber pressure and oxidizer mass flux exponents should be

$$n = m = \frac{1}{2}$$
(3.11).

Practically, it is greatly difficult to develop solid fuels having this characteristic in all the ranges of pressure, oxidize mass flux and scales of the fuel grain. Even if such solid fuels are developed, huge development costs should be taken into account because a number of full scale tests should be required to eliminate scale effects.

3.2.3. Altering-intensity Swirling Oxidizer Flow Type

In A-SOFTs, the fuel mass flow rates should be expressed as

$$\dot{m}_f = 2\pi L r \rho_{sf} a(1 + S_e^2)^m G_o^n = A(1 + S_e^2)^m \dot{m}_o^n$$
(3.12).

Therefore, the condition to maintain O/F ratio $1/k$ is

$$A\dot{m}_o^n \leq \dot{m}_f = k\dot{m}_o \leq A\left(1 + S_{e_{max}}^2\right)^m \dot{m}_o^n$$
(3.13).

The left figure of Figure 3.4 shows the geometric expression of Eq. (3.13). The blue colored area is the possible operational range. The black straight line refers to a constant O/F ratio $1/k$. The upper limit of fuel mass flow rates is $\dot{m}_f = A\left(1 + S_{e_{max}}^2\right)^m \dot{m}_o^n$, and this limit can expand toward the y axis because conceptually any $S_e \geq 0$ can be taken. If the tangential injector is ideally designed to realize any geometric swirl number, finally the left

figure in Figure 3.5 shifts to the right one. The blue operational area of A-SOFT in the right figure of Figure 3.5 corresponds to the outside of those of the Aft-end Oxidizer Injection method. The throttle range in the right figure is expressed by the following equation as

$$A\dot{m}_o^n \leq k\dot{m}_o$$

(3.14).

Therefore, the throttle range is

$$\dot{m}_{o_{min}} \geq \left(\frac{A}{k}\right)^{\frac{1}{1-n}}$$

(3.15).

Conceptually, in A-SOFTs, a lower thrust limit at a constant O/F ratio always exists, but we can confirm whether the lowest throttle ratio to be used oxidizer mass flow rate $\dot{m}_{o_{min}}$ fulfills the condition of Eq. (3.15) in the design phase of the engine. If the parameter $A$ proportional to $Lr$ is designed to fulfill the condition of Eq. (3.15), the lower limit of the thrust is negligible in practical operations.

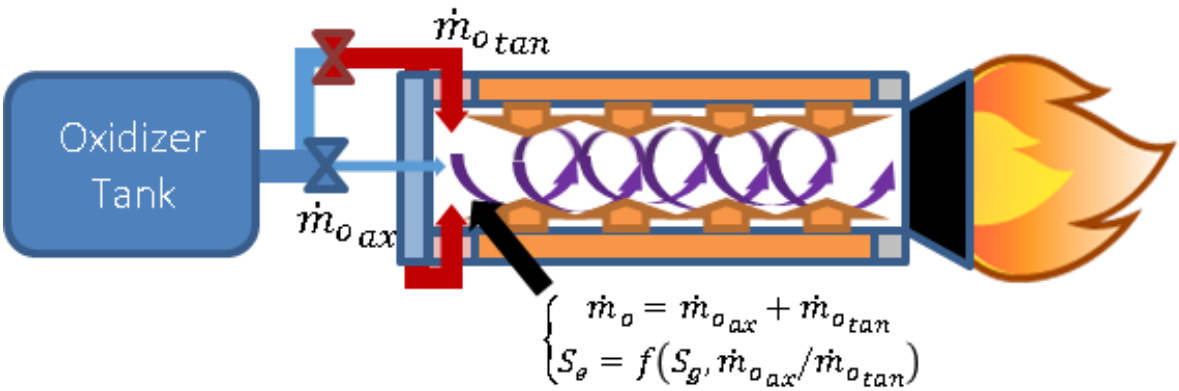


Figure 3.4. Schematics of the concept of A-SOFTs and the definitions of the variables.

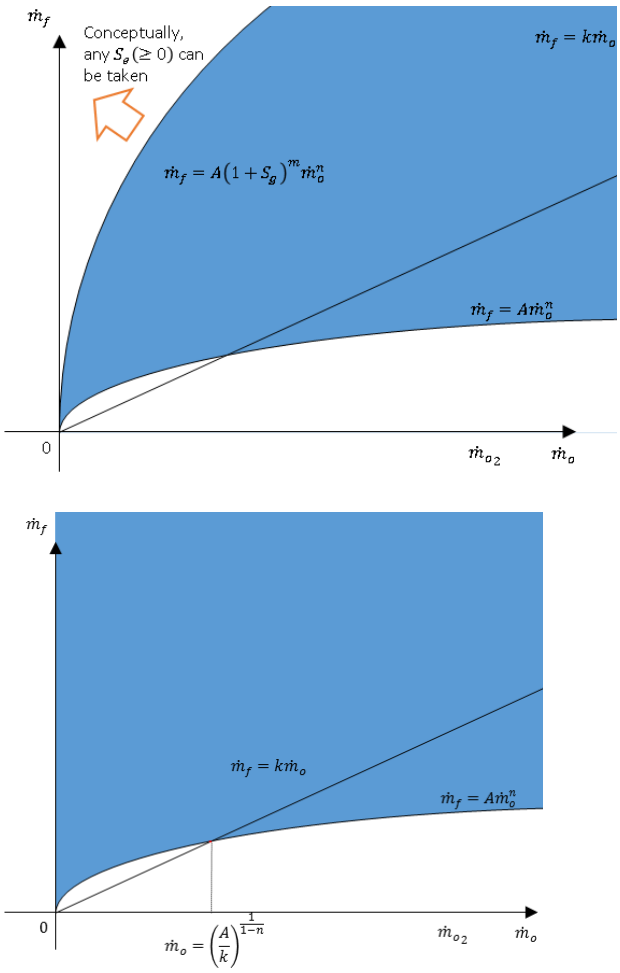


Figure 3.5. Geometric expression of the throttle range of A-SOFTs using $S_e$ with an upper limit and $S_e$ without its upper limit.

## 3.3. Comparison of the Qualitative Advantages and disadvantages in O/F Shift Elimination Technologies

In this subsection, the characteristics of the O/F shift elimination technologies are pointed out, and their qualitative advantages and disadvantages are discussed. At the last of this section, the most favorable method is selected from the aspects of the flight performances and practical usage.

First, the necessity of the oxidizer injection in gaseous state is discussed. In A-SOFTs, vaporization of liquid oxidizer is necessary before injecting oxidizer into combustion chamber whereas the other methods do not have such requirements. This is

because liquid oxidizer decreases the enhancement of regression rates due to swirling injection of oxidizer[1]. This also means that liquid oxidizer injection weakens the sensitivity of fuel regression rates to geometric swirl number to be used for the control of O/F ratio. Moreover, combustion instability was reported in liquid oxidizer injection whereas SOFTs using gaseous oxidizer injection quite stably burned[2]. This is possibly because a time lag of liquid oxidizer vaporization inside the chamber induces a pressure oscillation coupled with the natural frequency of chugging of the propulsion system[2]. Therefore, any types of liquid oxidizer vaporization system should be implemented such as pre-burners[3] or regenerative cooling nozzle for oxidizer vaporization[4]. Oxidizer vaporization systems make the propulsion system more complex and the structural mass of the oxidizer feed system increases. However, the oxidizer vaporization systems give a benefit also to other O/F control systems. That is the uniformity of local oxidizer mass flux especially in low throttle ratios. The paper[5] reported that ununiformed fuel regression or combustion instability was sometimes observed due to the ununiformed spray of liquid oxidizer in the deep throttle operations. Therefore, from the aspect of combustion stability, oxidizer vaporization systems are recommended also in the other two methods if deep throttle operations are to be used.

From the aspect of c* efficiency, A-SOFTs have an advantage compared to the other two methods because high c* efficiency for hybrid rocket propulsion were reported in SOFTs[6]. This good performances in SOFTs are mainly because the addition of circumferential velocity component enhanced diffusion and mixing of fuel and oxidizer inside the turbulent boundary layer. In the Aft-end Oxidizer Injection method, the mixing effects should decrease in the fuel port because of lower mass flow rates from the head-end of the fuel port. Instead, aft-oxidizer injections into productive gases from the main chamber can improve mixing effects, though parametric studies are possibly important to determine the locations of the aft-injectors. The characteristics of PSFs on c* efficiency should strongly depend on the chemical species of the propellants, and cannot be discussed in the current conceptual phase.

A-SOFTs have the same or larger regression rates compared to those in axial hybrids because swirling oxidizer injection is originally a technique to enhance regression rates[7]. Moreover, A-SOFTs enable us to place more importance on mechanical properties of solid fuels than on their regression rates. This expansion of acceptable ranges of regression rates is important because regression rates and mechanical strength practically have a

trade-off relation especially in high regression rate fuels such as paraffin wax based fuels. This high baseline of fuel regression rates provides a larger design space of solid fuel grains and aspect ratio of rockets. On the other hand, the Aft-end Oxidizer Injection method has the same or lower fuel regression rates compared to the axial hybrids because a part of the total oxidizer mass flow contributes to fuel regression and combustion flow at the tail end of the fuel port should be in fuel rich conditions. Therefore, this propulsion system should have large aspect ratio and thin fuel web thickness in order to broaden surface area for the solid fuel gasification. The baseline regression rates of PSFs should depend on the chemical compositions of the propellants. If the base material of PSFs is a conventional hydrocarbon in hybrids, the regression rates should be in the same or higher range.

A-SOFTs and PSFs have more complex fuel regression behaviors than the Aft-end Oxidizer Injection method because they have the two operation variables to affect fuel regression rates, and their characteristics of regression rates should be studied along with the two dimensional space of operating variables. This means that the number of operating points to be tested for engine developments should be square of that in conventional hybrids. This increase of the tests should lead to large increase of development costs.

As discussed in the previous section, throttle range of A-SOFT and Aft-end Oxidizer Injection method practically do not have limitation of their throttle ranges under the appropriate designs of the solid fuel grains. On the other hand, it is so difficult to develop PSFs compatible over wide throttle ranges and scales of flows.

The advantages and disadvantages of the O/F shift elimination technologies based on the above discussion are summarized in Table 3.1. It is clear that A-SOFT is the best option in the three candidates though the complexity of the fuel regression mechanism is a problem. Therefore, we selected the A-SOFT as the most promising candidate of the O/F control systems in hybrid rocket propulsion.

Table 3.1. Summary of the qualitative advantages and disadvantages among the three O/F shift elimination technologies.

| Trade off | A-SOFT | Aft-end Injection | PSF |
|---|---|---|---|
| Liquid oxidizer vaporization | Necessary | Unnecessary | Unnecessary |
| Uniform spray of oxidizer | ○ | △ | △ |

| | | | |
|---|---|---|---|
| Combustion stability | ○ | △ | △ |
| C* efficiency | ○ | △ | ? |
| Baseline reg-rates | ○ | × | △ |
| Aspect ratio/Structural coefficient | ○ | × | △ |
| Simplicity of regression characteristics | △ | ○ | △ |
| Throttle range | ○ | ○ | × |

## 3.4. Conclusions

In this chapter, the concept of A-SOFT is explained, and throttle range and other qualitative advantages and disadvantages were compared with the existing O/F shift elimination technologies proposed before. This chapter clarified that A-SOFTs conceptually do not have restrictions on throttle ranges under the appropriate designs of the solid fuel grains and qualitatively have favorable characteristics from the most points of views. The only practical disadvantage is that the costs of burn tests for R&Ds become larger than the other candidates because a lot of tests should be done in the two dimensional operating space. However, this disadvantage will be compensated by the analytical or numerical researches, and this thesis focuses on A-SOFTs in the following chapters.

## Bibliography of Chapter 3


1 Yuasa, S., Shimada, O., Imamura, T., Tamura, T., and Yamamoto, K., "A Technique for Improving of Hybrid Rocket Engines the Performance," *35th AIAA/ASME/SAEASEE Joint Propulsion Conferenceand Exhibit*, Los Angeles, CA: AIAA, 1999, p. AIAA 99-2322.

2 Kitagawa, K., Mitsutani, T., Ro, T., and Yuasa, S., "Effects of Swirling Liquid Oxygen Flow on Combustion of a Hybrid Rocket Engine," *40th AIAA/ASME/SAE/ASEE Joint Propulsion Conference and Exhibit*, Fort Lauderdale, FL: AIAA, 2004, p. AIAA 2004-3479.

3 Sakurai, T., and Tomizawa, T., "Applicability of a LOx Vaporization Preburner for Swirling-Flow Hybrid Rocket Engines," *51st AIAA/SAE/ASEE Joint Propulsion Conference*, Orlando, FL: AIAA, 2015, p. AIAA 2015-4134.

4 Kitagawa, K., and Yuasa, S., "Combustion Characteristics of a Swirling LOX Type

Hybrid Rocket Engine," *Journal of the Japan Societ*y *for Aeronautical and Space Sciences*, vol. 54, 2006, pp. 242–249.

5 Waidmann, W., "Thrust Modulation in Hybrid Rocket Engines," *Journal of Propulsion and Power*, vol. 4, 1988, pp. 421–427.

6 Yuasa, S., Shiraishi, N., Sakamoto, M., Sezaki, C., Hirata, K., and Sakurai, T., "Evaluation Method of C* Efficiency of Swirling-Oxidizer-Flow-Type Hybrid Rocket Engines," *Journal of the Japan Societ*y *for Aeronautical and Space Sciences*, vol. 59, 2011, pp. 97–101.

7 Tamura, T., Saburo, Y., and Kengo, Y., "Effects of Swirling Oxidizer Flow on Fuel Regression Rate of Hybrid Rockets," *35th AIAA/ASME/SAE/ASEE Joint Propulsion Conference and Exhibit*, Los Angeles, California: AIAA, 1999, p. AIAA 99-2323.

# Chapter 4

# Analytical Prediction of Local Fuel Regression Rates in Swirling Oxidizer Flow Type Hybrid Rocket Engines

In the previous chapter, Altering-intensity Swirling Oxidizer Flow Type (A-SOFT) was selected as the most promising candidate of O/F shift elimination technologies in the three candidates. However, the the fuel regression rates behavior using oxidizer swirling injection including Swirling Oxidizer Flow Types (SOFTs) have not been analytically modeled or explained in the previous researches. Originally, analytically understanding physical phenomena of reactive flows in rocket engines have great importance to qualitatively and quantitatively predict the fuel regression behavior, design solid fuel grains, and structures of engines. In this chapter, the classic diffusion limited analysis[1,2,3,4] by Marxman et al. in flat plate turbulent boundary layer are extended to that in axi-symmetric coordinates. Our approaches will follow those of Marxman et al. in 1960s, but some models are added to evaluate effects of circumferential flows. Decay of swirl number along with axial position is a representative model of them. From the comparison of fuel regression behavior between the analytical and experimental results, the characteristics of the flow field and regression rates are discussed. In the following chapter, this analytical technique will be used for the analyses of the experimental results of the firing experiments of the A-SOFTs.

## 4.1. Evaluation of Heat Transfer to the Wall and Fuel Regression Rates of A-SOFTs Using Reynolds Analogy

As explained in Chapter 1, in turbulent boundary layer combustion of hybrid rocket propulsion, heat convection and thermal conduction are dominant in the thermal transfer phenomena to gasify the solid fuels. Marxman et al.[1] used the Reynolds Analogy[5], which refers to the similarity of momentum and energy conservations of incompressible thermal fluid, in order to evaluate the two dominant thermal transport phenomena in flat plate turbulent boundary layer combustion. In this section, this approach is applied in axi-symmetric swirling pipe flows.

The axial component of the incompressible momentum conservation law can be written as

$$\rho u_z \frac{\partial u_z}{\partial z} + \rho u_r \frac{\partial u_z}{\partial r} = \mu_t (\frac{\partial^2 u_z}{\partial r^2} + \frac{1}{r}\frac{\partial u_z}{\partial r}) \tag{4.1}$$

where $\mu_t$ is turbulent viscosity and the axial gradients are assumed to be negligible. The energy conservation law can be written as

$$\rho u_z \frac{\partial T}{\partial z} + \rho u_r \frac{\partial T}{\partial r} = \frac{K}{C_p} (\frac{\partial^2 T}{\partial r^2} + \frac{1}{r}\frac{\partial T}{\partial r}) \tag{4.2}$$

where the friction heat inside fluid was assumed to be negligible. This assumption indicates the heat transfer to the solid wall is assumed to be dominated by both heat convection and thermal conduction. The shapes of Eqs. (4.1) and (4.2) show similarity in terms of $u_z$ and $T$ if the turbulent Prandtl number is 1. In this expression, there is no variable related to circumferential velocity components. Considering the assumption that all the physical quantities are uniform along circumferential direction in axisymmetric flows, no emergence of circumferential components is reasonable. Moreover, when a typical assumption in gaseous flows[2] is used that the turbulent Prandtl number is in the order of magnitude of 1, axial velocity component and temperature have the following relation as

$$\frac{du_z}{u_{z_b} - u_z} = \frac{dT}{T_b - T} \tag{4.3}$$

where $b$ referes to the position of the flame. Because axial differentials are assumed to be far smaller than radial differentials in the turbulent boundary layer, the small differences of axial velocity and temperature can be evaluated as follows:

$$du_z \approx \frac{\tau_{rz}}{\mu_t} dr \tag{4.4a}$$

$$dT \approx -\frac{q_r}{K} dr \tag{4.4b}$$

Using Eqs. (4.3), (4.4a) and (4.4b), the heat flux at the wall can be evaluated as

$$\frac{q_{r_w}}{T_b - T_w} = -\frac{C_p \tau_{rz_w}}{u_{z_b}} \tag{4.5}$$

where the negative symbol is due to the positive direction of $\tau_{rz}$ is shear stress to the axial direction at the outer surface. Using the definition of the enthalpy gap between flame and the wall $\Delta h \equiv C_p(T_b - T_w)$, Eq. (4.5) can be transformed as

$$q_{r_w} = -\frac{\tau_{rz_w}}{u_{z_b}} \Delta h = \frac{C_{f_z}}{2} \frac{\rho_e {u_{z_e}}^2}{u_{b_z}} \Delta h = \frac{C_{f_z}}{2} G_o \left(1 + \frac{1}{O/F(z)}\right) B_t h_v \tag{4.6}$$

where the normalized axial component of wall shear stress was defined for convenience using the dynamic pressure in the main flow as

$$\frac{C_{fz}}{2} \equiv -\frac{\tau_{rz_w}}{\rho_e u_{z_e}^2} \tag{4.7}$$

and $B_t$ at the rightest side of Eq. (4.6) is defined as

$$B_t \equiv \frac{u_{e_z} \Delta h}{u_{b_z} h_v} \tag{4.8}.$$

$h_v$ is the total enthalpy of the solid fuel to gasify, and $B_t$ corresponds to the parameter called as thermochemical blowing parameter[6]. These two parameters only depend on the combination of propellants and the initial thermodynamic state of the reactants and is near to constant through the boundary layer combustion[1]. Note that the heat flux to the wall $q_{r_w}$ can also be expressed by the fuel regression rate in quasi-steady state combustion as

$$q_{r_w} = \rho_f \dot{r} h_v \tag{4.9}.$$

Eq. (4.9) shows that steady fuel regression rates can be evaluated by the heat flux into the wall using Eq. (4.6). $G_o$, $B_t$ and $h_v$ are the initial conditions and the constants, and the local $O/F(z)$ at a cross-section normal to the axial direction is easily calculated by the integration of total fuel mass flow rate from the upstream. Therefore, the only unknown variable is $C_{fz}/2$. The following subsections show the process to evaluate this variable using the initial conditions.

## 4.2. Evaluation of Axial Distributions of Wall Shear Stress in Axi-symmetric Flows

Considering Eq. (4.4a), the wall shear stress can be practically evaluated by modelling the radial distribution of axial velocity component and the turbulent viscosity. Marxman et al. used the equivalence of the two radial distribution models of shear stress in the turbulent boundary layer[3]. One is the Prandtl's mixing length theory[7]. The turbulent

viscosity was approximated by the 1/7 power law[7]. The other one is the first order correction of the blowing effects of the gasified fuel from the wall[8]. The wall shear stress was evaluated from the equivalence of these two expressions and the given boundary conditions. In this subsection, this method is extended and applied to the boundary layer in the swirling pipe flows to evaluate the axial component of wall shear stress with independent variables.

### 4.2.1. Three Dimensional Mixing Length Theory

The mixing length theory should be extended for the three dimensional coordinate. In this subsection, the mixing length model proposed by Czernuszenko and Rylov[9] is introduced. In this paragraph, their mixing length model is briefly summarized in the three dimensional flat plate boundary layer. Let us assume that there is a flat plate normal to the $z$ axis at $z$=0, and the mainstream flows have both velocity components along with x and y axes. In the turbulent boundary layer, each velocity component should be transported by eddies. If the mainstream has both $x$ and $y$ directional components, the eddy should diagonally transport the velocity components as is shown in the upper figure of Figure 4.1. Therefore, the scale of the velocity of the eddy can be expressed as

$$\left|w'(x_0,\, y_0)\right| \approx |u'| + |v'| \qquad (4.10a).$$

Because the disturbances of the velocity components transported by the eddies should be independent of each other as is shown in the bottom figures of Figure 4.1, the transported momentum can be expressed as

$$\rho u'(x_0,\, y_0) \approx \rho l \frac{\partial \bar{u}}{\partial r} \qquad (4.10b)$$

and

$$\rho v'(x_0,\, y_0) \approx \rho l \frac{\partial \bar{v}}{\partial r} \qquad (4.10c)$$

where isotropic turbulent flow is assumed.

Therefore, the three dimensional turbulent shear stress model should be

$$\tau_{xz} = \mu \frac{\partial \bar{u}}{\partial z} - \rho \overline{u'w'} \approx \left\{\mu + \rho l^2 \left(\left|\frac{\partial \bar{u}}{\partial z}\right| + \left|\frac{\partial \bar{v}}{\partial z}\right|\right)\right\} \frac{\partial \bar{u}}{\partial z} \qquad (4.10d).$$

In fact, there are many models for $w'$such as the reference[10] because originally $w'$should not be a simple summation of the disturbances of the velocity components or the square root of sum of their squares. However, in this subsection, for the simplicity of analytical handling, the summation model by Czernuszenko and Rylov is adopted.

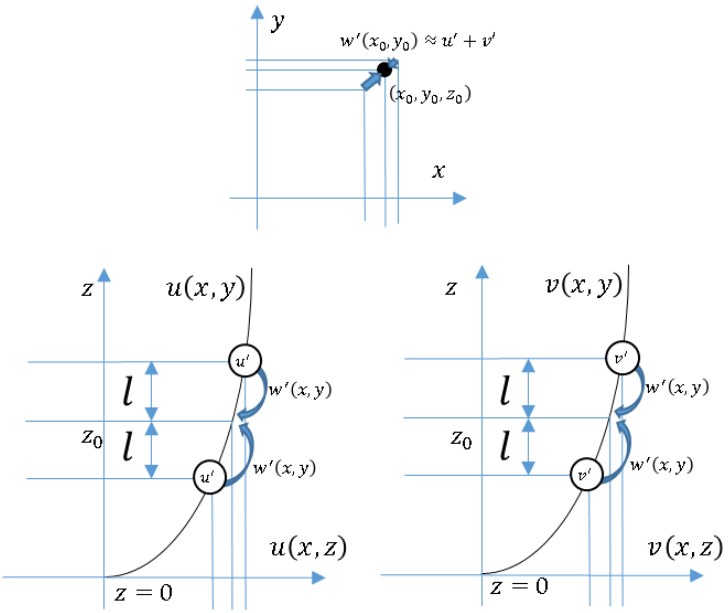


Figure 4.1. Schematics of the concept of three dimensional mixing length theory.

Eq. (4.10d) can be transformed in axi-symmetric coordinate as

$$\tau_{rz} \approx \left\{\mu + \rho l^2 \left(\left|\frac{\partial \overline{u_\theta}}{\partial r} - \frac{\overline{u_\theta}}{r}\right| + \left|\frac{\partial \overline{u_z}}{\partial r}\right|\right)\right\} \frac{\partial \overline{u_z}}{\partial r} \qquad (4.11).$$

This equation is used for the turbulent shear stress model of swirling flows.

4.2.2. Turbulent Shear Stress Model Including Blowing Effects

In this subsection, the second shear stress model including the effects of mass addition from the flat plate is extended to in three axisymmetric flows. This evaluation is based on the work on the two dimensional flat plate turbulent boundary layer by Dorrance and Dore[8].

First, let us summarize the quasi-steady governing equations in axi-symmetric flows as

Mass conservation

$$\frac{\partial \rho u_z}{\partial z} + \frac{\partial \rho u_r}{\partial r} + \frac{\rho u_r}{r} = 0 \tag{4.12}$$

and

Momentum conservation

$$\frac{\partial \rho {u_z}^2}{\partial z} + \frac{\partial \rho u_r u_z}{\partial r} + \frac{\rho u_r u_z}{r} = -\frac{1}{\rho}\frac{\partial p}{\partial z} + \frac{\partial \tau_{zz}}{\partial z} + \frac{\partial \tau_{rz}}{\partial r} + \frac{\tau_{rz}}{r} \tag{4.13a}$$

$$\frac{\partial \rho u_z u_\theta}{\partial z} + \frac{\partial \rho u_r u_\theta}{\partial r} + \frac{2\rho u_r u_\theta}{r} = \frac{\partial \tau_{z\theta}}{\partial z} + \frac{\partial \tau_{r\theta}}{\partial r} + 2\frac{\tau_{r\theta}}{r} \tag{4.13b}$$

When the mean values of physical quantities for the timescale of eddies and their disturbances as

$$\rho = \bar{\rho} + \rho' \tag{4.14a}$$

$$u_i = \overline{u_i} + u_i' \tag{4.14b}$$

$$\rho u_i = \overline{\rho u_i} + (\rho u_i)' \tag{4.14c}$$

$$p = \bar{p} + p' \tag{4.14d}$$

$$\tau_{ij} = \overline{\tau_{ij}} + {\tau_{ij}}' \tag{4.14e}$$

These equations are substituted into the conservation laws and timely averaged for the timescale of the disturbances, and the governing equations should be

$$\frac{\partial \overline{\rho u_z}}{\partial z} + \frac{\partial \overline{\rho u_r}}{\partial r} + \frac{\overline{\rho u_r}}{r} = 0 \tag{4.15a}$$

$$\frac{\partial \overline{\rho u_z}\,\overline{u_z}}{\partial z} + \frac{\partial \overline{\rho u_r}\,\overline{u_z}}{\partial r} + \frac{\overline{\rho u_r}\,\overline{u_z}}{r} + \frac{\partial \overline{(\rho u_z)' u_z'}}{\partial z} + \frac{\partial \overline{(\rho u_r)' u_z'}}{\partial r} + \frac{\overline{(\rho u_r)' u_z'}}{r} = -\frac{1}{\rho}\frac{\partial p}{\partial z} + \frac{\partial \overline{\tau_{zz}}}{\partial z} + \frac{\partial \overline{\tau_{rz}}}{\partial r} + \frac{\overline{\tau_{rz}}}{r} \tag{4.15b}$$

$$\frac{\partial \overline{\rho u_z}\,\overline{u_\theta}}{\partial z} + \frac{\partial \overline{\rho u_r}\,\overline{u_\theta}}{\partial r} + \frac{2\overline{\rho u_r}\,\overline{u_\theta}}{r} + \frac{\partial \overline{(\rho u_z)' u_\theta'}}{\partial z} + \frac{\partial \overline{(\rho u_r)' u_\theta'}}{\partial r} + \frac{2\overline{(\rho u_r)' u_\theta'}}{r} = \frac{\partial \overline{\tau_{z\theta}}}{\partial z} + \frac{\partial \overline{\tau_{r\theta}}}{\partial r} + 2\frac{\overline{\tau_{r\theta}}}{r} \tag{4.15c}$$

Using the mass conservation law of Eq. (4.12), momentum conservation laws can be transformed as

$$\overline{\rho u_z}\frac{\partial \overline{u_z}}{\partial z}+\overline{\rho u_r}\frac{\partial \overline{u_z}}{\partial r}+\frac{\partial \overline{(\rho u_z)'u_z'}}{\partial z}+\frac{\partial \overline{(\rho u_r)'u_z'}}{\partial r}+\frac{\overline{(\rho u_r)'u_z'}}{r}=-\frac{1}{\rho}\frac{\partial p}{\partial z}+\frac{\partial \overline{\tau_{zz}}}{\partial z}+\frac{\partial \overline{\tau_{rz}}}{\partial r}+\frac{\overline{\tau_{rz}}}{r} \quad (4.16a)$$

$$\overline{\rho u_z}\frac{\partial \overline{u_\theta}}{\partial z}+\overline{\rho u_r}\frac{\partial \overline{u_\theta}}{\partial r}+\frac{\overline{\rho u_r u_\theta}}{r}+\frac{\partial \overline{(\rho u_z)'u_\theta'}}{\partial z}+\frac{\partial \overline{(\rho u_r)'u_\theta'}}{\partial r}+\frac{2\overline{(\rho u_r)'u_\theta'}}{r}=\frac{\partial \overline{\tau_{z\theta}}}{\partial z}+\frac{\partial \overline{\tau_{r\theta}}}{\partial r}+2\frac{\overline{\tau_{r\theta}}}{r} \quad (4.16b).$$

Here, using the viscous shear stress models as

$$\tau_{rz}\approx\mu\left(\frac{\partial \overline{u_z}}{\partial r}+\frac{\partial \overline{u_r}}{\partial z}\right) \quad (4.17a)$$

$$\tau_{r\theta}\approx\mu\left(\frac{\partial \overline{u_\theta}}{\partial r}-\frac{\overline{u_\theta}}{r}\right) \quad (4.17b)$$

and the approximation of scales of differentials in turbulent boundary layers as

$$\frac{\partial f}{\partial z}\ll\frac{\partial f}{\partial r} \quad (4.18),$$

Eqs. (4.16a) and (4.16b) are transformed as

$$\overline{\rho u_z}\frac{\partial \overline{u_z}}{\partial z}+\overline{\rho u_r}\frac{\partial \overline{u_z}}{\partial r}=\frac{1}{r}\frac{\partial r\{\overline{\tau_{rz}}-\overline{(\rho u_r)'u_z'}\}}{\partial r}=\frac{1}{r}\frac{\partial r\tau_{t_z}}{\partial r} \quad (4.19a)$$

$$\overline{\rho u_z}\frac{\partial \overline{u_\theta}}{\partial z}+\overline{\rho u_r}\frac{\partial \overline{u_\theta}}{\partial r}+\frac{\overline{\rho u_r u_\theta}}{r}=\frac{1}{r^2}\frac{\partial r^2\{\overline{\tau_{r\theta}}-\overline{(\rho u_r)'u_\theta'}\}}{\partial r}=\frac{1}{r^2}\frac{\partial r^2\tau_{t_\theta}}{\partial r} \quad (4.19b)$$

where $\tau_t$ is defined as turbulent shear stress. $\overline{(\rho u_z)'u_z'}$ and $\overline{(\rho u_z)'u_\theta'}$ are assumed to respectively have the scales of $\overline{(\rho u_r)'u_z'}$ and $\overline{(\rho u_r)'u_\theta'}$ due to the scales of momentum transportation driven by eddies. Using the primary Taylor expansion at the wall along radial direction, $\left(\tau_{t_z}-(\overline{\rho u_r})_w\overline{u_z}\right)$ and $\left(\tau_{t_\theta}-(\overline{\rho u_r})_w\overline{u_\theta}\right)$ are approximated as

$$r\left(\tau_{t_z}-(\overline{\rho u_r})_w\overline{u_z}\right)=R\tau_{zw}+\frac{\partial r\left(\tau_{t_z}-(\overline{\rho u_r})_w\overline{u_z}\right)}{\partial r}\Big|_R(r-R)+\mathcal{O}((r-R)^2)\approx R\tau_{zw} \quad (4.20a)$$

$$r^2\left(\tau_{t_\theta} - (\overline{\rho u_r})_w \overline{u_\theta}\right) = R^2\tau_{\theta w} + \frac{\partial r^2(\tau_{t\theta} - (\overline{\rho u_r})_w \overline{u_\theta})}{\partial r}|_R (r-R) + o((r-R)^2) \approx R^2\tau_{\theta w} \qquad (4.20b)$$

where the following evaluations were used as

$$\frac{\partial r(\tau_{t_z} - (\overline{\rho u_r})_w \overline{u_z})}{\partial r}|_R = \left(\frac{\partial r\tau_{t_z}}{\partial r} - (\overline{\rho u_r})_w \frac{\partial r\overline{u_z}}{\partial r}\right)|_R - (\overline{\rho u_r})_w \overline{u_z}|_R = 0 \qquad (4.21a)$$

$$\frac{\partial r^2(\tau_{t\theta} - (\overline{\rho u_r})_w \overline{u_\theta})}{\partial r}|_R = \left(\frac{\partial r^2\tau_{t\theta}}{\partial r} - (\overline{\rho u_r})_w \frac{\partial r^2\overline{u_\theta}}{\partial r}\right)|_R - 2R(\overline{\rho u_r})_w \overline{u_\theta}|_R = 0 \qquad (4.21b).$$

The following transformation of Eqs. (4.20a) and (4.20b) yield the first order approximation of radial distribution of shear stress as

$$\tau_{t_z} = \frac{R}{r}\tau_{zw} + (\overline{\rho u_r})_w \overline{u_z} = \tau_{zw}\left(\frac{R}{r} + \frac{(\overline{\rho u_r})_w}{C_{f_z}/2\, u_{z_e}} \frac{\overline{u_z}}{u_{z_e}}\right) = \tau_{z_w}\left(\frac{R}{r} + B_z\varphi_z\right) \approx \tau_{z_w}(1 + B_z\varphi_z) \qquad (4.22a)$$

$$\tau_{t_\theta} = \frac{R^2}{r^2}\tau_{\theta w} + (\overline{\rho u_r})_w \overline{u_\theta} = \tau_{\theta_w}\left(\frac{R^2}{r^2} + \frac{(\overline{\rho u_r})_w}{C_{f_\theta}/2\, u_{\theta_e}} \frac{r}{R}\frac{\omega}{\omega_e}\right) = \tau_{\theta_w}(1 + B_\theta\overline{\omega}) \qquad (4.22b)$$

where $\frac{(R-r)}{R} \ll 1$ is assumed. $B_z \equiv \frac{(\overline{\rho u_r})_w}{C_{f_z}/2\, u_{z_e}}$ and $B_\theta = \frac{(\overline{\rho u_r})_w}{C_{f_\theta}/2\, u_{\theta_e}}$ are the counterparts of aerodynamic blowing parameter $B_a \equiv \frac{(\overline{\rho u_r})_w}{C_f/2\, u_e}$ in axial hybrids. From the evaluations of the heat flux at the solid fuel surface Eq.(4.6) and Eq.(4.9), the equivalence of $B_z$ to $B_t$ in quasi-steady state can be shown as

$$\rho_f \dot{r} h_v = \frac{C_{f_z}}{2} G_e \frac{u_{e_z}\Delta h}{u_{b_z}} \Leftrightarrow B_a = \frac{(\overline{\rho u_r})_w}{C_f/2\, G_e} = \frac{u_{e_z}\Delta h}{u_{b_z} h_v} = B_t \qquad (4.23).$$

4.2.3. Evaluation of Wall Shear Stress

In this subsection, using the two models of turbulent shear stress, $C_{f_z}/2$ is evaluated with other representative variables of the flow fields. Combining Eq. (4.11) with Eq. (4.22a) yields

$$\tau_{z_w}(1+B_z\varphi_z)=\left\{\mu+\rho l^2\left(\left|\frac{\partial\overline{u_\theta}}{\partial r}-\frac{\overline{u_\theta}}{r}\right|+\left|\frac{\partial\overline{u_z}}{\partial r}\right|\right)\right\}\frac{\partial\overline{u_z}}{\partial r} \quad (4.24).$$

The turbulent viscosity is evaluated by substituting the following 1/7 power laws of the individual velocity components as

$$\varphi_z={\eta_z}^{n_z} \quad (4.25a)$$

$$\overline{\omega}={\eta_\theta}^{n_\theta} \quad (4.25b)$$

where $n_z=n_\theta=1/7$ is assumed. $\eta_z$ and $\eta_\theta$ are respectively the normalized distances from the wall by momentum boundary layer thicknesses $\delta_z$ and $\delta_\theta$ as

$$\eta_z\equiv\frac{R-r}{\delta_z},\eta_\theta\equiv\frac{R-r}{\delta_\theta} \quad (4.26).$$

The names of these two parameters, "momentum boundary layer thicknesses", are designated just for convenience because momentum boundary thickness is defined on the plane consisting of the streamline and normal vector of the wall. $\delta_z$ and $\delta_\theta$ mean the scale of the distance affected by the existence of the wall. For simplicity, isotropic mixing lengths in proportion to distance from the wall are assumed as

$$l=\kappa(R-r),\kappa=0.4 \quad (4.27).$$

These models are substituted into Eq.(4.24) as

$$\frac{C_{f_z}}{2}\frac{u_{ze}(R-\delta_\theta)}{\kappa^2 n_\theta\delta_z u_{\theta e}}(1+B_z\varphi_z)=\left\{{\eta_z}^2-\frac{R-\delta_\theta}{\delta_z}\left(1+\frac{n_z u_{ze}}{n_\theta u_{\theta e}}\right)\eta_z-\frac{u_{ze}(R-\delta_\theta)}{\kappa^2 Re_{\delta_z} n_\theta\delta_z u_{\theta e}}\right\}\frac{\partial\varphi_z}{\partial\eta_z} \quad (4.28).$$

Equation (4.28) can be integrated to radial direction from the edge of the boudary layer to the fuel port wall. This integration results in

$$\frac{C_{f_z}}{2}\approx\frac{\kappa^2\left(n_\theta\frac{u_{\theta e}}{u_{ze}}+n_z\right)}{\ln\left\{1+\kappa^2 Re_{\delta_z}\left(n_\theta\frac{u_{\theta e}}{u_{ze}}+n_z\right)\right\}}\frac{\ln(1+B_z)}{B_z} \quad (4.29)$$

where $R\gg\delta_z,\delta_\theta$ and $\kappa^2 Re_{\delta_z}n_\theta\gg 1$ are assumed to approximate the exact solution. Eq. (4.29) can be more approximated into a simpler equation as

$$\frac{C_{f_z}}{2}\left(\frac{u_{\theta e}}{u_{ze}}, \frac{O}{F}, \delta_z\right) \approx \alpha\left(1+\frac{u_{\theta e}}{u_{ze}}\right)^{0.85} Re_{\delta_z}{}^{-0.25\,\frac{\ln(1+B_z)}{B_z}} \qquad (4.30).$$

When $u_{\theta e}$ is zero in axial flow, $C_{f_z}/2$ , $B_z$ and $\delta_z$ are equivalent to $C_f/2$, $B_a$ and $\delta$ in axial hybrids. In that case, Eq. (4.30) is the same form as the one of friction coefficient derived in the "diffusion limited analysis" by Marxman et al.[2], and $\alpha$ is 0.0225 in a developing turbulent boundary layer[7]. Moreover, Eq. (4.30) has the same form of the wall friction coefficient in fully developed turbulent flows[7] if $\delta$ is replaced by $R$. In that case, $\alpha$ is said to be 0.0333[7]. In Figure 4.2, the approximation of the first term of the right side of Eq. (4.30) is compared with that in Eq. (4.29). Eq. (4.30) approximates Eq. (4.29) with a good accuracy. However, Eq.(4.30) still have the two unknown variables of $u_{\theta e}/u_{ze}$ and $\delta_z$. Therefore, how $\delta_z$ develops and $u_{\theta e}/u_{ze}$ decays along with axial direction should be evaluated by known variables.

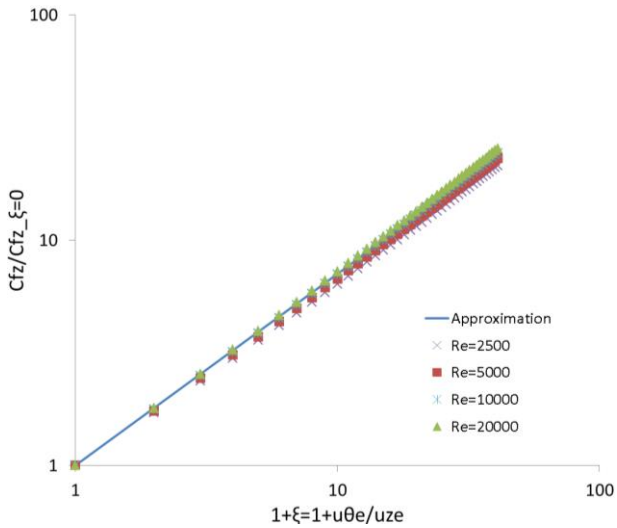


Figure 4.2. Comparison between Eq. (4.29) and its approximation Eq. (4.30). This approximation enables to easily handle the effects of swirl with a good accuracy.

## 4.3. Boundary Layer Thickness Evaluation Using Karman's Momentum Integration

In this section, boundary layer thickness on axial velocity component $\delta_z$ is evaluated using the Karman's momentum integral equation in axisymmetric pipe flows. First, the Karman's momentum integral in a axi-symmetric coordinate is derived. The quasi-steady conservation laws in incompressible axi-symmetric flows are

Mass conservation law $$\frac{\partial u_z}{\partial z}+\frac{\partial u_r}{\partial r}+\frac{u_r}{r}=0 \tag{4.31}$$

Momentum conservation law

$$u_z\frac{\partial u_z}{\partial z}+u_r\frac{\partial u_z}{\partial r}=-\frac{1}{\rho}\frac{\partial P}{\partial z}+\frac{\mu}{\rho}\left(\frac{\partial^2 u_z}{\partial r^2}+\frac{1}{r}\frac{\partial u_z}{\partial r}\right) \tag{4.32a}$$

$$\frac{{u_\theta}^2}{r}=\frac{1}{\rho}\frac{\partial P}{\partial r} \tag{4.32b}$$

$$u_z\frac{\partial u_\theta}{\partial z}+u_r\frac{\partial u_\theta}{\partial r}+\frac{u_r u_\theta}{r}=\frac{\mu}{\rho}\left(\frac{\partial^2 u_\theta}{\partial r^2}+\frac{1}{r}\frac{\partial u_\theta}{\partial r}-\frac{u_\theta}{r^2}\right) \tag{4.32c}$$

where axial partial differentials in the viscous terms are ignored because radial differentials have far larger scales in the turbulent boundary layer. Eq. (4.31)$\times\, ru_z$+Eq. (4.32.a) $\times\, r$ and the partial integration of Eq. (4.31) yield the following momentum integral as

$$\frac{\partial}{\partial z}\int_R^{R-\delta_z} r{u_z}^2 dr-u_{ze}\frac{\partial}{\partial z}\int_R^{R-\delta_z} ru_z dr=-\frac{R\tau_{rz_w}}{\rho}(1+B_z)-\int_R^{R-\delta_z}\frac{r}{\rho}\frac{\partial P}{\partial z}dr \tag{4.33}$$

where $(\rho u_r)_w$ is handled as a non-zero variable because the fuels are gasified from the solid fuel wall. In axial flows, the term of $\frac{\partial}{\partial z}\left(\frac{rP}{\rho}\right)$ is typically evaluated with the velocity of the main flows[7] because $\frac{\partial P}{\partial r}$ is evaluated as 0. However, in swirling flows, this assumption cannot always be used due to radial pressure gradient in Eq. (4.32b). In order to model the pressure gradient term, we observed the result of the Large Eddy Simulation (LES) by Motoe et al.[11] as is shown in Figure 4.3. This figure shows the radial and axial distributions of chamber pressure in a SOFT hybrid rocket engine of $S_g$=19.4. In these figures, the pressure increases along increasing radial position especially in the vortex core, but center-to-wall pressure ratio is almost constant. In this chapter, the axial pressure gradient at the edge of the boundary layer is ignored because of the following evaluations. First, the axial pressure gradient of the main flows are evaluated from Eq. (4.32a) as

$$\left.\frac{\partial P}{\partial z}\right|_{R-\delta_z}=\left.\left(u_z\frac{\partial u_z}{\partial z}+u_r\frac{\partial u_z}{\partial r}\right)\right|_{r=R-\delta_z}\sim\left.\left(u_z\frac{\partial u_z}{\partial z}+u_r\frac{\partial u_z}{\partial r}\right)\right|_{r=0}\sim 0 \tag{4.34}$$

This evaluation just means that the pressure gradient at the outer edge of boundary layer can be ignored. From the right figure of Figure 4.3, pressure at the solid wall can be evaluated as $P(z,R)\sim 1.1P(z,0)$, and the axial pressure gradient around the wall is evaluated from Eq. (4.32a) as

$$\frac{\partial}{\partial z}P(z,r\sim R)\sim 1.1\frac{\partial}{\partial z}P(z,0)\sim 0 \qquad (4.35).$$

This result shows that the axial pressure gradient in the boundary layer of swirling flows is negligible if Eq. (4.34) is assumed. That is why the second term of the right side of Eq. (4.32a) is handled as 0.

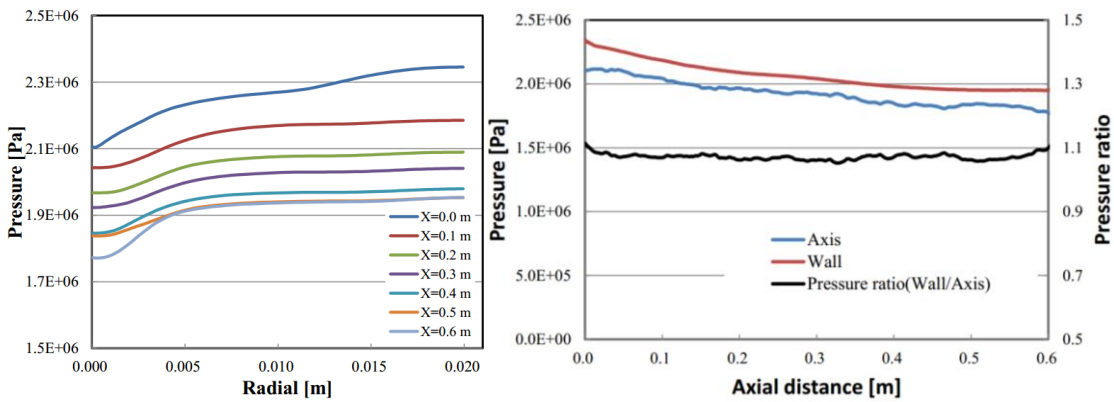


Figure 4.3. Distributions of radial pressure (left) and axis-to-wall pressure ratio (right) from the results of the CFD of a SOFT hybrid rocket engine[11].

In order to evaluate the Karman's momentum integral, the radial distribution model of velocity component $\varphi_z$ should also be modelled. As Marxman et al. did[1], our model is derived from the following assumptions: 1) $\varphi_z$ is expressed as a function of $\eta_z$ and $B_z$, namely $\varphi_z(\eta_z, B_z)$, 2) boundary conditions of $\varphi_z(\eta_z = 0, B_z) = 0$ and $\varphi_z(\eta_z = 1, B_z) = 1$, and 3) 1/7 law of $\varphi_z(\eta_z, B_z = 0) = \eta_z^{n_z}$ is satisfied in $B_z = 0$. The velocity distribution model to satisfy these conditions is derived from the shear stress models in the subsection 4.2.1 and 4.2.2 as

$$\tau_{rz} = \mu_t \frac{u_{z_e}}{\delta_z}\frac{\partial \varphi_z}{\partial \eta_z} = \tau_{rz_w}(1 + B_z\varphi_z) \qquad (4.36)$$

$$\frac{\partial \varphi_z}{\partial \eta_z} = \frac{\tau_{rz_w}\delta_z}{\mu_t u_{z_e}}(1 + B_z\varphi_z) \quad (4.37).$$

From the first assumption, $\frac{\tau_{rz_w}\delta_z}{\mu_t u_{z_e}}$ should be expressed only by $B_z$ and $\eta_z$. One of the velocity gradient models to fulfill the first and third assumptions is

$$\frac{\partial \varphi_z}{\partial \eta_z} = f(B_z)\eta_z^{n_z-1}(1 + B_z\varphi_z) \quad (4.38).$$

In order to determine $f(B_z)$, the second assumption is used by integrating Eq. (4.38), and the following solution is acquired as

$$f(B_z) = n_z \frac{\ln(1+B_z)}{B_z} \quad (4.39)$$

$$\varphi_z = \frac{\exp\{\eta_z^{n_z}\ln(1+B_z)\}-1}{B_z} \quad (4.40).$$

In this thesis, as is in the previous papers[2], the first and second order approximation respectively on $B_z$ and $\eta_z^{n_z}$

$$\varphi_z = \frac{\eta_z^{n_z}(1+B_z\eta_z^{n_z}/2)}{1+B_z/2} \quad (4.41)$$

is applied to Eq. (4.40) as

$$\frac{7(40B_z^2+143B_z+110)}{1980(B_z+2)^2}\frac{\partial \delta_z}{\partial z} \approx \frac{C_{f_z}}{2}\left(\frac{u_{\theta e}}{u_{ze}}, \frac{O}{F}, \delta_z\right)(1 + B_z) \quad (4.42).$$

Eq. (4.42) is the momentum integral equation used in this chapter in the three dimensional axisymmetric coordinates to evaluate the development of $\delta_z$ along with axial direction. Combining Eq. (4.42) wtih Eq. (4.30) can eliminate $C_{f_z}/2$, but $u_{\theta e}/u_{ze}$ and O/F ratio in Eq. (4.30) are still unknown variables. In the following section, $u_{\theta e}/u_{ze}$ is evaluated from geometric swirl number.

## 4.4. Axial Distribution Model of Swirl Number

Higher regression rates of SOFTs seem to be realized by the enhancement of mixing effects driven by eddies. This effect appeared in the term of turbulent viscosity in Eq. (4.24), and the prior section revealed that this effect is transformed into representative axial to circumferential velocity component ratio $u_{\theta e}/u_{ze}$. In this section, $u_{\theta e}/u_{ze}$ is evaluated by geometric swirl number and gas dynamics of main flows.

In axi-symmetric flows, swirl number is defined with the following equation as

$$S \equiv \frac{\int_0^R 2\pi r^2 G_z u_\theta dr}{R\int_0^R 2\pi r G_z u_z dr} \tag{4.43}$$

where the numerator and the denominator respectively refer to angular momentum and the multiplication of port radius and axial momentum of the flow. Generally, circumferential velocity component in swirling pipe flows decays along with axial direction. Though there are some researches of experiments[12] or computation[13] on weak cold swirling pipe flows, those of velocity distributions on hot swirling pipe flow of strong swirl number are rarely found. The former researches claim that the decay of swirl number is caused by that of angular momentum due to wall shear stress and swirl number exponentially decays along with axial position.

However, the simulation of combustive flow of SOFTs by Motoe et al.[11] showed totally different characteristics of the decay of swirl number from those of cold flows. The left figure of Figure 4.5 shows the axial distribution of swirl number from the result of the CFD [11] and swirl number steeply decreased with the different curve from exponential curves. The dominant mechanism of the steep decrease is the rapid acceleration of the axial velocity due to combustion. The right figure of Figure 4.5 shows the axial distributions of the angular momentum and axial momentum. The axial momentum rapidly increases along increasing axial direction though angular momentum slightly changes after its development in the head-end region.

In this section, an axial distribution of swirl number is analytically modeled by the simple Euler equations on compressible gas dynamics. In order to model swirl number decay, several conditions are assumed that 1) thermodynamic status is uniform in main flows over a cross-section normal to the center axis, 2) mixture ratio does not exceed the optimum one

to maximize adiabatic flame temperature over the fuel port, 3) specific heat at constant pressure does not have sensitivity to temperature, and 4) transformed enthalpy of burnt gases into kinetic energy is so small.

The temperature distribution and molecular weight are modeled as functions of O/F ratio. If gaseous temperature is calculated as an interpolation between the pure oxidizer and the burnt products of the maximum adiabatic flame temperature, it can be approximated as a function of inverse of O/F ratio $F/O$ from energy conservation law:

$$T = \frac{\left(\frac{F}{O}\right)_{op}\left(1+\frac{F}{O}\right)C_{p_{op}}(T_{op}-T_o)}{C_{p_{op}}\left(1+\left(\frac{F}{O}\right)_{op}\right)\frac{F}{O}+C_{p_o}\left(\left(\frac{F}{O}\right)_{op}-\frac{F}{O}\right)} + T_0 \tag{4.44}$$

and averaged molecular weight can be also approximated as a function of $F/O$ as

$$W = \frac{\left(\frac{F}{O}\right)_{op}\left(1+\frac{F}{O}\right)W_o W_{op}}{W_o\left(1+\left(\frac{F}{O}\right)_{op}\right)\frac{F}{O}+W_{op}\left(\left(\frac{F}{O}\right)_{op}-\frac{F}{O}\right)} \tag{4.45}$$

Secondly, by solving mass and momentum conservation laws of the one dimensional Euler equations[14] using Eqs. (4.44) and (4.45). The approximated solutions can be written as

$$\begin{cases} P \approx P_0 + \frac{G_O^2\left(1+\frac{F}{O}\right)^2}{P_0}RT \\ \rho \approx \frac{P_0}{RT} + \frac{G_O^2\left(1+\frac{F}{O}\right)^2}{P_0} \\ u_z \approx \frac{G_o\left(1+\frac{F}{O}\right)RT}{P_0+\frac{R_0T_0}{P_0}G_O^2} \end{cases} \tag{4.46}$$

where $P_0$ refers to total pressure of oxidizer at the head end of the fuel port, and $\frac{G_O^2\left(1+\frac{F}{O}\right)^2}{P_0^2}RT \ll 1$ is assumed.

Circumferential velocity profile along axial direction is evaluated from the assumptions of angular momentum conservation. In this section, it is assumed that radial distribution of circumferential velocity is similar along with axial direction and radial distribution of axial mass flux is uniform. These assumptions yield the following relation as

$$\int_0^R 2\pi r^2 G u_\theta dr = G_o\left(1+\frac{F}{O}\right)\int_0^R 2\pi r^2 u_\theta dr = \pi R^3 I G_o\left(1+\frac{F}{O}\right)u_{\theta_e} = \pi R^3 I G_o u_{\theta_{e_0}} \tag{4.47}$$

where $I = \int_0^1 2x^2 u_\theta / u_{\theta_e} dx$ is a constant coefficient dependent on radial distribution of circumferential velocity. From these evaluations, swirl number can be calculated as

$$S(O/F) = \frac{2\pi \int_0^R r^2 G u_\theta dr}{R 2\pi \int_0^R r G u_z dr} = I \frac{u_{\theta_e}}{u_{z_e}} = I \frac{u_{\theta_{e_0}}}{u_{z_{e_0}}} \frac{WT_0}{W_0 T} \frac{1}{\left(1+\frac{F}{O}\right)^2} = S_0 \frac{WT_0}{W_0 T} \frac{1}{\left(1+\frac{F}{O}\right)^2} \quad (4.48).$$

This is the decay of swirl number and representative velocity component ratio. Swirl number is evaluated as a function of initial velocity component ratio, radial distribution of circumferential velocity, molecular weights of propellants, ambient temperature, and O/F ratio. In this function, the only unknown variable to calculate swirl number is O/F ratio and initial swirl number. Eq. (4.48) also indicates that swirl number is proportional to circumferential-to-axial representative velocity component ratio, and swirl number is equivalent to the velocity component ratio if the circumferential distribution is a free vortex.

This model is validated with the research by Motoe et al.[11] in Figure 4.4. In the referential study, oxidizer and fuel are respectively assumed to be oxygen and methane. This referential study is convenient for the validation because this study gives the axial distribution of mass flux addition from the wall in advance.

The initial conditions of our model are the averaged molecular weight, the adiabatic flame temperature under constant pressure, and specific heat. These conditions are quoted from the result of NASA-CEA[15]. Initial swirl number is assumed to be equal to geometric swirl number of the injector used in the simulation. As explained in the previous chapters, geometric swirl number is the ideal swirl number of the injector and actually defined by the following equation as

$$S_g = \frac{R_m \rho u_{inj}^2 A_{inj}}{R \rho u_{z_e}^2 A_{port}} = \frac{R_m A_{port}}{R A_{inj}} \quad (4.49)$$

In this validation, free vortex in the main flow, $I = 1$ is assumed. Figure 4.5 shows the comparison of analytical swirl number model from Eq. (4.48) with the result of the referential study[11]. Our analytical model fit well the reference except in the region inside tangential injector in the upstream of the start point of the fuel port. Let us call this area as "pre-combustion region". The referred paper[11] reported that reverse pressure around the vortex core was created by the large mass flux addition at the head end of the fuel port. The reverse flow was considered to carry some of the hot burnt gases and swirl number started

to decrease even in the pre-combustion region. However, this region should not strongly affect the regression rate behavior and the two models of swirl number agreed well in the fuel port. Therefore, our model is applied to the diffusion limited analysis for SOFTs in the next section.

In this section, swirl number and velocity component ratio model were created and to enable numerical integration of $\delta_z$ with Eqs. (4.30), (4.42) and (4.48).

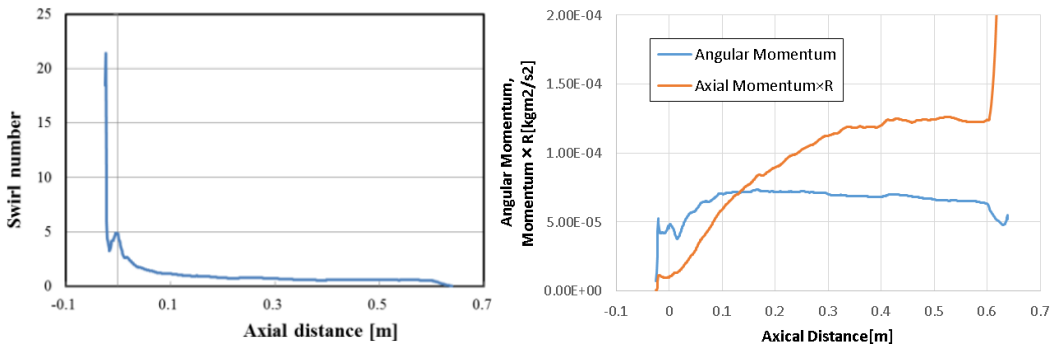


Figure 4.4. Axil distributions of swirl number[11] (left) and axial distributions of axial momentum and angular momentum (right) from the results of the CFD of a SOFT hybrid rocket engine. The right figure is produced by the results of CFD from the reference[11].

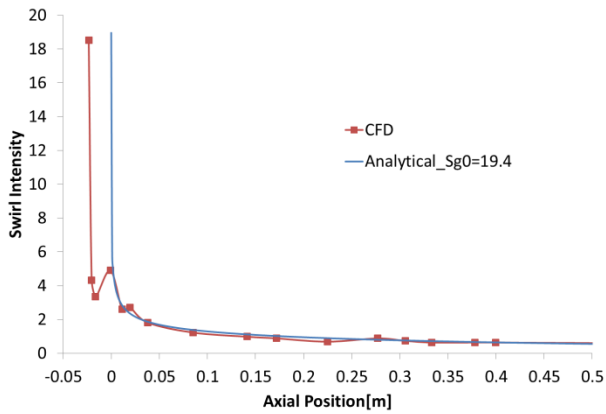


Figure 4.5. Comparison of local swirl number between the analytical model and the result of CFD[11].

## 4.5. Evaluation Schemes of Axial Distribution of Wall Shear Stress, Boundary Layer Thickness and Local Regression Rates in Swirling Oxidizer Flow Type Hybrid Rocket

Engines

In this section, the evaluation scheme of axial distribution of wall shear stress, boundary layer thickness and local regression rates along with axial direction are constructed. This scheme is built for the two situations of the flows. One is for the developing turbulent boundary layer and the other is for the fully developed turbulent pipe flow. Usually, solid fuel ports in axial hybrid rocket engines do not have enough length for boundary layer thickness to reach the center of fuel port and to transit to fully developed turbulent pipe flows. That is why the developing boundary layer is rather significant to understand the fuel regression behavior[6] in conventional axial hybrid rocket engines. However, the boundary layer in SOFTs can rapidly develop because actual flow paths in swirling flows can be far longer than those of axial hybrid rocket engines due to the circumferential velocity component of the mainstream. In our calculation scheme, the developing turbulent boundary layer scheme shifts to the developed turbulent pipe flow scheme once the boundary layer thickness reaches the port radius. Originally, transitions to the fully developed pipe flow should be discussed. However, for simplicity of calculations, the transition from developing boundary layer to turbulent pipe flow is not discussed in this thesis.

Though the thermal transportation in swirling hybrids was modelled until the prior section, O/F ratio is still a remained unknown variable. The distribution of O/F ratio is evaluated by the definition of aerodynamic blowing parameter $B_z$ as

$$B_z \equiv \frac{2(\rho u_r)_w}{C_{f_z} G} = \frac{2\rho_f \dot{r}}{C_{f_z} G} = \frac{R}{C_{f_z}} \frac{d \ln\left(1+\frac{F}{O}\right)}{dz} \qquad (4.50).$$

This relation can be transformed as

$$\frac{d \ln(1+F/O)}{dz} = \frac{B_z}{R} C_{f_z} \qquad (4.51).$$

Eqs. (4.30), (4.42), (4.48) and (4.51) are the closed system for numerical integrations of $(u_{\theta e}/u_{ze}, O/F, \delta_z)$ along with axial direction. In the following subsections, the practical calculation schemes are discussed.

4.5.1. The Developing Turbulent Boundary Layer Scheme

As modeled in the prior sections, the developing turbulent boundary layer scheme in SOFTs consists of the following 4 equations of Eqs. (4.30), (4.42), (4.48) and (4.51) as

$$\frac{d\ln(1+F/O)}{dz} = \frac{B_z}{R}\alpha_0\left\{1 + S_0\frac{WT_0}{W_0T}\left(1+\frac{F}{O}\right)^{-2}\right\}^{0.85} Re_{\delta_z}{}^{-0.25}\frac{\ln(1+B_z)}{B_z} \tag{4.52}$$

$$\frac{\partial\delta_z}{\partial z} \approx \alpha_0\left(1 + S_0\frac{WT_0}{W_0T}\left(1+\frac{F}{O}\right)^{-2}\right)^{0.85} Re_{\delta_z}{}^{-0.25}\frac{1980(B_z+2)^2(1+B_z)}{7(40B_z^2+143B_z+110)}\frac{\ln(1+B_z)}{B_z} \tag{4.53}$$

where $\alpha_0$ is 0.0225, a constant in flat plate developing turbulent boundary layer. These equations are simultaneous ordinary differential equations on $\delta_z(z)$ and $F/O(z)$. Practically, these equations are numerically solved using the 4th order Runge-Kutta method[16]. Local regression rates along with axial direction are calculated from the solutions of $\delta_z(z)$ and $F/O(z)$ using the following equation derived from Eqs. (4.23), (4.30) and (4.48) as

$$\rho_f\dot{r} = \alpha_0\left\{1 + S_0\frac{WT_0}{W_0T}\left(1+\frac{F}{O}\right)^{-2}\right\}^{0.85} G_o\left(1+\frac{F}{O}\right)Re_{\delta_z}{}^{-0.25}\ln(1+B_z) \tag{4.54}$$

4.5.2. The Developed Turbulent Pipe Flow Scheme

After the transition to developed turbulent pipe flows, Eq. (4.53) is not appropriate to describe the characteristics of the flow field because $\delta_z$ is constant. In this scheme, instead of Eq. (4.53), $\delta_z = R$ is substituted to Eq. (4.52) as

$$\frac{d\ln(1+F/O)}{dz} = \frac{B_z}{R}\alpha_1\left\{1 + S_0\frac{WT_0}{W_0T}(1+F/O)^{-2}\right\}^{0.85} Re_R{}^{-0.25}\frac{\ln(1+B_z)}{B_z} \tag{4.55}$$

where $\alpha_1$ is 0.0333, a constant in developed turbulent pipe flows. This equation is also numerically solved using the 4th order Runge-Kutta method[16]. Local regression rates along with axial direction are calculated from the solutions of $F/O(z)$ using the following equation derived from Eq. (4.54) as

$$\rho_f \dot{r} = \alpha_1 \left\{1 + S_0 \frac{WT_0}{W_0 T}\left(1 + \frac{F}{O}\right)^{-2}\right\}^{0.85} G_o \left(1 + \frac{F}{O}\right) Re_R{}^{-0.25} \ln(1 + B_z) \qquad (4.56).$$

## 4.6. Results and Discussions

The results of our model are compared with a set of experiments by Yuasa et al.[17] In the referential study, the time-averaged local regression rates of a lab-scale SOFT hybrid rocket engine in different geometric swirl numbers were measured. Their initial port radius and port length are 20 [mm] and 500 [mm] respectively. The propellants are polymethyl methacrylate (PMMA) and gaseous oxygen. The oxidizer mass flow rate was 90 [g/s] and the burn time was less than 10 [s]. The options of the geometric swirl number were 0, 9.7 and 19.4. According to the experimental estimation[3], the blowing parameter is evaluated as $B_t = B_z \sim 10$. $S_0 = S_g$ is given in the analytical scheme as discussed in the previous section. Though the viscosity of $\mu = 1.0 \times 10^{-5}$ [Pa · s] in the same order of the air in ambient temperature seems to be used in the analyses by Yuasa et al.[18], this order seems not to be correct because gaseous viscosities are subject to the Sutherland's formula[19]. In this chapter, $\mu = 1.0 \times 10^{-4}$ [Pa · s] is assumed because gaseous viscosities are proportional to $\sqrt{T}$ according to the kinetic theory[20,21].

Figure 4.6 shows the comparison of the analytical approach (curves) using only the developing turbulent boundary layer scheme with the experimental data of the local regression rates (dots). In this figure, the purple, red, and blue colors respectively refer to the geometric swirl numbers of 19.4, 9.7, and 0. The broken lines refer to the axial position where the boundary layer thickness is equal to the port radius. The analytical solution of the local regression rates of the axial hybrid rocket engine showed a good agreement except in the region between 0.1 and 0.2 [m]. In this case, the axial position where the boundary layer thickness $\delta_z$ reached the port radius $R$ was at 0.4[m] near to the tail end of the fuel port, and the transition to developed pipe flows should hardly affect the regression rate behavior. On the other hand, in the SOFTs, the analytical scheme assuming developing boundary layer does not have a good agreement especially in the downstream of the middle of the fuel port. These disagreements are quite natural because the distance between flame and the solid fuel port wall was not appropriately evaluated. Figure 4.7 shows the development of the boundary layer thickness in all the cases. The broken line refers to the port radius. The maximum boundary layer thickness $\delta_z$ was not limited to the port radius in these calculations, and $\delta_z$ reached the double of the port radius especially in the case of $S_g$=19.4. These artificial developments of the boundary layers seemed to make heat flux to the solid

fuel too less and result in too small local regression rates in the downstream region of the fuel port.

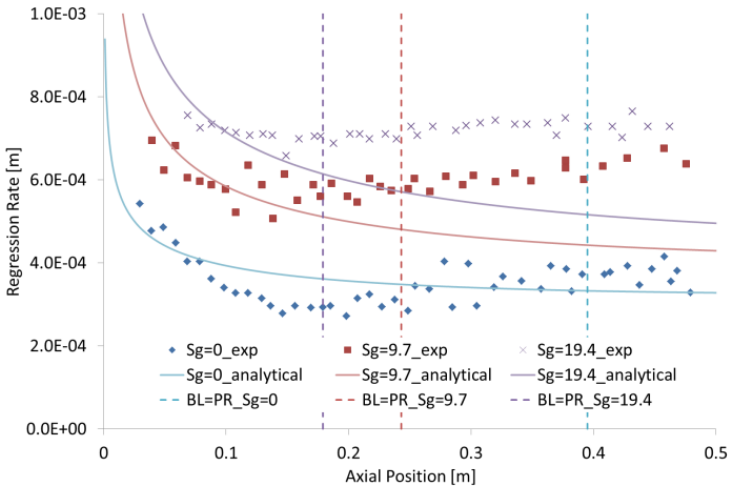


Figure 4.6. Comparison of local regression rates by extended Marxman's diffusion limited analysis for SOFTs with the set of experimental data[17].

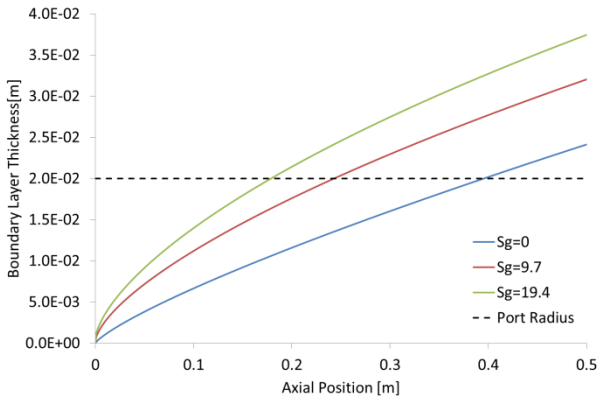


Figure 4.7. Axial distributions of turbulent boundary layer thickness by the extended Marxman's diffusion limited analysis for SOFT-HREs.

Figure 4.8 and Figure 4.9 show the results of the calculation including the developed turbulent pipe flow model limiting maximum $\delta_z$ to the port radius. The dashed lines show the axial positions where $\delta_z$ reached the port radius $R$. Let us call these points as "transition points". In the downstream of the transition points, there are the three curves evaluating local regression rates. The dotted curves show the results of the developing

turbulent boundary layer model, and the lower solid curves show the results of the developed turbulent pipe flow model, but the coefficient $\alpha$ is $\alpha_0$ for the developing flat plate boundary layer. The upper curves show the results of the developed turbulent pipe flow model, and the coefficient $\alpha$ is $\alpha_1$ for the developed turbulent pipe flow model. The developed turbulent pipe flow model in $\alpha$=$\alpha_0$ resulted in the higher local regression rates than the developing boundary layer model, but the regression rates were still less than the experimental ones because the coefficient $\alpha$ was not for the developed turbulent pipe flows. Both the two experimental results respectively disagreed with those of the developing boundary layer scheme around the transition points, but were located between the two developed turbulent pipe flow models. Moreover, the experimental results were getting nearer from those in $\alpha = \alpha_0$ to in $\alpha = \alpha_1$ in the downstream of the transition points. This trend suggests that the practical flow fields of SOFTs were on the way to transit from developing boundary layer flows to developed turbulent pipe flows. Therefore, analytical prediction of local regression rates in SOFTs should be evaluated separately in the developing turbulent boundary layer and in the developed turbulent pipe flow region. The idea itself had already been empirically proposed in several researches by Shiraishi et al.[22] because these researchers empirically found that types of functions of the local regression rates are different between the head end and tail end regions in the fuel port though they did not point out the concrete mechanisms. Therefore, our results gave a theoretical background of the separation in the evaluation of the local regression rates from the aspects of the development of boundary layer.

The axial positions of the transition should also be discussed. The larger the geometric swirl numbers were, the nearer the transition point were to the leading edge of the fuel port. This tendency agrees with the increase of practical flow path along with increasing geometric swirl number. Moreover, the results of this analytical prediction gave deeper suggestions to predict regression rates behavior in swirling hybrids. One of them is that the dominant model to determine local or averaged regression rate behaviors in SOFTs can depend not only on oxidizer mass flux but also on geometric swirl number and port aspect ratio because the position of transition points is a function of these parameters. For example, scaled up SOFT engines which operate in the same oxidizer mass flux can have lower regression rates because transition points shifts to downstream and radial flame position can shift farther from the solid fuel surface.

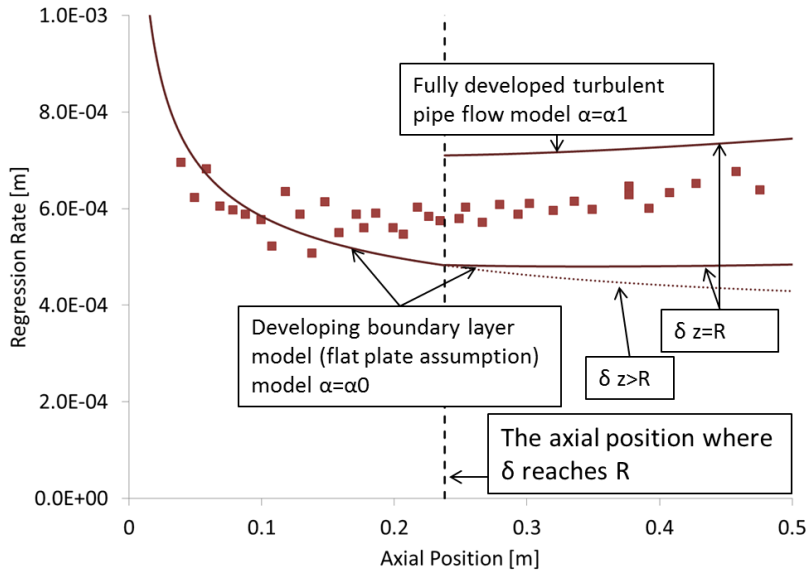


Figure 4.8. Comparison of local regression rates by extended Marxman's diffusion limited analysis using fully developed turbulent flow with the experimental data[23] in $S_g$=9.7. Lower curves are the regression rates of $\alpha = 0.0225$, and upper are of $\alpha = 0.0333$. The curves in downstream are fully developed turbulent flow models.

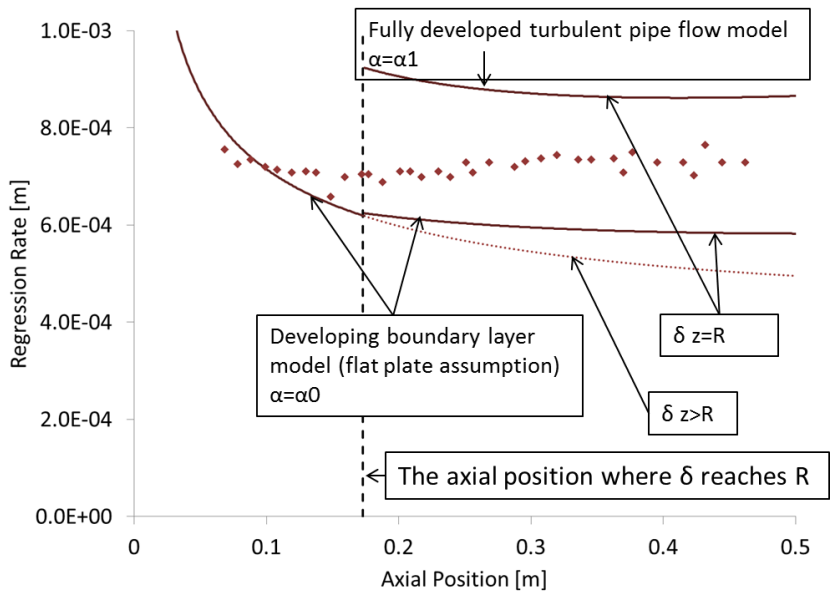


Figure 4.9. Comparison of local regression rates by extended Marxman's diffusion limited analysis using fully developed turbulent flow model with the experimental data[23] in $S_g$=19.4. Lower curves are the regression rates of $\alpha = 0.0225$, and upper are of $\alpha = 0.0333$. The curves in downstream are fully developed turbulent flow models.

## 4.7. Conclusions

In this chapter, analytical evaluations of fuel regression rates in swirling hybrids were developed in order to understand physical phenomena related to the internal flow fields and characteristics of the effects on swirling flow in SOFT hybrid rockets and to predict fuel regression rate in various operational conditions and designs. Our approach was to extend Marxman's diffusion limited analysis for axi-symmetric flows having the circumferential velocity component. Thermal transport phenomena were linked with momentum transfer using the Reynolds' analogy also in turbulent boundary layer of axi-symmetric flows. The newly introduced models were three the dimensional mixing length model, swirl number decay model of main flows assuming one dimensional Euler equation and angular momentum conservation laws. The swirl number decay model was validated with the result of the numerical calculation of combustive flow in SOFTs. The axial component of turbulent shear stress including blowing effects from the solid fuel wall was also modelled. The development of turbulent boundary layer thickness was also evaluated using the Karman's momentum integral under the assumption on pressure gradients. The developed turbulent pipe flow model was newly introduced for the cases where the boundary layer thickness reached the port radius in swirling flows. In this model, the Karman's momentum integral was omitted because this model assumes that turbulent boundary layer has already transited to the fully developed turbulent pipe flow.

The results of our analytical model showed good agreements with those of the experimental results especially in the upstream of the transition points in all the axial and SOFT cases. In the downstream of these points, the experimental results of local regression rates were located between the developed turbulent pipe flow model of $\alpha$ for the developing turbulent boundary layer and that of $\alpha$ for the developed turbulent pipe flow model. These results suggest the existence of the transition start points and the shifts of the flow pattern from the developing boundary layer to the fully developed boundary layer. Moreover, according to the characteristics of our analytical model, the transition of the flow pattern seems to depend on the operating conditions and the design of the fuel grain. For example, our analytical model suggested that the averaged fuel regression rates should decrease in scaled-up SOFTs because the diffusion flames should be located further from the solid fuel wall.

Bibliography of Chapter 4


1 Marxman, G. A., Wooldridge, C. E., and Muzzy, R. J., "Fundamentals of Hybrid Boundary Layer Combustion," *Heterogeneous Combustion Conference*, Palm Beach,FL: AIAA, 1963, p. AIAA 63-505.

2 Marxman, G., and Gilbert, M., "Turbulent Boundary Layer Combustion in the Hybrid Rocket," *Symposium (International) on Combustion*, vol. 9, 1963, pp. 371–383.

3 Marxman, G. A., "Combustion in the Turbulent Boundary Layer on a Vaporizing Surface," *Symposium (International) on Combustion*, vol. 10, 1965, pp. 1337–1346.

4 Marxman, G. A., "Boundary-layer combustion in propulsion," *Symposium (International) on Combustion*, vol. 11, 1967, pp. 269–289.

5 Fox, R. W., Macdonald, A. T., and Pritchard, P. J., *Introduction to Fluid Mechanics*, Wiley, 2003.

6 Chiaverini, M. J., Kuo, K. K., *Fundamentals of Hybrid Rocket Combustion and Propulsion*, AIAA, 2007.

7 Schlichting, H., *Boundary Layer Theory*, McGRAW-HILL, 1979.

8 Dorrance, W. H., and Dore, F. J., "The Effect of Mass Transfer on the Compressible Turbulent Boundary-Layer Skin Friction and Heat Transfer," *Journal of the Aeronautical Sciences*, vol. 21, 1954, pp. 404–410.

9 Taylor, P., Czernuszenko, W., and Rylov, A. A., "A Generalisation of Prandtl's Model for 3D Open Channel Flows," *Journal of Hydraulic Research*, vol. 38, 2000, pp. 37–41.

10 Wang, C.-R., and Papell, S. S., *Three-Dimensional Turbulent Mixing-Length Modeling for Discrete-Hole Coolant Injection into a Crossflow*, 1983.

11 Motoe, M., and Shimada, T., "Numerical Simulations of Combustive Flows in a Swirling-Oxidizer-Flow-Type Hybrid Rocket," *52nd Aerospace Sciences Meeting*, National Harbor, Maryland: AIAA, 2014, p. AIAA 2014-0310.

12 Hatazawa, M., "Characteristics of Turbulent Swirling Flow in a Straight Pipe," *Transaction of JSME, B*, vol. 75, 2009, pp. 1275–1286.

13 Leschziner, M. A., and Hogg, S., "Computation of Highly Swirling Confined Flow with a Reynolds Stress Turbulence Model," *AIAA journal*, vol. 27, 1989, pp. 57–63.

14 Thompson, P. A., and Beavers, G. S., "Compressible-Fluid Dynamics," *Journal of Applied Mechanics*, vol. 39, 1972, p. 366.

15 Gordon, S., and McBride, B. J., *Computer Program for Calculation of Complex Chemical Equilibrium Compositions and Applications*, 1994.

16 Suli, E., Suli, E., Mayers, D., and Mayers, D., *An Introduction to Numerical Analysis*, Cambridge University Press, 2003.

17 Yuasa Saburo, Yamamoto Kengo, Hachiya Hitoshi, Kitagawa Koki, O. Y., "Development of a Small Sounding Hybrid Rocket with a Swirling-Oxidizer-Type Engine," *37th AIAA / ASME / SAE / ASEE Joint Propulsion Conference & Exhibit*, Salt Lake City, UT: AIAA, 2001, p. AIAA 2001-3537.

18 Yuasa, S., Shiraishi, N., and Hirata, K., "Controlling Parameters for Fuel Regression Rate of Swirling-Oxidizer-Flow-Type Hybrid Rocket Engine," *48th AIAA/ASME/SAE/ASEE Joint Propulsion Conference & Exhibit*, Atlanta, GA: AIAA, 2012, p. AIAA 2012-4106.

19 Svehla, R. a., "Estimated Viscosities and Thermal Conductivities of Gases at High Temperatures," *NASA Lewis Research Center Technical Report*, vol. No. R-132, 1962.

20 "NASA Ames Tests Peregrine Hybrid Sounding Rocket Motor," *NASA's Ames Research Center*.

21 Bird, R. B., Stewart, W. E., and Lightfoot, E. N., *Transport Phenomena*, John Wiley & Sons, Inc, 2006.

22 Shiraishi, N., and Yuasa, S., "Prediction Method of Time Variation of Swirling-Oxidizer-Flow-Type Hybrid Rocket Engine Performance Based on Local Fuel Regression Rates," *Journal of the Japan Society for Aeronautical and Space Sciences*, vol. 61, 2013, pp. 71–78.

23 Karabeyoglu, M. A., and Altman, D., "Dynamic Modeling of Hybrid Rocket Combustion," *Journal of Propulsion and Power*, vol. 15, 1999, pp. 562–571.

# Chapter 5

# Static Firing Experiments of a Bread Board Model of Altering-intensity Swirling Oxidizer Flow Type Hybrid Rocket Engines

In this chapter, the concept of A-SOFTs is experimentally demonstrated by static firing experiments. As an O/F elimination technology, A-SOFTs practically should have monotonous dependence of regression rate, O/F ratio and thrust on oxidizer mass flow rates and effective swirl number. In practical use, in addition to this fundamental characteristic, combustion stability, uniqueness and reproducibility of the above three variables are also required. However, as the beginning of experimental investigations of A-SOFTs, the monotonous dependence should be demonstrated by a small bread board model of A-SOFTs (the A-SOFT BBM) prior to the latter three characteristics. In order to demonstrate the monotonous dependence of regression rates on the two operating variables, static firing experiments are carried out in several operating points of oxidizer mass flow rate and effective geometric swirl numbers. In the following sections, after the explanation of the experimental setup and operating conditions, the experimental results are summarized. From these data, the characteristics of the fuel regression rates of the A-SOFT BBM are analyzed. The results are compared with those of SOFTs or the analytical prediction discussed in the prior chapter.

## 5.1. Experimental Setup

In this section, the whole experimental setup including the feed system, the test piece, the control/sensing systems, and the stand system of the A-SOFT BBM are briefly introduced. The whole view of the practical experimental setup is shown in Figure 5.1.

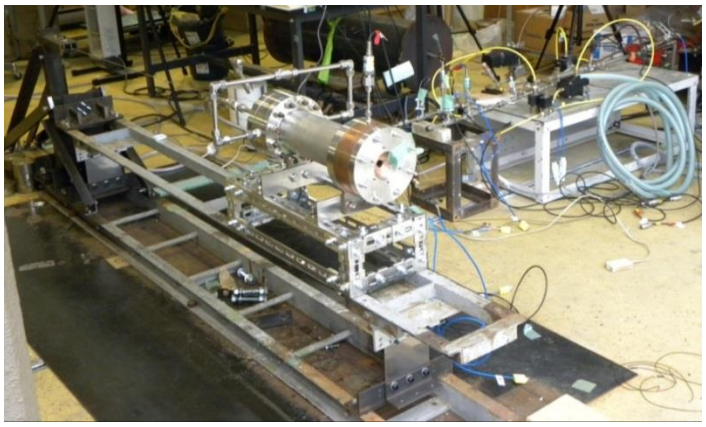

Figure 5.1. Overview of the experimental setup of the A-SOFT BBM.

### 5.1.1. Feed System

The schematic of the feed system is shown in Figure 5.2. In the upstream of the interface with the motor, the oxidizer feed line splits into the two branches. These are the axial and tangential feed lines. The axial-to-tangential oxidizer mass flow ratio is fixed by the chocked orifices during the individual experiments. If the pressure losses between the two branches are negligible, the oxidizer mass flow ratio is determined only by the areal ratio and the efficiency of the two orifices. The total mass flow rate is measured by the turbine flow meter QO1, the pressure transducer PG1 and the thermocouple T1. The rated oxidizer mass flow rate is 78.3[g/s]. The individual mass flow rates in the two branches are also calculated from the characteristics of the choked orifices, the temperature and the pressure at the right upstream of them. Table 5.1 shows the specifications of the choked orifices used in this set of firing experiments. The efficiency of the orifices was calculated from the preliminary tests on the choked orifices before the firing experiments in the Akiruno Research Center of ISAS, JAXA.

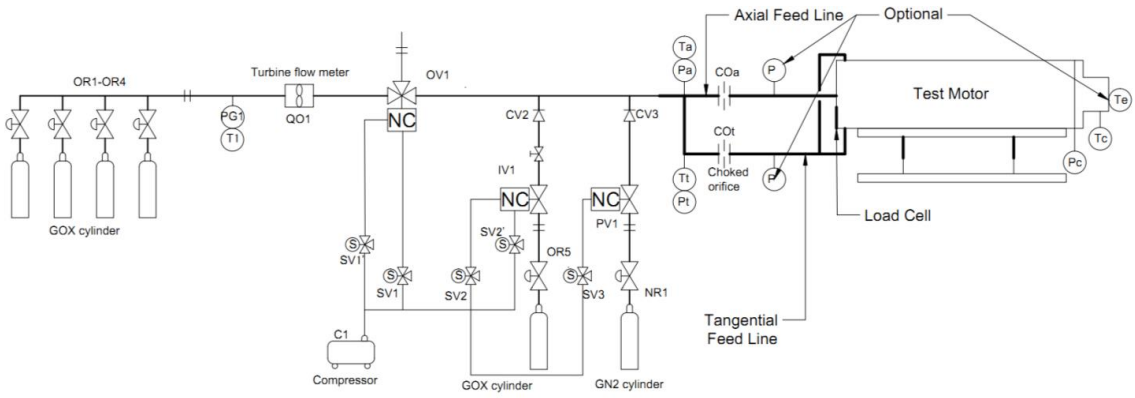


Figure 5.2. Schematic of the feed system and Control & Sensing devices.

Table 5.1. Summary of the choked orifices used in the firing experiments

| Diameter, mm | Discharge Coefficient | Standard Deviation, $10^4$ |
|---|---|---|
| 2.6 | 0.885 | 18.2 |
| 2.4 | 0.872 | 8.30 |
| 2.2 | 0.876 | 9.88 |
| 1.3 | 0.762 | 31.2 |

### 5.1.2. Test Piece

#### 5.1.2.1. Scaling of the Test Piece

One of the most important points in firing experiments of rocket engines is to determine the scaling of engines from the aspect of purposes of experiments. There are the two purposes for this set of the firing experiments. One is to prove the concept of A-SOFTs. This purpose is intended that regression rates of A-SOFTs continuously and stably increase along with both increasing oxidizer mass flux and effective geometric swirl number, which was defined in the section 3.1., and O/F ratio decreases along with the operating variables. Stable operating ranges of oxidizer mass flux as hybrid rocket engines depend on designs of injectors and combustion chambers, but it is said that its order of magnitude ranges between $10^0$ and $10^3$ [kg/m$^2$s]. It is not possible to test over this range using a single design of the engine in this section. Therefore, as the beginning of experimental studies on A-SOFT hybrid rocket engines, our study focuses only on the operational range of the lab-scale SOFT hybrid rocket engines in the previous experiments. According to one of the latest paper on

SOFT hybrid rocket engines[1,2], the operating range of oxidizer mass flux used in the experiments was between 10 and 300 [kg/m²s]. The practical upper limit of geometric swirl number of the tangential injector is about 40. This is because the only practical way to increase geometric swirl number is to decrease injector port area $A_{inj}$ from the definition of the geometric swirl number Eq. (3.1). If too small injector ports are designed, large pressure losses happen. Moreover, oxidizer flows can finally choke in the injector ports, and finally mass flow rates cannot be controlled by controlling devices such as the choked orifices in the upstream of the injectors. From this point of view, the geometric swirl number of 37.3 was selected. The second purpose is to discuss differences of the regression rate behavior between A-SOFTs and SOFTs. That is why the target operating range in this series of experiments is limited more. In the previous experiments of SOFTs, the combination of polypropylene (PP) and gaseous oxygen or polymethyl methacrylate (PMMA) and gaseous oxygen were mainly chosen as the propellants, and the trend of local regression rates along with geometric swirl number were researched especially in the latter combination[3,4]. The operating range of these previous researches was $G_o = 10\sim70$ [kg/m²s] and $S_g = 0\sim19.4$. In the researches using PP and GOX, local regression rate behavior in $S_g = 19.4$ had been researched in detail. The maximum oxidizer mass flux in the researches using PP and GOX was up to 300 [kg/m²s]. In our experiments, PP and GOX were selected as the propellants because of the low material and production costs, and the target operating conditions were in $G_o = 10\sim70$ [kg/m²s].

From the aspects of the scales of the flow fields and the axial position of transition points, it is desirable to carry out experiments in the similar scales of flow fields with the previous experiments of SOFTs. Therefore, it is desired to experiment in the similar scales of $G_o^n, \frac{u_{\theta_e}}{u_{z_e}}, \delta_z \propto Re_L^{-0.2}L$ and $\varphi_\theta\left(\frac{R}{L}\frac{u_{\theta_e}}{u_{z_e}}\frac{G_oR}{\mu}\right)$. The first and second parameters determine the range of regression rates. The third parameter determines boundary layer thickness in the pipe flows[5], and the last one determines radial distribution of circumferential velocity assuming Rankine-like vortex[6]. In order to fit the scales of all the parameters, $R$, $L$, $G_o$ and $u_{\theta_e}/u_{z_e}$ should have the same scale as those in the previous studies. Therefore, the rated oxidizer mass flux and flow rate were set around 60[kg/m²s] and 80[g/s]. The initial port diameter of 40[mm] was chosen. The fuel port should have enough length to include the transition point to developed turbulent pipe flows in the fuel port in order to collect local regression data to validate our theory in Chapter 4. The transition points become the largest in the case of the rated oxidizer mass flux $G_{o_{max}}$ in axial hybrid rocket engines. The expected transition point is evaluated from the relation of Reynolds number and boundary

layer thickness. The estimated transition point in the axial case referred in Chapter 4 was $L = 395$[mm]. Therefore, in the cases of axial injection and the rated oxidizer mass flux cases of 60[kg/m$^2$s], the expected transition point is

$$\left(\frac{60L}{\mu}\right)^{-\frac{1}{5}} L = \left(\frac{70 \cdot 395}{\mu}\right)^{-\frac{1}{5}} 395, L = 380[mm] \qquad (5.1).$$

From this prediction, the solid fuel grain length of 330[mm] was chosen through this set of experiments. The shorter length than the expected value was selected considering the costs to manufacture solid fuel grains. The fuel port length of 330[mm] corresponds to the transition points in $G_{o_{max}}$ ~60[kg/m$^2$s] and $S_g = 2.8$. That is why developing turbulent boundary layer is expected to transit to developed turbulent boundary layer in most of the operational range. The expected O/F ratio at $G_{o_{max}}$ ~60[kg/m$^2$s] and $S_g = 37.3$ is 2.1. This result is in the target range of O/F ratio between 2.0 and 2.5. This range is a typical target range of O/F ratio to maximize specific impulse using propellants of hydrocarbon fuels and oxygen.

5.1.2.2. Summary of the Test Piece

The cross-section of the A-SOFT BBM is shown in Figure 5.3. All the components except for the nozzle are made of SUS304 stainless steel, and the nozzle is made of oxygen free copper. The front flange connected with the injectors is tightened by 12 pieces of M12 bolts, while the rear flange to fix nozzle is tightened by 8 pieces of M8 bolts. The numbers and diameter of the rear bolts were intended to be broken at the designed burst chamber pressure. The axial oxidizer flow is fed from the head of the test piece and the tangential oxidizer flow is fed from the two sides of the dual injector plates. The injector plate between the two flanges has the dual injector consisting of the axial injector element and the tangential injector element. The dual injector can be disassembled into the individual axial and tangential injector elements. Circumferential flow having angular momentum is injected from the 8 slits of the tangential injector ports, and axial flow is injected from the 8 axial injector ports. The maximum effective geometric swirl number is 37.3. The copper nozzle has the pressure transducer port to measure the chamber pressure and the thermocouple port to measure the temperature inside the nozzle. The solid fuel web thickness is designed to be large enough to use high regression rate fuels represented by paraffin wax[7] or low temperature melting fuels[8]. Owing to the enough web thickness, burn time also can be extended for throttling experiments planed in the near future.

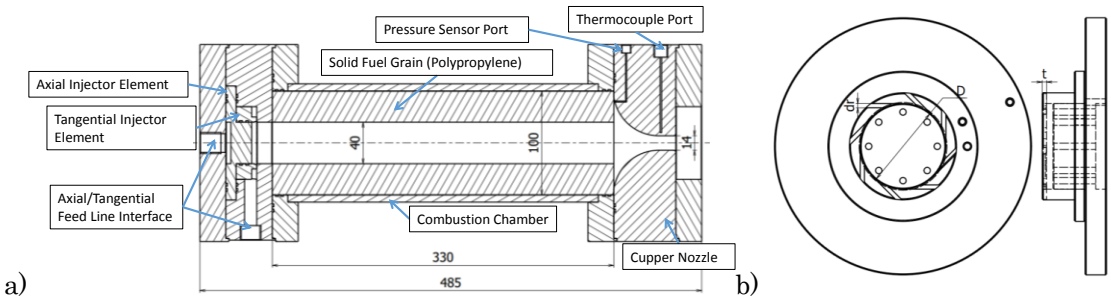


Figure 5.3. a) Cross-section view of the A-SOFT BBM and b) schematics of the dual injector.

### 5.1.3. Control and Sensing Systems

Figure 5.4 shows the sensing system diagram in the apparatus. This system consists of 5 pressure transducers, 5 thermocouples, a load-cell and a turbine flow meter. The measured values are amplified by the amplifiers, converted from analogue to digital data by NI USB-6343 BNC and the converted digital data are recorded in a laptop. The sampling rates of raw data and cooked data using gains and offsets are respectively 1[ms] and 100[ms]. The cooked ones are displayed on the LabView[9] 2013 SP1 and the individual sets of 7 segment displays on the amplifiers.

The control system diagram in the apparatus is shown in Figure 5.5. The programmed relays OMRON 20C1AR-A-V2 and 8E1AR are used to switch the hardware. The safety key switch, the manual switches of the solenoid valves, and the emergency stop button are directly connected to the input ports of the programmed relays and the 4 outputs to control the devices from the NI USB-6343 BNC are also connected to the inputs of the programmed relays through the relay switches. The outputs of the relays are connected to the solenoid valves to control pneumatic valves and the lamps to check on-offs or open-closes of the components.

Gaseous flows are controlled by the valves and the regulators showed in Figure 5.2. The primary pressure of the two sources of GOX, the purge nitrogen gas are manually controlled by the pressure regulators and the needle valves. The GOX flows having the secondary pressures in the downstream of the regulators are controlled by the pneumatic valves from the operation room. The purge valve is a spring-return type, and it is controllable using a single electromagnetic valve. The ignitor is a heating wire connected to the lead storage battery of DC 12 [V] and switched by the programmed relay. The heating

wire is put on the head-end of the fuel port around 120 degree as is shown in Figure 5.6. Total oxidizer mass flow rate is measured by the thermocouple T1, the pressure transducer PG1 and the turbine mass flow meter QO1. The alternative way is the summation of the measured oxidizer mass flow rates at the two choked orifices. The pressure transducers and the thermocouples at the two choked orifices, Ta, Pa, Tt and Pt send the measured data to the laptop and oxidizer mass flow rates of the axial and tangential feed lines are instantly calculated. A pressure transducer is put on the nozzle flange to measure the pressure in the combustion chamber.

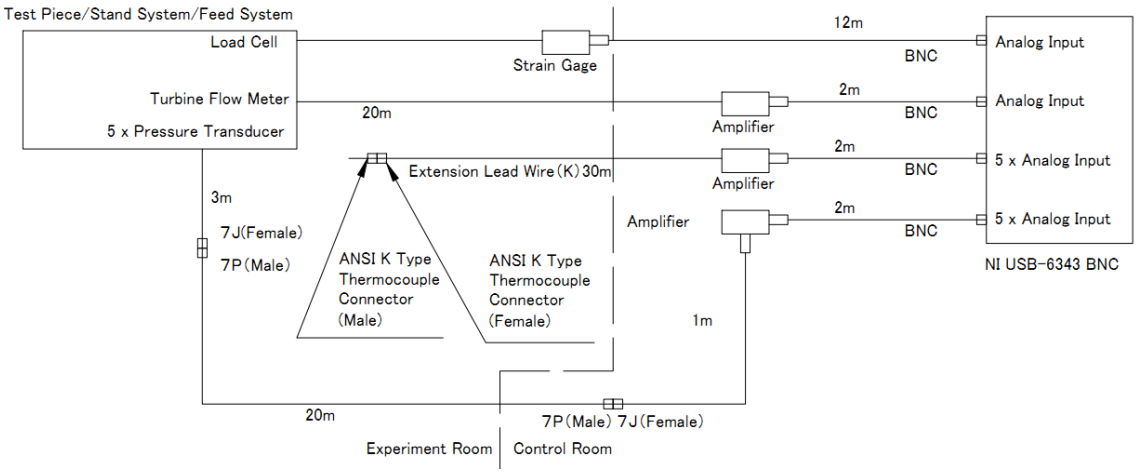


Figure 5.4. Schematic of the sensing system.

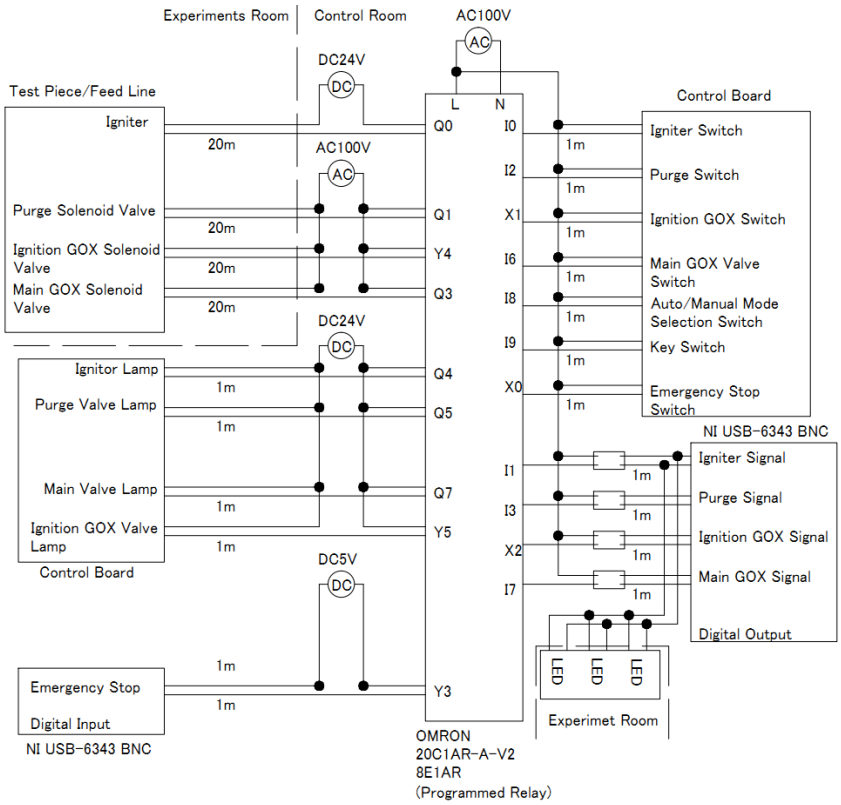


Figure 5.5. Schematic of the control system.

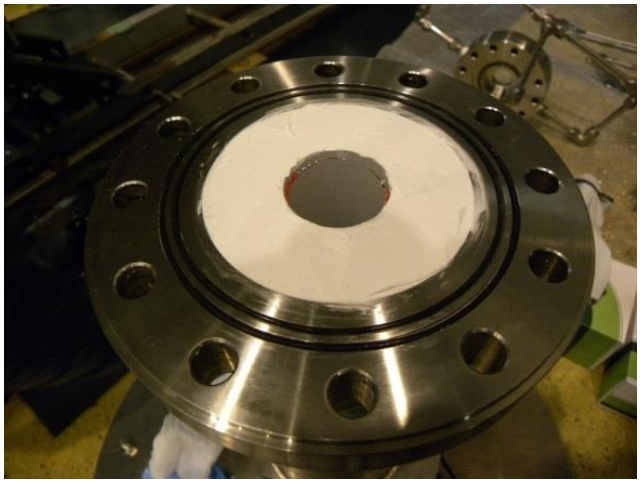

Figure 5.6. Schematic of the setting of the heating wire.

### 5.1.4. Stand System

Most of the components of the stand system shown in Figure 5.7 and Figure 5.8

were mainly provided from Kyushu University. The moving frame of the stand is connected with the base frame with the two pieces of flat springs. When the thrust of the test piece pushes the moving frame of the stand, the load cell is pressed and yields voltage, and this signal is amplified and recorded by the data logger and the laptop. Because the test piece and the stand system are just visually aligned in the yaw direction, the yaw-directional misalignment of ±3 degrees should be taken into account. This error slightly decreases apparent thrust by less than 0.14 %. Because the wires to pull the test piece with the pre-load weight are tied with the bolts to tighten the head-end flange, the wire between the bolts and the pulley is not placed on the center axis of the test piece. This pitch-directional misalignment overestimates the thrust. At most +0.15 degree of misalignment is estimated, and this error gives at most +0.03 % error of thrust. The pulley between the test piece and the pre-load mass are loaded, and the load-cell can lose a few percent of the thrust. These factors decrease the accuracy of the thrust measurement and increase the apparent thrust. The rigidity of the test stand is not evaluated. The less rigidity can also decrease the accuracy of thrust. Deformation of the wire does not affect thrust calibration using pre-load, but decreases the measured thrust pushed by the test piece. In addition to the errors easily evaluated from the specifications of the sensors and amplifiers, these errors difficult to estimate should exist and be taken into account in the measured thrust data.

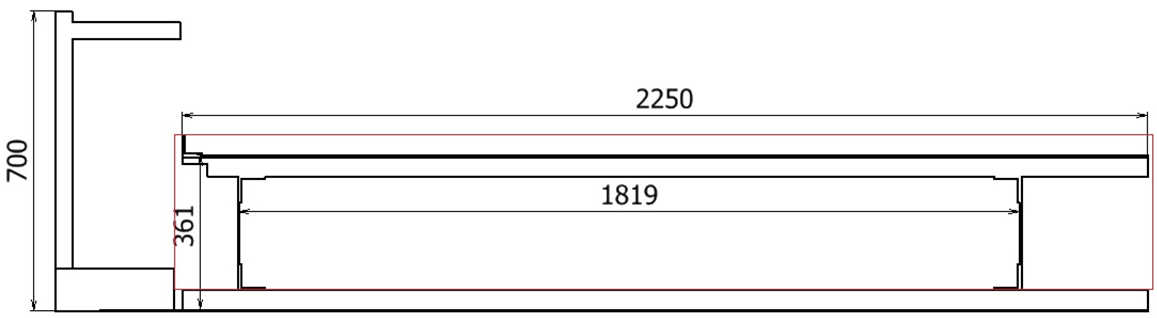


Figure 5.7. Schematics of the main frame of the test stand.

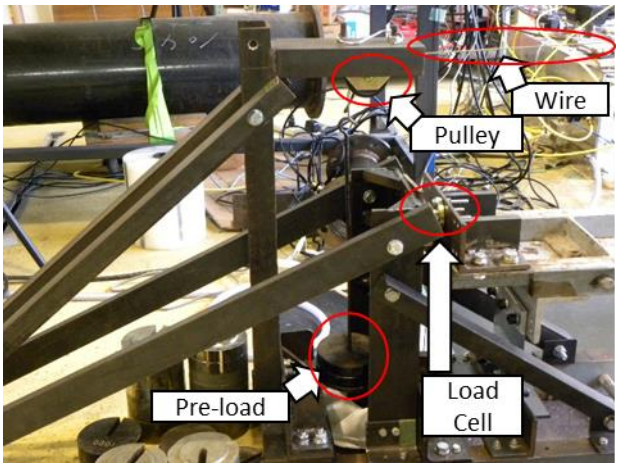


Figure 5.8. Side view of the practical setting around the load cell in the test stand system.

5.1.5. Optical system

Figure 5.9 shows the optical system in the experiments. VTR1, VTR2 and VTR3 respectively record the exhaust gas, overview of the systems placed in the test room, and on-offs of the pneumatic valves. The overview from the VTR2 can be monitored from the control room to check the real time state of the experiments. The 3 pieces of LEDs showing the igniter signals can be seen in all the videos as is shown in Figure 5.10. These lights are used for synchronization of the time between the logged data and the movies with accuracy of 0.033[s].

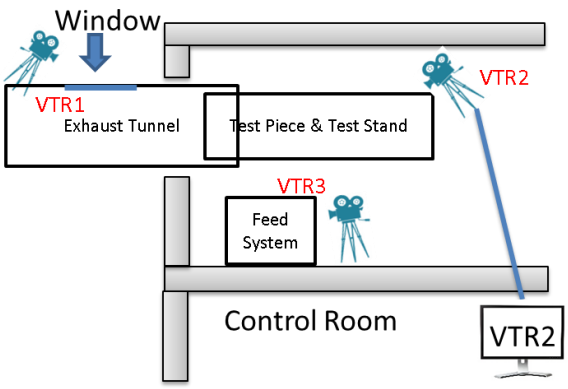


Figure 5.9. Overview of the camera settings.

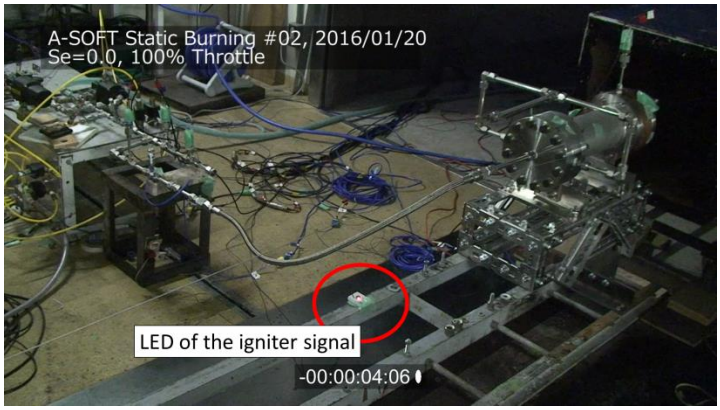


Figure 5.10. Typical view from the VTR2.

## 5.2. Experimental Conditions

### 5.2.1. Operating conditions

The operating conditions in this series of experiments are summarized in Figure 5.11 and Table 5.2 with the selected pairs of the orifices at individual runs. The maximum expected operational pressure (MEOP) in this set of experiments is 1.65 [MPa]. The burn time is 5 [s]. The test piece has a choked nozzle and the maximum expected thrust is 230 [N]. The choked nozzle was used because the nozzle areal ratio of optimal expansion in the lowest chamber pressure in this series is less than 2 and large increases of thrust using divergent nozzles are not expected. The operating conditions are selected from the combination of 3 options of oxidizer mass flow rates and 4 options of effective geometric swirl numbers. The number of options of effective geometric swirl numbers is larger than that of oxidizer mass flow rates because investigating effects of effective geometric swirl number on regression rates are considered to be more important than those of oxidizer mass flux on regression rates, which has been researched by many previous studies[10].

The operating variable designated as “effective geometric swirl number” on Figure 5.11 and Table 5.2 is an extension of “geometric swirl number” used in the field of swirling hybrids for injectors merging axial and swirl flows at injector outlets. This parameter has already been defined in the section 3.1. as

$$S_e = \frac{R_m A_{port}}{R A_{inj}} \frac{1}{\left(1+\dot{m_{o_{ax}}}/\dot{m_{o_{tan}}}\right)^2} = \frac{S_g}{\left(1+\dot{m_{o_{ax}}}/\dot{m_{o_{tan}}}\right)^2} \quad (5.2).$$

The thrust and chamber pressure were predicted by a simple performance prediction program for A-SOFTs. In this program, the axially averaged fuel regression model is adopted as

$$\dot{r}(t) = a_0(1 + S_e(t)^2)^{n_2} G_o(t)^{n_1} \tag{5.3}$$

where the term $(1 + S_e^2)^{n_2}$ refers to the dependence of swirling flow in SOFTs[3]. The constants of this fuel regression model were evaluated from the previous studies[1,3,4]. Because the practical data on the dependence of $S_g$ on regression rates in PP+GOX could not be found, $n_2$ was modelled from the fuel regression data of PMMA+GOX[3,4]. The result of the least square minimization of $(1 + S_e^2)^{n_2}$ is shown in Figure 5.12. The red points were taken from the reference[3] and the green ones were taken from the reference[4]. The blue curve is the curve of the term $(1 + S_e^2)^{n_2}$ approximated with the least square minimization method. Using the evaluation of $n_2$, the other constants were evaluated. After substituting the referential data[1] of $\dot{r}$ and $S_g$ into Eq. (5.3), $n_1$ and $a_0$ are determined by the least square minimization. Besides the performance prediction, the highest local fuel regression rates at the head-end region were also predicted using the empirical prediction model[2] for the safety of the firing experiments.

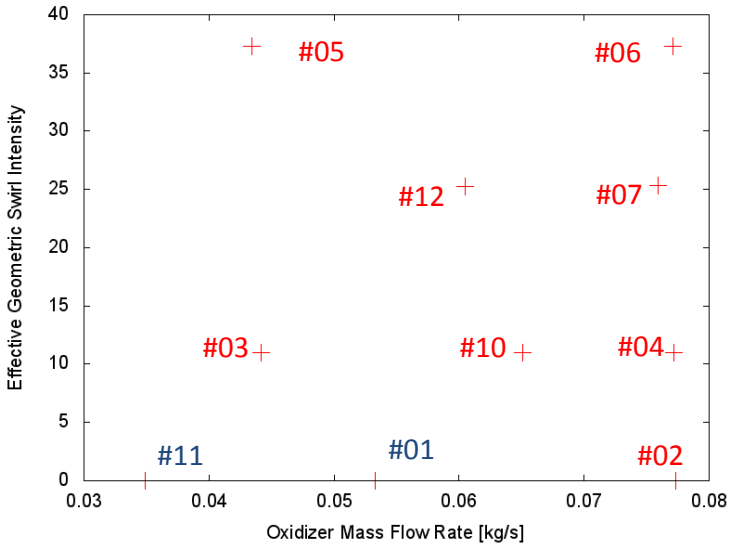


Figure 5.11. Summary of the operating conditions of firing experiments of the A-SOFT BBM.

Table 5.2. Summary of the operating conditions in the static firing experiments of the A-SOFT BBM.

| Run, No. | #01 | #02 | #03 | #04 | #05 | #06 |
|---|---|---|---|---|---|---|
| Target GOX Mass Flow Rate, g/s | 54.8 | 78.3 | 41.9 | 78.3 | 41.9 | 78.3 |
| Target $S_e$ | 0.0 | 0.0 | 11.0 | 11.0 | 37.3 | 37.3 |
| Axial Feed Line Orifice DIA, mm | 2.6 | 2.6 | 2.2 | 2.2 | 0.0 | 0.0 |
| Tangential Feed Line Orifice DIA, mm | 0.0 | 0.0 | 2.4 | 2.4 | 2.6 | 2.6 |
| Expected Thrust, N | 104 | 147 | 106 | 191 | 114 | 226 |
| Expected Chamber Pressure, MPa | 0.6 | 0.9 | 0.6 | 1.1 | 0.7 | 1.3 |
| Burn Time, s | 5.0 | 5.0 | 5.0 | 5.0 | 5.0 | 5.0 |
| Run, No. | #07 | #08 | #09 | #10 | #11 | #12 |
| Target GOX Mass Flow Rate, g/s | 78.3 | 41.9 | 41.9 | 61.1 | 41.9 | 61.1 |
| Target Se | 25.3 | 25.3 | 25.3 | 11.0 | 0.0 | 25.3 |
| Axial Feed Line Orifice DIA, mm | 1.3 | 1.3 | 1.3 | 2.2 | 2.6 | 1.3 |
| Tangential Feed Line Orifice DIA, mm | 2.6 | 2.6 | 2.6 | 2.4 | 0.0 | 2.6 |
| Expected Thrust, N | 214 | 115 | 115 | 152 | 79 | 169 |
| Expected Chamber Pressure, MPa | 1.2 | 0.7 | 0.7 | 0.9 | 0.5 | 1.0 |
| Burn Time, s | 5.0 | 5.0 | 5.0 | 5.0 | 5.0 | 5.0 |

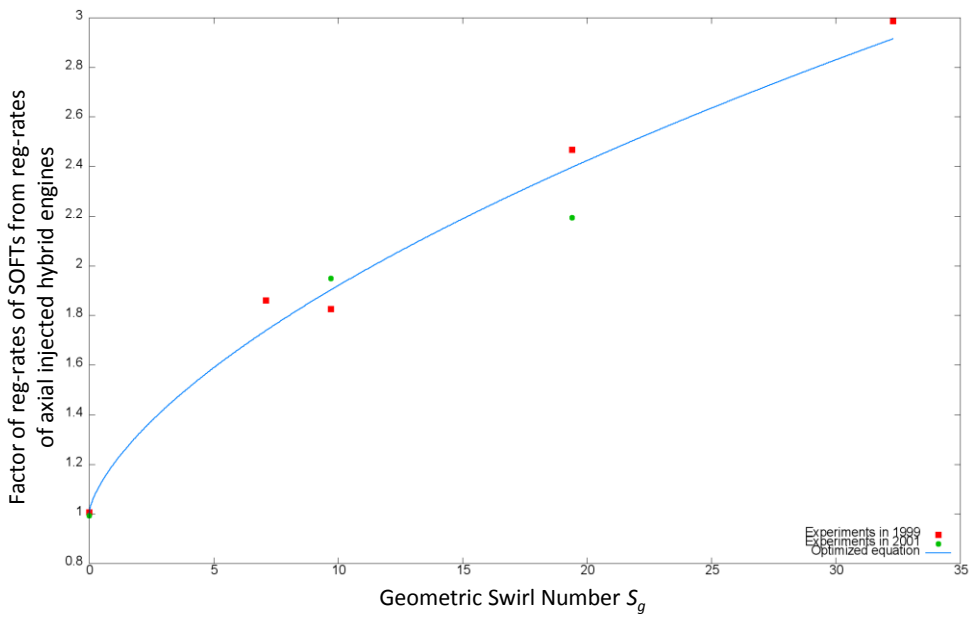


Figure 5.12. Comparison of $a_\xi/a_0$ between the approximation and the previous

experimental data using PMMA+GOX.

### 5.2.2. Time Sequence

Figure 5.13 shows the time sequence of the firing experiments. This figure shows the time sequence of #run02. The upside and downside of each polyline respectively refer to "open and close" or "on and off". Taking the time lags of ignition and the main GOX valve into account, the ignition GOX valve is still open until +0.1[s] and the igniter has still worked until +2.0[s]. The time lag of the main valves is about 0.2[s] from the signals of open and close. In order to open the main valve at 0.0[s], the opening signal turns on at -0.2[s]. The ignition GOX valve and the igniter opened and turned on earlier by 2.0[s] from the run#02 due to the ignition delay in run#01.

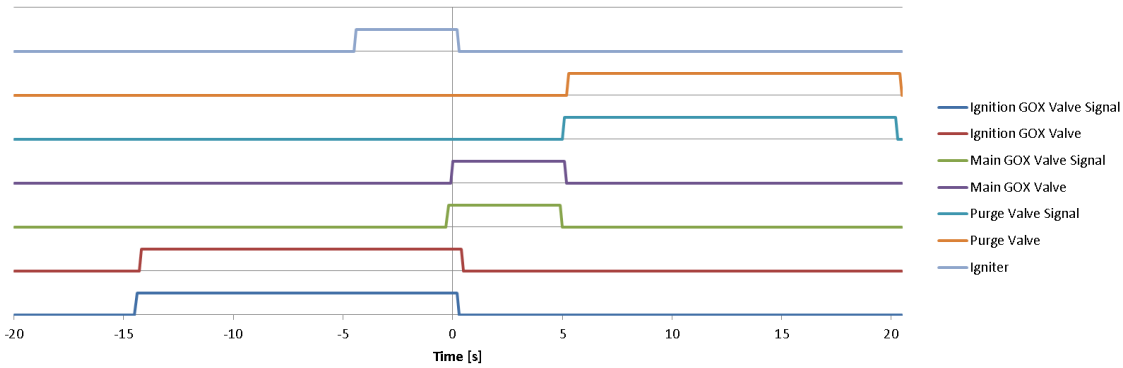


Figure 5.13. Traces of time sequence of the A-SOFT BBM static firing experiments in run#02-#12.

## 5.3. Results and Discussion

### 5.3.1. Overview of the Traces of the Firing experiments

The functional tests and firing experiments had been carried out from Jan. 4, 2016 to Jan. 29, 2016 at Kyushu University. In these tests and experiments, because the malfunction of the turbine flow meter was suspected, total mass flow rates of GOX were evaluated only by the characteristics of the choked orifices, the pressure transducers, and the thermocouples in the upstream of them.

The engine did not reach static burning in several runs. In run#01, the ignition delay occurred due to too short heating time for ignition. This problem was solved by increasing heating time. In run#01 and run#11, though the ignition succeeded, the engine did not reach static burning. Over the series of experiments, heating wire glued at the head-end of the grain is put along 1/3 circumference. Ignition can delay longer in the remained 2/3 circumference of the fuel port can delay only in axial injection cases of run#01 and run#11. In order to decrease ignition delay in axial cases, assistant fuel such as steel wool should be added in the future. In run#08 and run#09, peeling of the igniter and the shortage of battery power caused ignition failure. The other experiments of run#03-#07, run#10 and run#12 ignited and smoothly reached static burning.

Figure 5.14 shows the overviews of the static firing experiments of 100% thrust levels. In run#02, the axial injection case, a lot of droplets of fuel also were seen in the exhaust gas from the nozzle. The larger $S_e$ was, the less the droplets decreased whereas fuel regression rates increased along with $S_e$. These phenomena suggest that c* efficiency of the A-SOFT BBM was improved along increasing $S_e$.

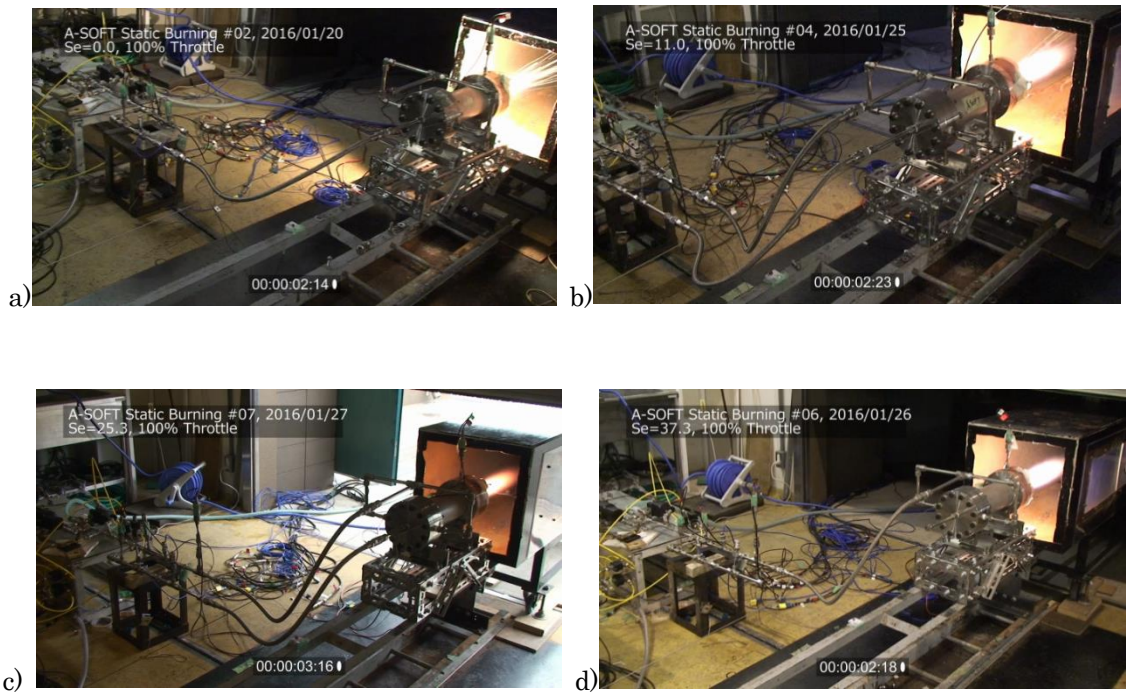


Figure 5.14. Overview of the static firing experiments of the A-SOFT BBM in a) 100% throttle, $S_e$=0), in b) 100% throttle, $S_e$=11.0, in c) 100% throttle, $S_e$=25.3, and in d) 100% throttle, $S_e$=37.3.

Figure 5.15 shows the typical traces of chamber pressure, thrust, oxidizer mass flow rates, and effective geometric swirl number in run#04. In this run, the ignition event started at -4.4 [s] with small flow rates of GOX, and once main GOX flowed at 0.0 [s], the engine smoothly moved onto static burning through the transient state between 0.0[s] and +1.1[s]. The combustion was stable and the increase of chamber pressure followed the increase of total oxidizer mass flow rate.

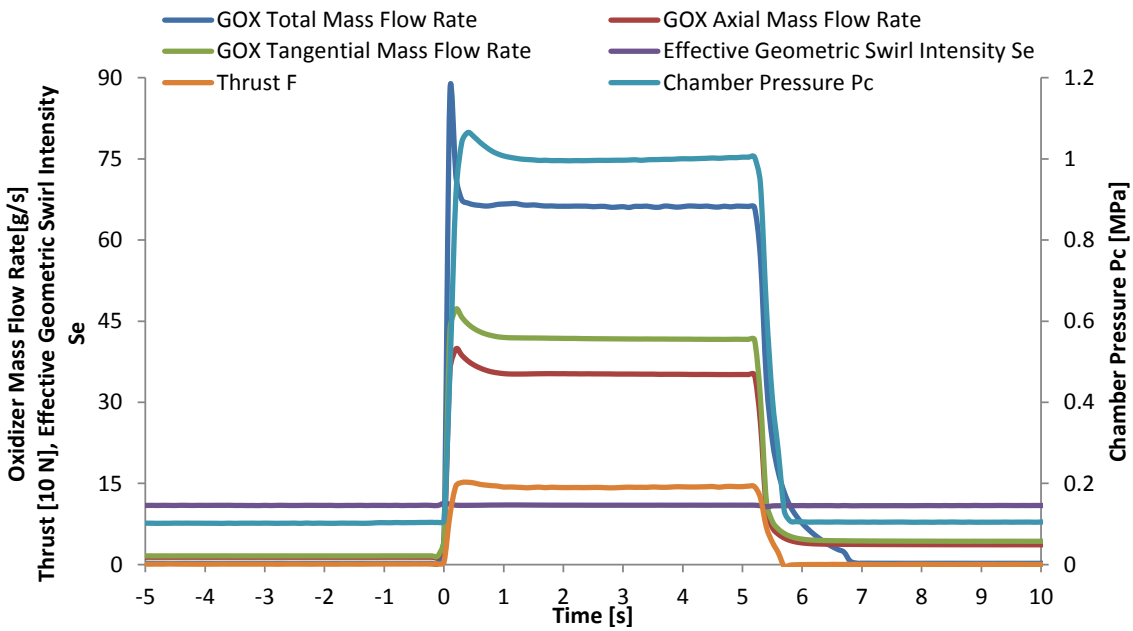


Figure 5.15. Typical traces of the A-SOFT BBM static firing experiments in the case of 100% throttle and $S_e$ =11.0 (run#04).

5.3.2. Fuel Regression Rate Behaviors

The results of the firing experiments are summarized in Table 5.3. The time and axially averaged fuel regression rates were calculated from the fuel grain density and the gross mass of fuel regression using a digital scale, and the diameter after the firing experiments were calculated. The burn time $\Delta t$ was defined as the duration between the time when the chamber pressure rises more than 75% of the peak pressure and the time when the chamber pressure falls below 75% of the peak pressure.

Table 5.3. Summary of the results of the firing experiments of the A-SOFT BBM.

| Run | Init. Conditions of Fuel Grain | | | Inner DIA | | Fuel Mass | | Burn | GOX Mass | $S_e$ |
|---|---|---|---|---|---|---|---|---|---|---|
| No. | Length | Outer DIA | Density | Init. | End | Init. | End | Time | Flow Rate | |
| | mm | mm | kg/m3 | mm | mm | kg | kg | s | g/s | - |
| #01 | 329.65 | 99.79 | 905.9 | 39.95 | 40.75 | 1961.1 | 1945.8 | 1.9 | 53.30 | 0.00 |
| #02 | 329.55 | 99.75 | 904.5 | 40.03 | 43.64 | 1954.4 | 1883.5 | 5.2 | 77.26 | 0.00 |
| #03 | 329.55 | 99.75 | 904.7 | 40.05 | 44.19 | 1954.1 | 1872.4 | 5.2 | 44.18 | 11.00 |
| #04 | 329.60 | 99.75 | 905.5 | 40.04 | 45.54 | 1956.6 | 1846.3 | 5.2 | 77.20 | 10.97 |
| #05 | 329.65 | 99.72 | 904.9 | 40.05 | 44.98 | 1953.8 | 1855.5 | 5.2 | 43.39 | 37.30 |
| #06 | 329.55 | 99.70 | 904.9 | 40.07 | 47.11 | 1952.2 | 1808.4 | 5.2 | 77.12 | 37.30 |
| #07 | 329.65 | 99.75 | 911.1 | 40.06 | 46.49 | 1968.6 | 1837.3 | 5.2 | 75.91 | 25.31 |
| #10 | 329.60 | 99.75 | 905.2 | 40.26 | 45.18 | 1951.8 | 1853.3 | 5.2 | 65.15 | 10.98 |
| #11 | 329.55 | 99.75 | 905.9 | 40.20 | 41.45 | 1954.0 | 1930.1 | 5.2 | 34.87 | 0.00 |
| #12 | 329.50 | 99.75 | 906.4 | 40.03 | 45.53 | 1958.1 | 1847.8 | 5.2 | 60.51 | 25.30 |

| Run | Averaged | O/F | Pressure | | Thrust | | $c^*$ | $I_{sp}$ | $\eta_{c^*}$ | $\eta_{I_{sp}}$ |
|---|---|---|---|---|---|---|---|---|---|---|
| No. | Reg-Rate | | Real | Ideal | Real | Ideal | | | | $/\eta_{C_F}$ |
| | mm/s | - | MPa | MPa | N | N | m/s | s | - | - |
| #01 | 0.21 | 6.62 | 0.51 | 0.57 | 50.1 | 93.3 | 1465.5 | 158.4 | 0.89 | 0.55 |
| #02 | 0.36 | 5.67 | 0.79 | 0.87 | 113.7 | 151.1 | 1515.1 | 172.9 | 0.91 | 0.76 |
| #03 | 0.42 | 2.81 | 0.62 | 0.64 | 87.3 | 107.1 | 1693.5 | 186.3 | 0.96 | 0.82 |
| #04 | 0.56 | 3.64 | 1.00 | 1.02 | 142.7 | 179.6 | 1639.6 | 189.8 | 0.98 | 0.80 |
| #05 | 0.50 | 2.30 | 0.69 | 0.68 | 93.2 | 114.3 | 1717.6 | 190.8 | 1.01 | 0.82 |
| #06 | 0.74 | 2.79 | 1.16 | 1.13 | 166.7 | 200.9 | 1706.9 | 199.3 | 1.02 | 0.83 |
| #07 | 0.67 | 3.01 | 1.03 | 1.08 | 148.4 | 191.2 | 1689.6 | 196.5 | 0.96 | 0.78 |
| #10 | 0.50 | 3.44 | 0.87 | 0.88 | 124.4 | 152.4 | 1651.5 | 188.6 | 1.00 | 0.82 |
| #11 | 0.12 | 7.59 | 0.28 | 0.35 | 31.2 | 52.4 | 1421.3 | 138.7 | 0.79 | 0.65 |
| #12 | 0.56 | 2.85 | 0.84 | 0.88 | 118.8 | 152.2 | 1697.0 | 193.8 | 0.96 | 0.79 |

The time and axially averaged regression rate and axially averaged port radius are respectively calculated by the following equation as

$$\dot{r} = \frac{\sqrt{\frac{m_1 - m_0}{\pi \rho L} + r_0^2} - r_0}{\Delta t} \tag{5.4}$$

$$r_1 = \sqrt{\frac{m_1 - m_0}{\pi \rho L} + r_0^2} \qquad (5.5).$$

From the traces of the firing experiments, the constants of Eq. (5.3) were evaluated by the least-square method. The time integration of Eq. (5.3) is

$$r_1^{2n_1+1} - r_0^{2n_1+1} = (1 + 2n_1)\frac{a_0}{\pi^{n_1}}\int_{t_0}^{t_1}(1 + S_e(t)^2)^{n_2}\dot{m}_o(t)^{n_1}dt \qquad (5.6).$$

This equation includes the effect of expansion of port diameter along with operating time. The right side can be numerically calculated using the records of the firing experiments as

$$r_1^{2n_1+1} - r_0^{2n_1+1} \sim \left(1 + 2n_1\right)\frac{a_0}{\pi^{n_1}}\sum_\tau(1 + S_e(\tau)^2)^{n_2}\dot{m}_o(\tau)^{n_1}\Delta\tau \qquad (5.7).$$

Thus, the residual sum of squares used in least square minimization is

$$\sum_N\left\{r_{1_N}^{2n_1+1} - r_{0_N}^{2n_1+1} - \left(1 + 2n_1\right)\frac{a_0}{\pi^{n_1}}\sum_\tau\left(1 + S_{e_N}(\tau)^2\right)^{n_2}\dot{m}_{o_N}(\tau)^{n_1}\Delta\tau\right\}^2 \qquad (5.8).$$

The approximated constants using the minimization of Eq. (5.9) were $(a_0, n_1, n_2) = (2.557 \times 10^{-5}, 0.6505, 0.0987)$ in SI units. Table 5.4 shows the errors of $r_1$ between the firing experiments and the approximated model. In this evaluation, the errors of fuel regression were calculated as

$$\frac{r_{1_N} - r_{0_N} - a_0\sum_\tau\left(1+S_{e_N}(\tau)^2\right)^{n_2}\left(\frac{\dot{m}_{o_N}(\tau)}{\pi r_N^2(\tau)}\right)^{n_1}\Delta\tau}{r_{1_N} - r_{0_N}} \qquad (5.9).$$

The time and axially averaged regression rates were compared between the experimental results and the approximated model in Figure 5.16. This figure shows that the fuel regression rates have dependence on both oxidizer mass flux and effective geometric swirl number, and Eq. (5.9) fits the fuel regression rates with good accuracy of $\pm 3.5\%$ errors. This result suggests that fuel regression behavior in A-SOFTs is easy to predict. Figure 5.17 shows the surface of Eq. (5.3) and timely and axially averaged regression rates. The surface of Eq. (5.3) is continuous and monotonous along with the two operating variables. These results indicates that A-SOFTs meet the characteristics required for thrust and O/F control, and this is one the purposes of this study. However, experimental results should be added especially in axial injection cases and low effective geometric swirl numbers because just one

of the three experiments succeeded in static burn of axial injection cases, and it is expected that fuel regression rates have strong sensitivity in low swirl numbers.

In Figure 5.18, regression rates of A-SOFTs are compared with those of SOFTs using PP+GOX[1] in various scales of the engine. The geometric swirl number $S_g$ is 19.4 over all the referred data. The grain length vary between 0.15-1.0[m], and the port diameter varies between 40 and 56 [mm]. The two red points show the results of the 5kN class SOFT hybrid rocket motor. Its initial port diameter is 56 [mm] and its port length is 970 [mm]. The regression rates of the A-SOFT BBM in $S_e$ =25.3 and 37.3 were located in the range of regression rates of the SOFTs in $S_g$=19.4 possibly because the fuel regression data of SOFTs include various operating conditions of chamber pressure, grain port scale and burn time. On the other hand, the regression rates of $S_e$=11.0 touched the lower limits of the referential SOFT data and are clearly smaller than them. Therefore, it is difficult to discuss the characteristics of fuel regression rates between the two types in detail just from Figure 5.18.

Table 5.4. Summary of the errors of the approximation from the fuel regression of the firing experiments of the A-SOFT BBM.

| Run No. | Port Diameter mm | Fitting Function mm | Initial Port Diameter mm | Error of Regression % |
|---|---|---|---|---|
| #01 | 40.74 | 40.91 | 39.87 | -25.1 |
| #02 | 43.64 | 43.61 | 40.03 | 0.56 |
| #03 | 44.19 | 44.03 | 40.05 | 3.44 |
| #04 | 45.54 | 45.62 | 40.04 | -1.87 |
| #05 | 44.98 | 44.98 | 40.05 | -0.20 |
| #06 | 47.11 | 47.01 | 40.07 | 1.05 |
| #07 | 46.49 | 46.48 | 40.06 | -0.19 |
| #10 | 45.18 | 45.27 | 40.26 | -2.07 |
| #11 | 41.45 | 42.08 | 40.20 | -58.7 |
| #12 | 45.53 | 45.65 | 40.03 | -2.48 |

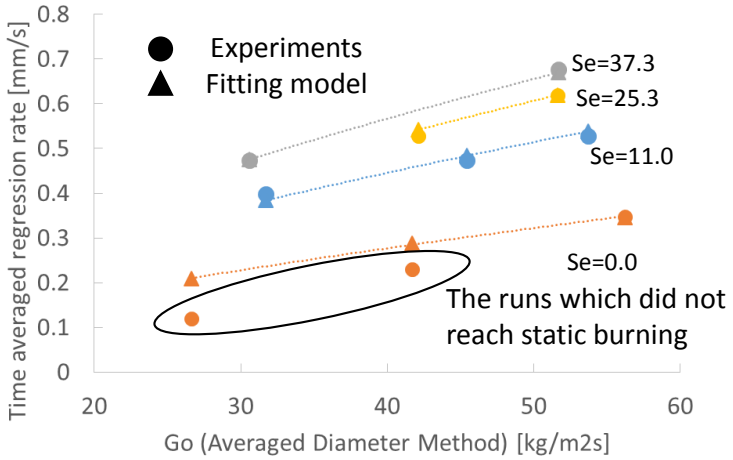


Figure 5.16. Comparison of the time and axially averaged regression rates of the firing experiments of the A-SOFT BBM with the results of the fitting of Eq. (5.3).

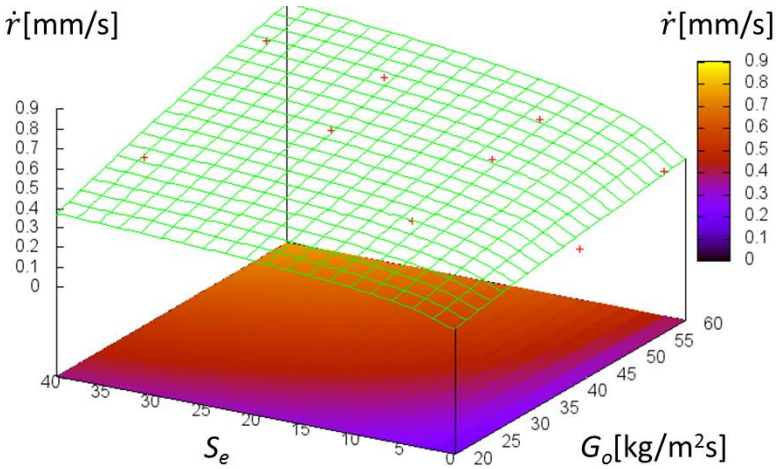


Figure 5.17. Comparison of the approximation of the fuel regression rates with the experimental results of the A-SOFT BBM.

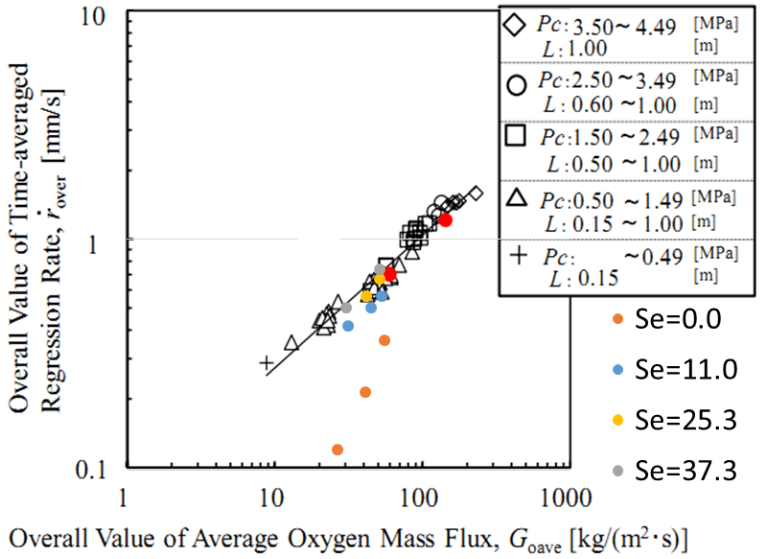


Figure 5.18. Comparison of the fuel regression rates between the A-SOFT BBM and SOFT ($S_g$=19.4).

5.3.3. Local Regression Rate Behavior

The axial distributions of regression rates were measured using the relation between mass and volume of water as is shown in Figure 5.19. The head-end of the fuel grains after the experiments was sealed and vertically put below the laser distance meter (DISTO X310 by Leica). A float (a colored plastic flat plate) was put on the bottom of the grain to reflect the light of the laser distance meter, and the distance between the distance meter and the bottom of the sealed end were measured. After the mass of the water was measured with a digital scale, it was poured into the fuel port, and the distance between the float and the distance meter was measured. From this set of information, mass of the poured water $m$, height filled by the poured water $L$ were acquired. Because the density $\rho$ of the water is a known constant, the averaged port diameter $r$ between the $z = 0$ and $L$ should be

$$r = \sqrt{\frac{m}{\pi \rho L}} \qquad (5.10).$$

From the axial distribution of $r$, the local regression rates were calculated. The measurement error of $r$ due to the measurement hardware is

$$\left(\frac{\sigma_r}{r_0}\right)^2 = \left(\frac{1}{r_0}\frac{\partial r}{\partial L}\Delta L\right)^2 + \left(\frac{1}{r_0}\frac{\partial r}{\partial m}\Delta m\right)^2 \tag{5.11}$$

$$\frac{\sigma_r}{r_0} = \frac{1}{2}\sqrt{\left(\frac{\Delta L}{L_0}\right)^2 + \left(\frac{\Delta m}{m_0}\right)^2} = \frac{1}{2m_0}\sqrt{(\pi r_0^2 \rho \Delta L)^2 + \Delta m^2} \tag{5.12}$$

where $\sigma_r$, $\Delta L$, and $\Delta m$ respectively refer to the expected errors of the port radius and the height and mass of the poured water, and the subscript 0 refers to the referential geometry of the grain to be measured. The scale of the measurement error is inversely proportional to the mass of the poured water. The measurement error of fuel regression rates should be

$$\frac{\sigma_{\dot{r}}}{\dot{r}_0} = \frac{\sigma_r}{\dot{r}_0 \Delta t} \tag{5.13}$$

And the axial distance between the two times of the measurements $L_0$ should be

$$L_0 = \frac{m_0}{\pi r_0^2 \rho} \tag{5.14}$$

The officially announced errors of the digital scale and the laser distance meter are respectively 0.1 [g] and 1[mm]. If the referential grain port radius $r_0 = 22$ [mm] and the referential regression rates of $\dot{r}_0 = 0.4$ [mm/s] are assumed, $\sigma_{\dot{r}}/\dot{r}_0$ and $L_0$ are roughly estimated as is shown in Figure 5.20. From the aspects of both regression rate errors and number of the measurement points, $m_0 = 20\sim30$[g] was chosen. In order to improve the measurement accuracy, the replacement of the laser distance meter should have the largest impact.

Figure 5.21 shows the axial distribution of the fuel regression rates in Run #12 and #07 are compared with those of the SOFTs in the previous study. The local regression at the head-end region became greatly larger along with increasing $S_e$. This large increase of local regression rates should be reflected into designs of fuel grains or thermal designs of the combustion chamber. The error bars due to the measurement errors were also shown in Figure 5.21. In the head-end region, masses of the poured water were large for the local diameter so that the measured values had large error bars. The median values in the head end region were fluctuated possibly because the complex port geometries created by swirling flows helped bubbles in the water stay on the wall of the fuel grain. Because of these fluctuations, the port diameter was measured for several times, and the results of all the trials are shown even if some of them are apart from the next points.

The effective swirl number $S_e$ of these two experiments was 25.3 whereas $S_g$ of the referential data was 19.4. The time averaged oxidizer mass fluxes in Run #12 and #07 were respectively 42.1 and 51.7 [kg/m²s]. In the referential cases of the SOFTs, the fuel regression data of $P_c = 1.16\sim1.18$[MPa] are appropriate to be compared with our data from the aspects of the oxidizer mass flux. Run#12 largely showed the lower regression rates than the SOFTs whereas the local regression rates of run#07 were located in the same range. These gaps between run#12 and the SOFTs are possibly caused by burn time. The oxidizer mass flux in the SOFTs were smaller along with increasing burn time. The relation between the two items of the experimental conditions implies that the initial oxidizer mass flow rates in these 3 cases were near to the same, but the port diameter increased and the time averaged oxidizer mass flux decreased due to the long burn time. Difference of burn time should affect the time averaged fuel regression rates to some degree even if time averaged oxidizer mass flux is the same. In fact, the gap of the regression rates between the referential cases of $G_{oitm} = 67.0$ and $G_{oitm} = 71.9$ reflects this effect. Though the experimental conditions are near to each other except their burn time, the fuel regression rates are different, and the results of $G_{oitm} = 67.0$ is rather nearer to those of $G_{oitm} = 52.4$ and $G_{oitm} = 40.0$. In these cases, possibly, the same initial conditions of oxidizer flow were set except the burn times, and the results were similar to one another though the time averaged oxidizer mass flux changed. Considering this effect of burn time, it is more appropriate to compare the result of run#07 with those of the SOFTs in $P_c = 1.16\sim1.18$[MPa]. The results in run#07 showed the similar axial distribution of regression rates to those of the SOFTs in $S_g = 19.4$. Therefore, at least, the result of this comparison suggests that A-SOFTs have similar distributions of local regression rates to the SOFTs.

Next, the local regression rates in the experiments are compared with those using the prediction model built in the prior chapter. In order to analytically predict the regression rates, the blowing parameter of PP+GOX should be estimated because it could not be found in the previous studies. The thermochemical blowing parameter is expressed with the following equation as

$$B_t = \frac{K_O + \left(\frac{O}{F} + K_O\right)\frac{\Delta h}{h_v}}{\frac{O}{F}\frac{\Delta h}{h_v}} \frac{\Delta h}{h_v} \tag{5.15}$$

where $K_O$ refers to mass fraction of oxidizer at edge of boundary layer, $O/F$ refers to the O/F ratio of the flame, $\Delta h$ refers to the increase of enthalpy of the fuel from the wall to the flame, and $h_v$ refers to the net enthalpy to gasify the solid fuel from the ambient

temperature. If all the gasified fuel are assumed to be propylene, $h_v$ is equivalent to the gap between the formation of enthalpies between propylene at the degradation temperature and PP at ambient temperature. The thermal degradation temperature of PP is 588[K][11], and the enthalpy of formation of PP as ambient temperature is -1969[kJ/kg][12]. The enthalpy of formation of propylene in the range between 200[K] and 6000[K] can be calculated the polynomial database of NASA CEA[13]. From these data, $h_v = 3042$ [kJ/kg] and $\Delta h = 11567$[kJ/kg] are estimated. The stoichiometric O/F ratio of 3.43 is substituted into the term of $O/F$. The estimated blowing parameter resulted in $B_t = 5.20$. This value is in the range of Marxman's estimation[14] that the blowing parameter generally ranges in $5 \leq B_t \leq 100$.

In Figure 5.22, the axial distributions of the regression rates in 100% throttle cases are compared with the results of the prediction model. The black longer curves refer to the regression rate prediction using both of the turbulent boundary layer and the developed pipe flow models using the constant $\alpha = 0.0225$, and the shorter curves refer to those for the fully developed turbulent pipe flows using $\alpha = 0.0333$. These predictions were modelled in Chapter 4. The shapes of the prediction curves fit the experimental results well in all the cases though the axially averaged fuel regression rates sometimes a bit shifted from the results. However, the trends of the transitions to the fully developed turbulent pipe flow model using $\alpha = 0.0333$ were not observed in the A-SOFTs. The results[1] of the SOFTs in Figure 5.21 indicated the increase of the fuel regression rates unique to the fully developed turbulent pipe flow in the tail end region. The continuous decrease of regression rates in A-SOFTs may be affected by the existence of the nozzle. For example, the flame position can be apart from the fuel grain port due to the convergence of the flows near the nozzle. In fact, this indication also can be observed from the results of the SOFTs. In the cases of grain length of 600 [mm], the regression rates started to decrease from 400 [mm] in axial position against the increasing trend between 200 and 400 [mm]. Moreover, Yuasa et al.[15] actually observed the shift of the flame position using the stereoscopy inside the combustion chamber of the SOFTs. In order to precisely study the fuel regression rate behavior in the tail end region, the firing experiments should be carried out without the nozzle or using the longer fuel grain.

Figure 5.23 shows the comparison of the fuel regression rates among the two measurement techniques and the analytical predictions using the constant $\alpha$ of 0.0225. The two measurement method resulted in almost the same values. Most of the analytical predictions also showed good agreement with the two experimental results as the first step of the analytical fuel regression rate prediction of A-SOFTs. However, in some cases, the

predicted fuel regression rates were different from the practical results though the shapes of the curves of the local regression rates are quite similar to the experimental data. The averaged values of these curves a bit shifted from the measured data. The reasons for these shifts are not clear because there are many approximation both in the analytical model and the initial conditions. The improvement of the prediction model should be continued also in the future.

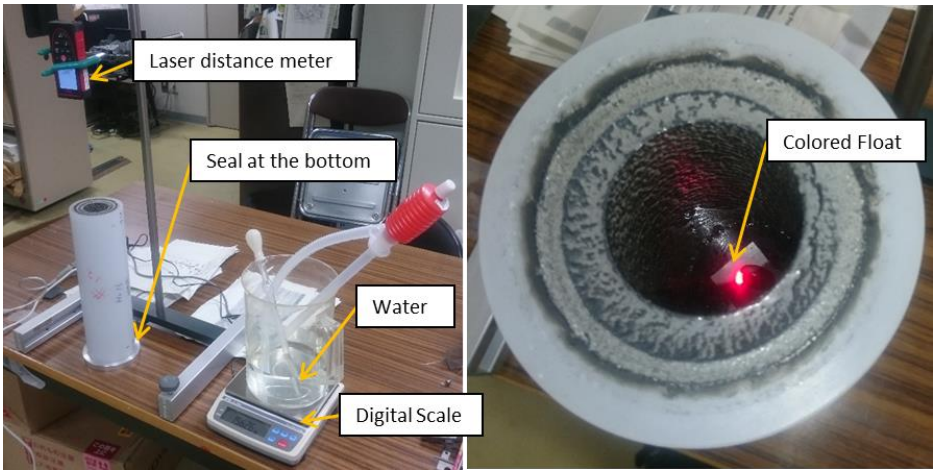


Figure 5.19. Overview of the local regression rate measurement.

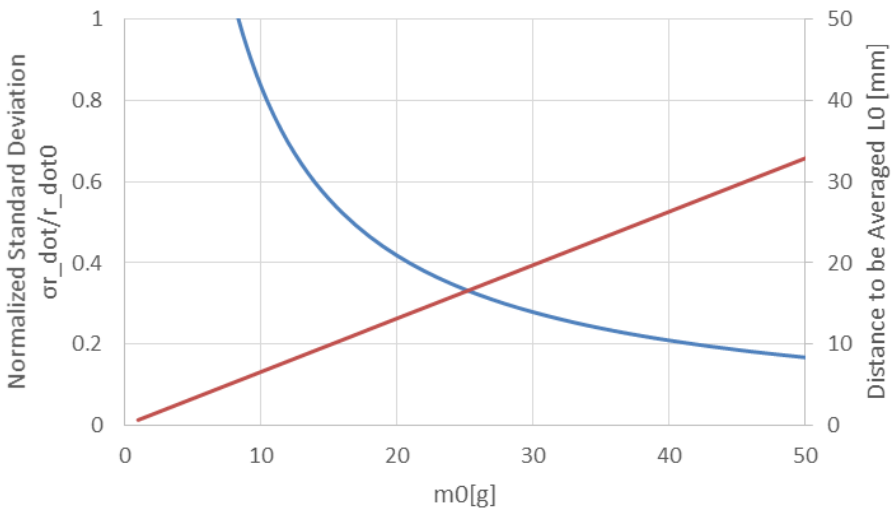


Figure 5.20. Relation between measurement accuracy and resolution of local regression rates.

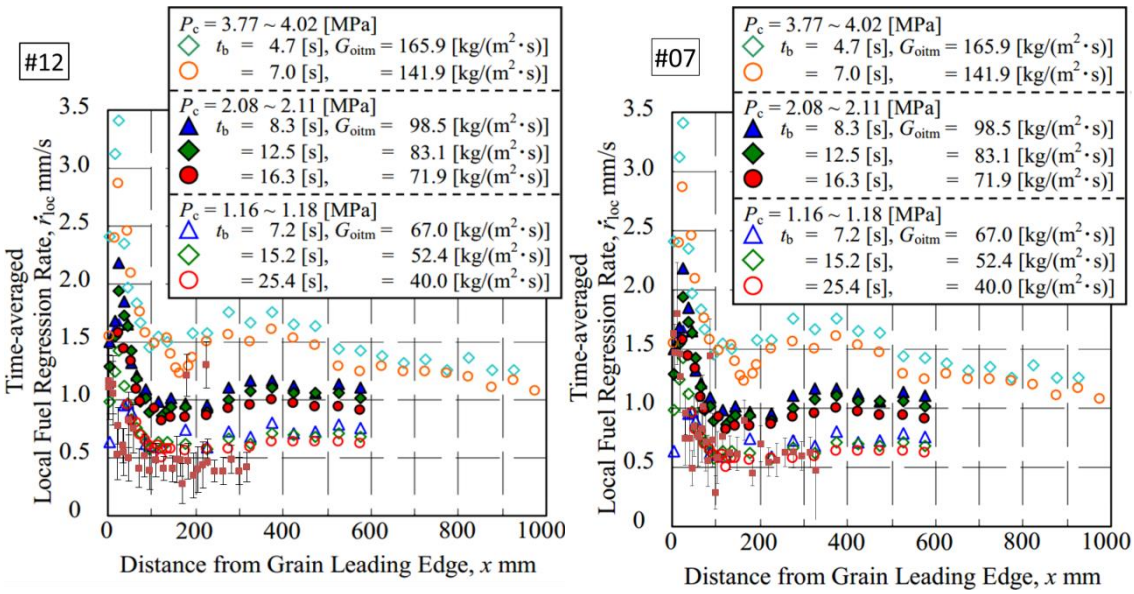


Figure 5.21. Comparison of axial distribution of regression rates between the A-SOFTs and SOFTs[1]

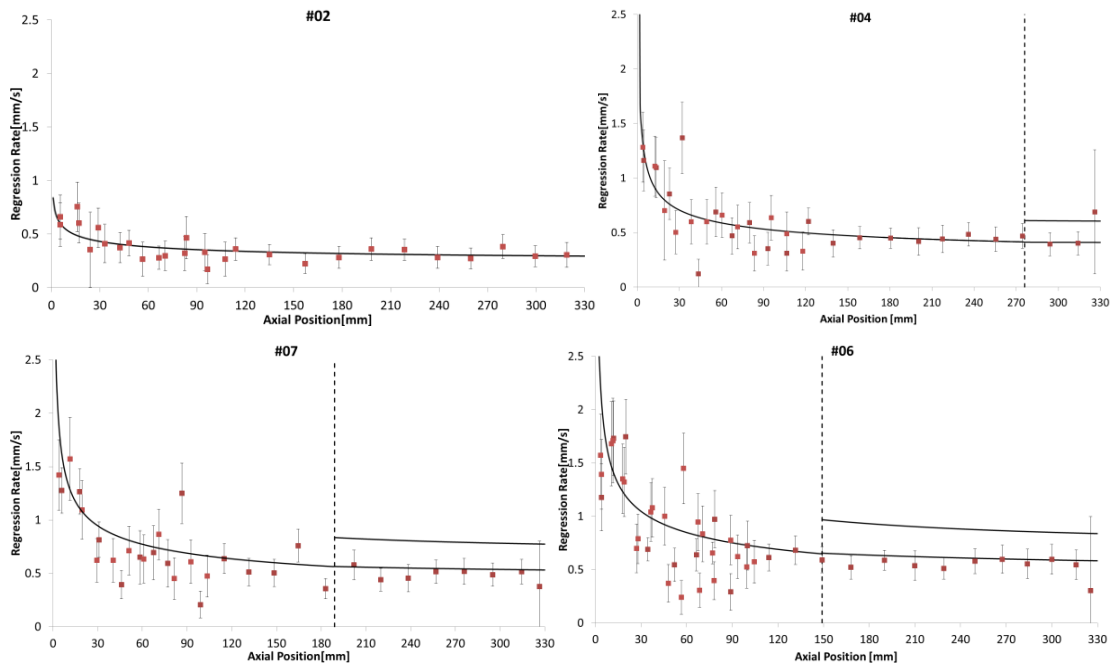


Figure 5.22. Comparison of axial distribution of regression rates between the experimental results and the analytical prediction of A-SOFTs.

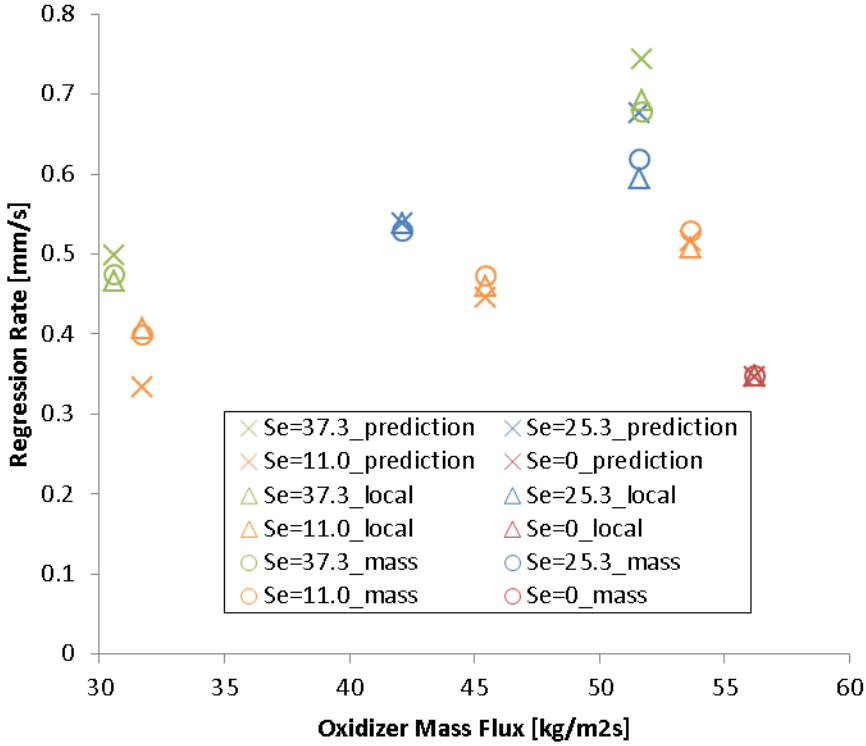


Figure 5.23. Comparison of the time and axially averaged regression rates of the A-SOFTs between from the solid fuel mass measurement, the volumetric measurement and analytical prediction.

5.3.4. Characteristics of O/F ratio and Thrust

Figure 5.24 shows O/F ratios in the 50, 75 and 100% throttle ratios. From the results, O/F ratios monotonously decreased along $S_e$ and increased along with $\dot{m}_o$. The two graphs in Figure 5.25 respectively show the surfaces of O/F ratio and thrust in the firing experiments and their approximations as

$$O/F = \frac{rG_o^{1-n_1}}{2a_0\rho L\{1+S_e^2\}^{n_2}} \tag{5.16}$$

$$F = a_1 + a_2\dot{m}_o + a_3S_e + a_4S_e^2 + a_5\dot{m}_oS_e \tag{5.17}$$

where $r$=21.35[mm] and $L$=329.6[mm] were substituted, and $a_n(n = 1,2,\ldots,5) = (24.7, 1.21 \times 10^3, -3.38 \times 10^{-2}, -1.85 \times 10^{-2}, 25.7)$ in SI units were determined using least square minimization of the thrust data. The red dots refer to the experimental results and the green

surfaces refer to the approximations. The runs where the combustion did not reach static burning were also included in the experimental results. Except for the failed cases, the approximation errors of O/F ratio and thrust were respectively within ±4.2% and ±4.7%.

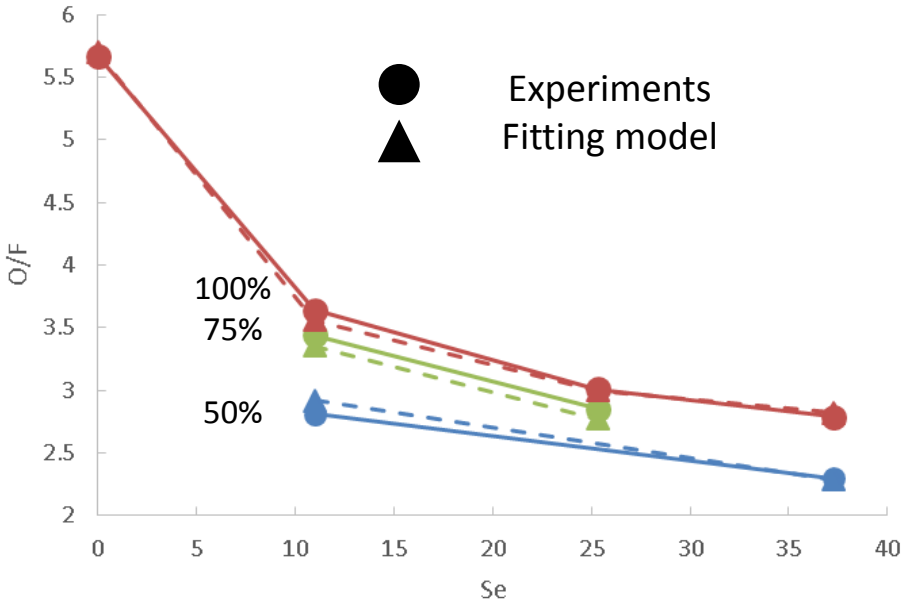


Figure 5.24. Plots of O/F ratio along with $S_e$ in the A-SOFT BBM static firing experiments.

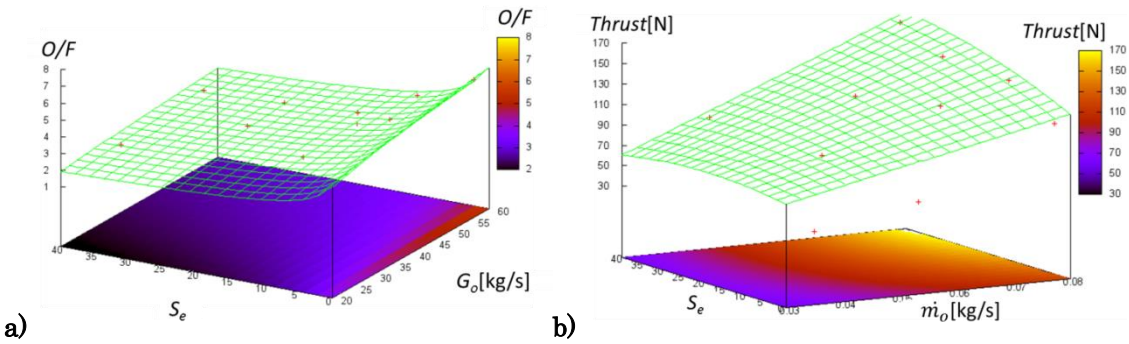


Figure 5.25. Plots of a) the approximation of O/F ratio in the A-SOFT BBM static firing experiments and b) the approximation of thrust in the A-SOFT BBM static firing experiments.

### 5.3.5. Evaluation of c* efficiency

As mentioned in the reference[16], hybrid rocket engines using swirling injection have

pressure differential along with radial direction due to the centrifugal force of the main flows. This pressure differential shifts the measured chamber pressure on the side wall, and sometimes c* efficiency is overestimated. Yuasa et al.[16] proposed that c* efficiency is evaluated indirectly using $I_{sp}$ efficiency and nozzle efficiency. Let us call the conventional method for c* efficiency evaluation using only chamber pressure as "the direct method", and on the other hand, let us call the proposing method using $I_{sp}$ efficiency and nozzle efficiency as "the indirect method". The paper[16] insists that the superiority of the indirect method is explained only in optimal expansion nozzles, but the superiority of the indirect method is not comprehensively investigated for various types of nozzles. In this subsection, after the indirect method is explained, its robustness against the pressure shift is investigated in the usage of the choked nozzle.

From the nozzle theory, the following two equations can be described as

$$\frac{F}{\dot{m}} = I_{sp} g_0 = c^* C_F = \left(\frac{p_c A_t}{\dot{m}}\right) C_F \tag{5.18}$$

$$\eta_{I_{sp}} = \frac{I_{sp}}{I_{sp_i}} = \frac{F/\dot{m}}{F_i/\dot{m}_i} = \frac{c^* C_F}{c_i^* C_{Fi}} = \frac{p_c}{p_{c_i}} \frac{C_F}{C_{Fi}} = \eta_{c^*} \eta_{C_F} \tag{5.19}$$

where $\eta_{c^*}$ refers to the direct method. From Eq. (5.19), c* efficiency can also be indirectly evaluated as $\eta_{I_{sp}}/\eta_{C_F}$. If chamber pressure $p_c$, thrust $F$ and mass flow rate $\dot{m}$ have offset from the true values, the shifts of $\eta_{c^*}$ and $\eta_{I_{sp}}/\eta_{C_F}$ are respectively evaluated as

$$\frac{\Delta\eta_{c^*}}{\eta_{c^*}} = \frac{p_c + \Delta p_c - p_c}{p_{c_i}} \frac{p_{c_i}}{p_c} = \frac{\Delta p_c}{p_c} \equiv \overline{\Delta p_c} \tag{5.20}$$

$$\Delta\left(\frac{\eta_{I_{sp}}}{\eta_{C_F}}\right) / \left(\frac{\eta_{I_{sp}}}{\eta_{C_F}}\right) \sim \left(\frac{\Delta F}{F} - \frac{\Delta\dot{m}}{\dot{m}}\right) + \left(-\frac{1}{\eta_{C_F}} \frac{\partial \eta_{C_F}}{\partial p_c} \Delta p_c\right) = \overline{\Delta F} - \overline{\Delta\dot{m}} - \eta_{c^*} \overline{\Delta p_c} \frac{\partial \ln \eta_{C_F}}{\partial \overline{p_c}} \tag{5.21}$$

where the variables having the symbol Δ refer to offsets from the mean values in combustion chamber. The ideal values ($p_{c_i}, C_{F_i}, F_i$) in Eqs.(5.19) and (5.20) are calculated from the engine performance calculation code mentioned in the subsection 5.2.1., the practical oxidizer mass flow rates, and the practical time averaged fuel regression rate. Therefore, the judgement condition to determine the indirect method has better accuracy is described as

$$\left|\overline{\Delta F}-\overline{\Delta\dot{m}}-\eta_{c^*}\overline{\Delta p_c}\frac{\partial \ln \eta_{C_F}}{\partial \overline{p_c}}\right| = |\overline{\Delta F}-\overline{\Delta\dot{m}}-\overline{\Delta p_c}\varepsilon| < |\overline{\Delta p_c}| \tag{5.22}$$

where the condition $\overline{\Delta F}^2, \overline{\Delta\dot{m}}^2 \ll \overline{\Delta p_c^2}$ is assumed. Because the choked nozzle is used in this engine, in the calculation of $C_F$, the following equation as

$$\frac{p_t}{p_c} = \left(\frac{2}{\gamma+1}\right)^{\frac{\gamma}{(\gamma-1)}} \tag{5.23}$$

can be substituted into $C_F$ as

$$C_F = \sqrt{\frac{2\gamma^2}{\gamma-1}\left(\frac{2}{\gamma+1}\right)^{\frac{(\gamma+1)}{(\gamma-1)}}\left\{1-\left(\frac{p_t}{p_c}\right)^{\frac{(\gamma-1)}{\gamma}}\right\}} + \frac{p_t-p_a}{p_c} = 2\left(\frac{2}{\gamma+1}\right)^{\frac{1}{(\gamma-1)}} - \frac{p_a}{p_c} \tag{5.24}$$

where the exhaust gas is assumed to be choked at the throat. The judgement condition $\varepsilon$ is calculated as

$$\varepsilon(p_{c_i}) = \eta_{c^*}|_{p_{c_i}}\frac{\partial}{\partial \overline{p_c}}\left[\ln\left\{2\left(\frac{2}{\gamma+1}\right)^{\frac{1}{(\gamma-1)}}-\frac{p_a}{p_c}\right\}-\ln\left\{2\left(\frac{2}{\gamma+1}\right)^{\frac{1}{(\gamma-1)}}-\frac{p_a}{p_{c_i}}\right\}\right]\Bigg|_{p_{c_i}} = \frac{1}{2\left(\frac{2}{\gamma+1}\right)^{\frac{1}{(\gamma-1)}}\phi-1} \quad (5.25).$$

Figure 5.26 shows the behaviors of Eq. (5.25) in the range of $1.1 \le \gamma \le 1.4, 5 \le \phi \le 20$, and $\overline{\Delta p_c}$~0.1, which covers the conditions in this set of the firing experiments. Because ε is below 0.2 over this range, the indirect method $\eta_{I_{sp}}/\eta_{C_F}$ theoretically has better accuracy than the direct method $\eta_{c^*}$ and cuts at least 80% of the error due to local pressure shifts.

Secondly, the standard deviations of the performance values used for c* efficiency are evaluated. As mentioned in the subsection 5.1.4., the error caused by yaw and pitch misalignment of the test piece was totally at most 0.15% and negligible. Table 5.5 shows the estimated values of the standard deviations in the individual runs. In these estimations, errors in thrust calibration, errors of efficiency of the choked orifices, errors of the sensors and the amplifiers, errors in measurement of the grain mass and errors of the burn time are included. The standard deviations of $\eta_{c^*}$ and $\eta_{I_{sp}}/\eta_{C_F}$ can be derived with the following propagational laws similar to those used in Eq. (5.20) and Eq. (5.21) as

$$\frac{\sigma_{\eta_{c^*}}}{\eta_{c^*}} = \frac{\sigma_{p_c}}{p_c} \tag{5.26}$$

$$\sigma_{\left(\eta_{I_{sp}}/\eta_{C_F}\right)} = \left(\frac{\eta_{I_{sp}}}{\eta_{C_F}}\right)\sqrt{\left(\frac{\sigma_F}{F}\right)^2 + \left(\frac{\sigma_{\dot{m}}}{\dot{m}}\right)^2 + \left(\eta_{c^*}\frac{\partial \ln \eta_{C_F}}{\partial \overline{p_c}}\right)^2\left(\frac{\sigma_{p_c}}{p_c}\right)^2} \qquad (5.27).$$

Figure 5.27 shows the results of c* efficiency evaluated by the direct method $\eta_{c^*}$ and the indirect method $\eta_{I_{sp}}/\eta_{C_F}$. Note that the error bars only shows the standard deviation of 1 $\sigma$. As expected, Figure 5.27 shows that $\eta_{c^*}$ increased along with $S_e$. This trend seems to be caused by the two main factors. One is the actual improvement of c* efficiency. The tangential flows in swirling injection encourage thermal transfer of combustion heat, mixing and diffusion of fuel and oxidizer. The increasing trend of regression rates along with effective swirl number in Eq. (5.3) also explains the enhancement of transport phenomena in swirling flows. That is why c* efficiency should be improved by swirling injection. This result corresponds to the fuel droplets in the exhaust from the nozzle can be seen in Figure 5.14. The other factor is the apparent improvement of c* efficiency. This apparent improvement of the c* efficiency is caused by the positive pressure gradient along with radial direction driven by the centrifugal force of swirling flows. The positive radial pressure gradient makes the measured values of the pressure transduces on the side wall of the chamber larger than the averaged one. Therefore, the direct method should be directly affected by these two factors. This effect strongly appeared in the results in $S_e$=37.3. In these cases, $\eta_{c^*}$ are larger than 1 and this result contradicts the ideal rocket theory even if the error bars are taken into account. On the other hand, compared to the direct method, the indirect method should be 80% less affected by the pressure shift on the side wall as is shown in Figure 5.26. Figure 5.27 shows that the increasing trend of c* efficiency in the indirect method is smaller than that in the direct method. This result suggests that the indirect method eliminated some of the effects of the local pressure shift due to the centrifugal force. However, all the results using the indirect method took smaller values than those using the direct method even in the case of $S_e$=0.0. The disagreement in the axial case is not covered by the error bars. This contradiction suggests the existence of different sources of the shifts of c* efficiency. The most possible cause is the thrust measurement system. The thrust measurement system has several unevaluated factors on the shifts of thrust as explained in 5.1.4. These factors decrease the measured thrust. Therefore, in order to evaluate c* efficiency using the direct method, the improvement of accuracy of thrust measurement system is desired. The lower c* efficiency in $S_e$=25.3 than other results in $S_e$=11.0 and 37.3 is possibly a practical result but cannot be explained by the low accuracy of the thrust system. This is because this result in the indirect method was clearly seen also in the direct method with the small error bars. These results are probably caused by other factors different from swirling flows such as ideal c* and port volume

because the individual cases in each thrust level have different conditions of total mass flow rate, O/F ratio and port volume during burning. These operating conditions can also affect c* efficiency. These factors should be quantitatively analyzed in more detail in the near future, and reproducibility of this trend should be confirmed in the future firing experiments.

The dominant factors of the large error bars in the indirect method are also the thrust measurement system. Quantitative analyses on individual factors showed that 84% of the errors came from the large gains in the amplifier of the load cell determined in thrust calibration, and 16% of the errors came from the errors of the offset calculated by thrust calibration. Therefore, the effective ways to decrease these large error bars are 1) to decrease amplification factors or gains in thrust calibration as possible and 2) to decrease the error of offset in thrust calibration. From both the aspects of the mean values and the deviations of the indirect method, thrust measurement system should be improved.

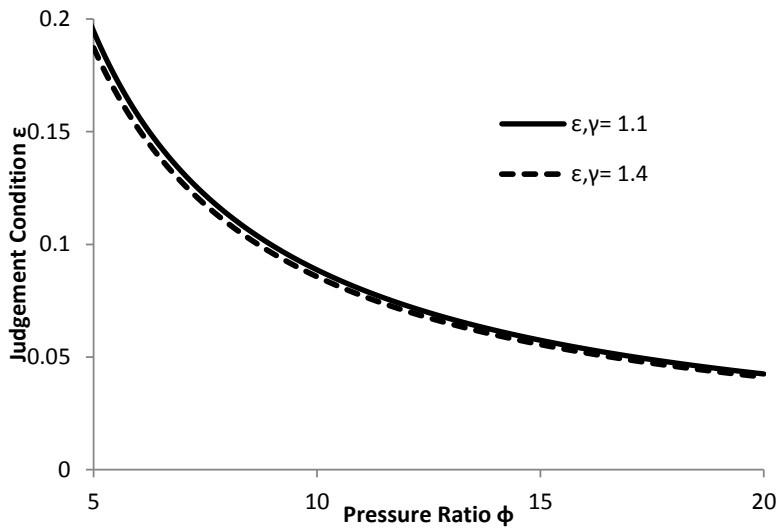


Figure 5.26. Relations between judgement condition ε and chamber pressure ratio $\phi$ in the A-SOFT BBM static firing experiments.

Table 5.5. Summary of the evaluations of the standard deviations of the performance values

| Run | $\sigma_F/F$ | $\sigma_{\dot{m}}/\dot{m}$ | $\sigma_{p_c}/p_c$ | $\sigma_{(\eta_{I_{sp}}/\eta_{c_F})}$ |
|---|---|---|---|---|
| No. | % | % | % | - |
| 01 | 7.72 | 0.54 | 2.32 | 0.0425 |
| 02 | 4.00 | 0.34 | 1.36 | 0.0306 |
| 03 | 3.30 | 0.68 | 1.83 | 0.0277 |
| 04 | 3.28 | 0.43 | 1.04 | 0.0263 |

| | | | | |
|---|---|---|---|---|
| 05 | 5.36 | 0.49 | 1.61 | 0.0439 |
| 06 | 3.00 | 0.36 | 0.89 | 0.0250 |
| 07 | 2.89 | 0.37 | 1.01 | 0.0227 |
| 10 | 3.70 | 0.50 | 1.22 | 0.0305 |
| 11 | 13.26 | 0.47 | 5.25 | 0.0864 |
| 12 | 4.59 | 0.44 | 1.27 | 0.0362 |

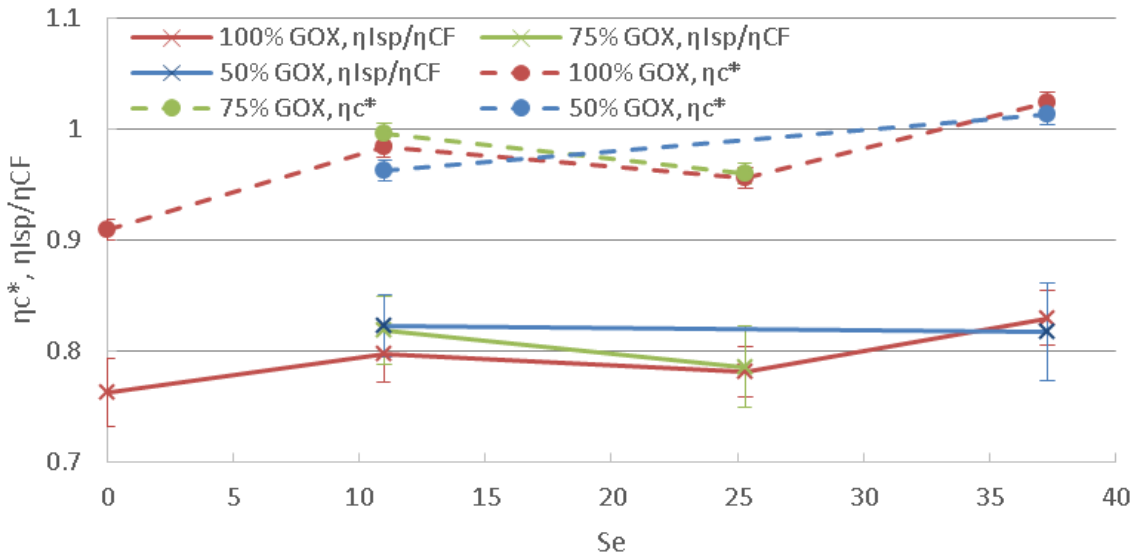


Figure 5.27. Comparison of $\eta_{c^*}$ and $\eta_{I_{sp}}/\eta_{C_F}$ along with $S_e$ in the A-SOFT BBM static firing experiments.

## 5.4. Conclusions

The static firing experiments of a bread board model of A-SOFT hybrid rocket engine (A-SOFT BBM) were carried out using PP and GOX. The results of the performances except the failed runs showed that the A-SOFT BBM has the favorable fuel regression behavior for practical use. The purpose of this set of firing experiments is to confirm the continuity, monotonicity and predictability of the performances of A-SOFTs on oxidizer mass flux and effective geometric swirl number.

The time and axially averaged fuel regression rates fit the model equation proposed in the past studies in SOFT hybrid rocket engines within $\pm 3.5\%$ errors, though more data in axial cases should be acquired in the future because just a case of axial injection succeeded to burn statically. The local regression rates of A-SOFTs were also measured. From the aspect of the measurement accuracy, it is recommended to use more accurate laser

distance diameters. The fuel regression rates were compared with those of SOFTs in $S_g$=19.4. This comparison showed that local fuel regression rates of the A-SOFT BBM in $S_e$=25.3 have similar distributions to those of the SOFTs in $S_g$=19.4. The transition to the fully developed turbulent pipe flows could not be observed probably due to the existence of the nozzle in the near downstream from the transition points. This trend also could be seen in some cases of the SOFTs. In order to validate the transition, firing experiments with longer fuels or without the nozzle should be carried out. The shapes of the prediction curves of regression rates in $\alpha = 0.0225$ agreed with the experimental results, but in the several cases, the predicted regression rates shifted from the measured data. The reasons for these shifts should be considered from the aspects of the settings of the initial conditions, the analytical model itself and other physical phenomena. The O/F ratios and the thrust also respectively fit the model equations within $\pm 4.2\%$ and $\pm 4.7\%$ errors.

c* efficiency was also evaluated using the two methods of 1) the conventional direct method using the real-ideal chamber pressure ratio $\eta_{c^*}$ and 2) the indirect method $\eta_{Isp}/\eta_{C_F}$ to eliminate the effects of local pressure shift caused by centrifugal force of swirling flows. The direct method showed the large increasing trend along with $S_e$, but in strong swirl cases, $\eta_{c^*}$ exceeded 1 because centrifugal force of swirling flows enlarged the local pressure near the side wall. The indirect method was extended for choked nozzles and its better robustness against the local pressure shift was quantitatively validated. This method theoretically decreases at least 80% of the effects of the local pressure shifts in our experimental conditions. The dependence of c* efficiency on $S_e$ was weak in the indirect method, but the result did not agree with the direct method even in the axial injection case where the local pressure should not shift. This result indicates that the source of the gap between the two methods can exist in the thrust measurement system such as frictions of the wire and pulley and loosing or deformations of the wires because these factors decrease the measured thrust and these factors had not been quantitatively evaluated. The decrease of c* efficiency in $S_e$=25.3 was probably caused by the difference of operating conditions such as oxidizer mass flow rate, O/F shift and port diameter. The reproducibility of this local decrease of c* efficiency should be confirmed. The large error bars in the indirect method were mainly due to the errors in the thrust measurement system. The largest factor was the amplified error of the load cell with the large gains. The secondly largest factor was the error of the offset in the thrust calibration. For both the reasons of the mean values and the deviations of the indirect method, the accuracy of the thrust measurement system should be improved.

Bibliography of Chapter 5


1 Yuasa, S., Hirata, K., Sezaki, C., Shiraishi, N., and Sakurai, T., "Fuel Regression Rate Behavior in Swirling-Oxidizer-Flow-Type Hybrid Rocket Engines," *47th AIAA/ASME/SAE/ASEE Joint Propulsion Conference & Exhibit*, San Diego, CA: AIAA, 2011, p. AIAA 2011-5677.

2 Yuasa, S., Shiraishi, N., and Hirata, K., "Controlling Parameters for Fuel Regression Rate of Swirling-Oxidizer-Flow-Type Hybrid Rocket Engine," *48th AIAA/ASME/SAE/ASEE Joint Propulsion Conference & Exhibit*, Atlanta, GA: AIAA, 2012, p. AIAA 2012-4106.

3 Tamura, T., Saburo, Y., and Kengo, Y., "Effects of Swirling Oxidizer Flow on Fuel Regression Rate of Hybrid Rockets," *35th AIAA/ASME/SAE/ASEE Joint Propulsion Conference and Exhibit*, Los Angeles, California: AIAA, 1999, p. AIAA 99-2323.

4 Yuasa Saburo, Yamamoto Kengo, Hachiya Hitoshi, Kitagawa Koki, O. Y., "Development of a Small Sounding Hybrid Rocket with a Swirling-Oxidizer-Type Engine," *37th AIAA / ASME / SAE / ASEE Joint Propulsion Conference & Exhibit*, Salt Lake City, UT: AIAA, 2001, p. AIAA 2001-3537.

5 Schlichting, H., *Boundary Layer Theory*, McGRAW-HILL, 1979.

6 Maicke, B. A., and Majdalani, J., "A Constant Shear Stress Core Flow Model of the Bidirectional Vortex," *Proceedings of the Royal Society A: Mathematical, Physical and Engineering Sciences*, vol. 465, 2009, pp. 915–935.

7 Karabeyoglu, A., Zilliac, G., Cantwell, B. J., DeZilwa, S., and Castellucci, P., "Scale-Up Tests of High Regression Rate Paraffin-Based Hybrid Rocket Fuels," *Journal of Propulsion and Power*, vol. 20, 2004, pp. 1037–1045.

8 Wada, Y., Kato, R., Kato, N., and Hori, K., "Small Rocket Launch Experiment using Low Melting Point Thermoplastic Fuel/N2O Hybrid Rocket," *49th AIAA/ASME/SAE/ASEE Joint Propulsion Conference*, San Jose, CA: AIAA, 2013, p. AIAA 2013-4050.

9 Blume, P. A., *The Labview Style Book*, Prentice Hall, 2007.

10 Chiaverini, M. J., Kuo, K. K., *Fundamentals of Hybrid Rocket Combustion and Propulsion*, AIAA, 2007.

11 Cullis, C. F., and Hirschler, M. M., "The significance of Thermoanalytical Measurements in the Assessment of Polymer Flammability," *Polymer*, vol. 24, 1983, pp. 834–840.

12 "Heats of Formation and Chemical Composition," *Purdue School of Aeronautics and Astronautics* Available:

https://engineering.purdue.edu/~propulsi/propulsion/comb/propellants.html.

13 Gordon, S., and McBride, B. J., *Computer Program for Calculation of Complex Chemical Equilibrium Compositions and Applications*, 1994.

14 Marxman, G. A., Wooldridge, C. E., and Muzzy, R. J., "Fundamentals of Hybrid Boundary Layer Combustion," *Heterogeneous Combustion Conference*, Palm Beach,FL: AIAA, 1963, p. AIAA 63-505.

15 Saito, D., Yuasa, S., and Sakurai, T., "Three Dimensional Visualization of Flames in Combustion Chamber of Swirling-Oxidizer-Flow-Type Hybrid Rocket Engine," *Proceedings of the 53rd Conference on Aerospace Propulsion and Power*, Kurashiki, Okayama, Japan: JSASS, 2013, p. JSASS-2013-0025.

16 Yuasa, S., Shiraishi, N., Sakamoto, M., Sezaki, C., Hirata, K., and Sakurai, T., "Evaluation Method of C* Efficiency of Swirling-Oxidizer-Flow-Type Hybrid Rocket Engines," *Journal of the Japan Socienty for Aeronautical and Space Sciences*, vol. 59, 2011, pp. 97–101.

# Chapter 6

# Conclusions and Future Work

In this thesis, the four topics related to O/F shifts of hybrid rocket propulsion and O/F elimination technologies were studied. In Chapter 2, the impact of O/F shifts in hybrid rocket propulsion on the flight performances of sounding rockets were evaluated. In Chapter 3, the concept of A-SOFT was proposed as a new O/F shift elimination technology, and its characteristics were compared with those of the existing ideas. In Chapter 4, the analytical evaluation of fuel regression rates for axially injected hybrids was extended to that for SOFTs and A-SOFTs. In Chapter 5, the concept of A-SOFT was experimentally demonstrated by static firing experiments. The important findings on the individual topics will be summarized in the following sections and the future work are discussed in the last subsection.

## 6.1. Evaluations of impacts of O/F shifts

Although O/F shifts were known as a unique phenomenon in hybrid rocket propulsion, most of the studies focused only on the O/F shifts caused by nominal fuel regression rate behaviors as the source of O/F shifts and the enthalpy shifts as the main impact of O/F shifts on flight performances. However, we believed that this hypothesis is not always correct, and several sources of O/F shifts and several phenomena affected by O/F shifts and having impacts on flight performances were pointed out and modelled. Assuming the similar scale and conceptual design to the S-520 series, the flight performances of vertically launched sounding rockets were simulated. Analyzing the results, the importance of each source of O/F shifts and the impacts of O/F shifts on the performances were evaluated.

The flight simulations were divided into the three sets. The first set of simulations was aimed to evaluate the impacts of the O/F shifts caused by the nominal fuel regression rates. This set of simulations revealed that the enthalpy shift of the productive gas in deep throttling is the dominant phenomenon to decrease the performance, and the other phenomena such as c* efficiency and erosion of the nozzle throat hardly depends on O/F

shifts. The loss of the highest altitude in the O/F uncontrolled case was by 2.2% of the highest altitude in the O/F controlled case. The second set was aimed to evaluate the effects of O/F shifts also caused by the systematic errors of fuel regression behaviors. Under the assumptions of the systematic errors of regression rates, in addition to the enthalpy shift, residual mass of propellants also decreased the flight performances. The O/F uncontrolled case lost 10% of the highest altitude in +3σ of the modelled systematic error. The conceptual O/F shift elimination technology system perfectly prevented the expected performance losses using the ideal feedback system.

The purpose of the last set was to evaluate the effects of O/F shifts caused by the random errors of fuel regression behaviors. The errors were added using the pseudorandom numbers subject to the normal distribution with the scale of the prediction interval. The flight simulations were repeated for 3000 times. Also in this sets of simulations, the O/F controlled cases succeeded to eliminate most of the residual propellants and the performance losses from the nominal performances but the O/F uncontrolled system lost the flight performances due to the random O/F shift. The residual mass, specific impulse and the highest altitudes in the O/F uncontrolled cases widely ranged though the O/F uncontrolled cases maintained good performances. This is because the variance of the fuel regression random errors directly affects their flight performances. The guaranteed highest altitude with 99.73% probability in the O/F controlled case was 2.9% higher than the one of the O/F uncontrolled case.

This series of the flight simulations clarified that O/F control system in hybrid propulsion prevent at most 10 % of the flight performance losses even for the single purpose use in vertically launched hybrid sounding rockets.

### 6.2. Trade-offs of the O/F control technologies

Following the evaluation of the impact of O/F shifts, the concept of new O/F control system designated A-SOFT was explained, and throttle range and other qualitative trade-offs were compared with existing O/F control systems previously proposed. This chapter clarified that A-SOFTs practically do not have restriction on their throttle ranges under the appropriate designs of the solid fuel grain and qualitatively have the favorable characteristics in the most point of views. The qualitative advantages of A-SOFTs are the

stable fuel regression and combustion, higher c* efficiency, large baseline regression rates and high structural efficiency. The practical disadvantages are the increase of complexity of additional components of LOX vaporization systems and the cost for burn tests in R&Ds in the two dimensional operational variables. However, these disadvantages will be compensated by analytical or numerical researches.

## 6.3. Analytical Prediction of Swirling Oxidizer Flow Type Hybrid Rocket Engines

In Chapter 4, analytical prediction of fuel regression rates in SOFTs were developed in order to phenomenologically understand the mechanism of the enhancement of fuel regression rates and to easily predict the fuel regression rates in SOFT hybrid rockets.

Our approach was to extend Marxman's diffusion limited analysis for axi-symmetric pipe flows having circumferential velocity component. The representative newly introduced models were the three dimensional mixing length model and the swirl number decay model of main flows based on one dimensional Euler equation and angular momentum conservation laws.

The results of our analytical model suggested the existence of the transition start points from the turbulent boundary layer to the turbulent pipe flows in the middle of the fuel port. The results of our analytical model in the downstream of these points implied that the boundary layer transits to the turbulent pipe flows. The predicted regression rates in the upstream of the transition points showed good agreements with the experimental data of regression rates, and in the downstream of these points, the experimental results were located between the turbulent boundary layer model and the developed turbulent pipe flow model. The transition start points depended on operational conditions such as oxidizer mass flux and geometric swirl number. The transition of turbulent boundary layer should depend also on the geometry of the solid fuel port because the maximum boundary layer thickness and its axial position depend on the port diameter.

## 6.4. Conceptual Demonstration of Altering-intensity Swirling Oxidizer Flow Type Hybrid Rocket Engines

The concept of A-SOFTs was empirically demonstrated by the static firing

experiments. As the beginning of the experimental investigation of A-SOFTs, the firing experiments were practically aimed to show that A-SOFTs have monotonous dependence of regression rate, O/F ratio and thrust on oxidizer mass flux and effective swirl number. In order to show monotonous dependence of regression rates on relative strength of oxidizer swirl, static firing experiments were successfully carried out in 8 operational points of oxidizer mass flow rate and relative swirl strength.

The bread board model of A-SOFT hybrid rocket engine using PP and GOX showed the stable burns and showed the favorable fuel regression behavior. After the experiments, time and axially averaged fuel regression rates were measured from weight losses of the solid fuel grains and axial distributions of regression rates were measured using water. The axially and timely averaged fuel regression fit the function system proposed in the past studies for SOFTs within ±3.5% errors. The axial distribution of the regression rates of A-SOFTs were compared with that of SOFTs. The axial distribution of the fuel regression rates of A-SOFTs in $S_e$=25.3was similar to those of SOFTs in $S_g$=19.4. However, the transition to the fully developed turbulent pipe flows was not observed possibly due to the existence of the nozzle in the near downstream from the transition points. The axial distribution of the regression rates of A-SOFTs were compared also with the results of the prediction method modelled in Chapter 4. The prediction curves with α=0.0225 agreed with the experimental results as the beginning of the analytical prediction of regression rates in A-SOFTs. The O/F ratios and the thrust also respectively fit the model equations within ±4.2% and ±4.7% errors. Therefore, eventually the purpose of the static firing experiments were accomplished.

Apart from the initial purpose, the efforts to improve accuracy of c* efficiency were also carried out. This is because the conventional direct measurement method using the real-ideal chamber pressure ratio has a problem on the existence of local pressure shifts due to centrifugal force of swirling flows. The indirect method using Isp efficiency and nozzle efficiency was proposed to eliminate the effects of local pressure shift caused by centrifugal force of swirling flows. In the practical analyses, the direct method showed the large increasing trend of the calculated c* efficiency along with $S_e$. On the other hand, that trend in the indirect method became smaller, but the two results did not agree even in the axial injection cases. This result indicates that the sources causing shifts of c* efficiency was suspected to exist in the thrust measurement system. The sources can be frictions of the

wire and pulley and loosing or deformations of the wires because these factors decrease the measured thrust and their reliability had not been evaluated. The low accuracy in the indirect method were dominated by the large errors in the thrust measurement system. From both of the aspects of shifts of median values and the scale of error bars, in order to acquire reliable results of c* efficiency, the accuracy of the thrust measurement system should be improved.

Though the static firing experiments succeeded to show the monotonous dependence of regression rates on operational variables of A-SOFTs, this is just the start point of the demonstration of the concept of A-SOFT. This character should be demonstrated also in the throttling cases. Moreover, uniqueness and reproducibility of the fuel regression rate behavior also should be proven. From the aspect of practical use, continuous throttling using flow control valves and the whole system including oxidizer vaporization system and feedback system using regression rate measurement systems also should be demonstrated.

## 6.5. Future Work

There is much work to carry out a flight demonstration of hybrid rocket propulsion in the future. In this subsection, academic research topics related to this thesis and remained challenges to realize A-SOFT as a propulsion system are discussed.

One of our future work is to improve and extend the flight simulation. The most necessary point to be improved in the engine model is the c* efficiency model. This model should be replaced by new one based on diffusion of propellants, and enhancement of c* efficiency due to swirling flow should be modelled. In the practical evaluations of the flight performances, we specified the mission, the propellants and the scale of rockets. In order to comprehensively discuss effects of O/F shifts in cases of many kinds of propellants and scales of rockets, flight performance of many types of hybrid rockets should be evaluated. Our engine model created in Chapter 2 is also applicable to evaluate expectancy and accuracy of orbit injection using flight simulations for launching rockets. After calculating conceptual design of optimal multi-stage launching rockets and developing a flight simulation code, improvement of the performances due to O/F shift elimination technologies can be evaluated.

Secondly, in Chapter 3, limitations of throttle ranges using O/F shifts elimination technologies can be discussed more deeply from the aspects of the practical limitations of geometric swirl number and practical conditions of solid fuel regression rate behavior or options of propellants. Upper and lower limits of thrust in each method can also be evaluated from the aspect of the design variables of fuel grains and rockets. Throttlability of Aft-end Oxidizer Injection Method using tangential injection should be discussed.

In Chapter 4, transition from developing turbulent boundary layer to fully developed pipe flow should be studied more. Modelling this region enables to greatly improve fuel regression rates in downstream of transition points.

On the topics in Chapter 5, first of all, many trials of static firing experiments of A-SOFTs should be carried out. We should focus especially on the experimental conditions in low effective geometric swirl numbers because stability of weak swirl in combustion flows is not clear. Moreover, the approximated function of regression rates of SOFTs and A-SOFTs should have an inflection point in a low swirl number. Investigation of fuel regression behaviors is also important in cases of existence of back step between injector outlet and solid fuel grain. These conditions change local swirl number because difference of diameters between the injector outlet and the fuel port changes both representative axial and circumferential velocity components of main flow. In addition to static characteristics, transient responses after throttling are also important. In order to understand basic response, it is easy to carry out firing experiments including step changes of thrust before continuous throttling tests. Our measurement method of local regression rates had large measurement errors due to the accuracy of the laser distance meter. Introduction of more accurate distance meter will improve the large measurement errors instantaneously. From the aspect of measurement of c* efficiency, it is necessary to improve accuracy of thrust measurement system.

Besides the improvements and expansion of the individual research topics discussed in this thesis, there are still several elemental technologies necessary to integrate A-SOFT as an independent propulsion system. Oxidizer vaporization systems and real-time fuel regression rate measurement systems are the representative ones. Oxidizer vaporization systems had been conceptually developed and demonstrated, but validated in the integrated systems including the engines all over planned throttle ranges. Real-time

regression rate measurement systems are one of the most important elemental systems to control A-SOFTs, which is used to feedback real-time status of fuel consumption during engine operation. These systems also had been conceptually demonstrated, but accuracies of the current systems had not been discussed or studies to acquire regression rates under dynamic acceleration were not found. Moreover, feed forward and feedback control theory of A-SOFTs also should be developed and practically demonstrated under an integrated A-SOFT system.